

FACULTY
OF MATHEMATICS
AND PHYSICS
Charles University

MASTER THESIS

Bc. František Zajíc

The study of scintillation properties of single crystals grown by floating zone method

Department of Condensed Matter Physics

Supervisor of the master thesis: doc. RNDr. Jiří Pospíšil, Ph.D.

Study programme: Physics of Condensed Matter and Materials

Prague 2024

I declare that I carried out this master thesis on my own, and only with the cited sources, literature and other professional sources. I understand that my work relates to the rights and obligations under the Act No. 121/2000 Sb., the Copyright Act, as amended, in particular the fact that the Charles University has the right to conclude a license agreement on the use of this work as a school work pursuant to Section 60 subsection 1 of the Copyright Act.

In ..... date ....

Author's signature

I would like to express my gratitude to my supervisor, doc. RNDr. Jiří Pospíšil, Ph.D., for his guidance in scientific research, for facilitating valuable contacts, and for his patience.

My heartfelt thanks go to Ing. Vítězslav Jarý, Ph.D. for his invaluable guidance, assistance, and encouragement during the preparation of my first manuscript, for introducing me to optical and scintillation measurements, and for the evening discussions we had at conferences.

Special thanks to prom.fyz. Pavel Boháček for preparing the powder precursors and the GSAG seed crystal, to Mgr. Romana Kučerková and Ing. Alena Beitlerová for conducting the optical measurements, and to prof. Ing. Martin Nikl, CSc., for supervising the work at the Institute of Physics of the Czech Academy of Sciences and providing profound insights into the field of scintillators. I would like to thank Crytur s.r.o. for providing the seed crystals of GGAG.

I extend my thanks to Mgr. Anna Yaghobová for her invaluable assistance with my GAUK project, for serving as a role model of Ph.D. student and young researcher, and for reminding me, that things can be different elsewhere. I also want to express my gratitude to Bc. Petr Vincena for always being there for me.

My (rather long) years of study at the Faculty of Mathematics and Physics were the best of my life, and I extend my gratitude to all those I encountered during this period who contribute to the essence of Matfyz, especially to all my friends, to my flatmates at dormitory, to my fellow organizers of summer camps and correspondence seminars and to the people from the Academic Senate. I would like to bid farewell to this chapter of my life with a quote from the poem *Sbohem a šáteček* by Czech poet Vítězslav Nezval:

Bylo to krásné a bylo toho dost.

Title: The study of scintillation properties of single crystals grown by floating zone method

Author: Bc. František Zajíc

Department: Department of Condensed Matter Physics

Supervisor: doc. RNDr. Jiří Pospíšil, Ph.D., Department of Condensed Matter Physics

Abstract: High-energy physics and medical applications require novel scintillators with superior performance. The production of modern multicomponent garnet scintillators is often costly due to the use of expensive crucibles. In this study, two series of multicomponent garnet scintillators, GGAG:Ce,Mg and GSAG:Ce, were prepared using a crucible-free laser-diode floating zone method with in-house developed afterheater. The prepared samples were evaluated for their optical and scintillation properties. The GGAG scintillators exhibited excellent performance, with light yields and scintillation decay times matching the performance of the state-of-the-art scintillators documented in the literature. The GSAG samples were significantly affected by iron contamination, achieving a lower light yield with fast decay times, but high afterglow. The results of this thesis were published and presented at international conferences.

Keywords: single crystal, floating zone method, scintillator, garnet

Název práce: Studium scintilačních vlastností krystalů rostlých metodou plovoucí zóny

Autor: Bc. František Zajíc

Katedra: Katedra fyziky kondenzovaných látek

Vedoucí bakalářské práce: doc. RNDr. Jiří Pospíšil, Ph.D., Katedra fyziky kondenzovaných látek

Abstrakt: Fyzikální aplikace v oblasti fyziky vysokých energií a medicíny si žádají scintilátory nové generace s vynikajícími scintilačními charakteristikami. Výroba moderních multikomponentních scintilátorů na bázi granátů je nákladná kvůli použití drahých kelímků. V této práci byly připraveny dvě série multikomponentních scintilátorů na bázi granátů, GGAG:Ce,Mg a GSAG:Ce, pomocí bezkelímkové metody plovoucí horké zóny s laserovým topením a námi vyvinutým dohřevem. Optické a scintilační vlastnost vzorků byly proměřeny. GGAG scintilátory vykazovaly vynikající vlastnosti, light yield časy scintilačního dosvitu jsou srovnatelné s nejlepšími scintilátory v literatuře. GSAG vzorky byly výrazně ovlivněny kontaminací železem. Dosáhly nízkého light yield s rychlými časy dosvitu a vysokým afterglow. Výsledky této práce byly publikovány a prezentovány na mezinárodních konferencích.

Klíčová slova: monokrystal, metoda plovoucí horké zóny, scintilátory, granát

Contents

Introduction **7**

1 Physics of scintillators **9**
1.1 Luminescence . . . 9
1.1.1 Luminescence according to the band model of solids . . . 10
1.2 Process of scintillation . . . 10
1.2.1 Conversion . . . 10
1.2.2 Transport . . . 12
1.2.3 Luminescence . . . 12
1.3 Production of scintillators . . . 12
1.3.1 Czochralski method . . . 12
1.3.2 Micro-pulling-down (μ-PD) . . . 14
1.3.3 Floating zone method . . . 15

2 Scintillation parameters and materials **16**
2.1 Scintillation material parameters . . . 16
2.1.1 Density, effective atomic number, and attenuation coefficient 16
2.1.2 Position of emission . . . 18
2.1.3 Scintillation efficiency and relative efficiency . . . 18
2.1.4 Scintillation lifetime . . . 18
2.1.5 Afterglow . . . 19
2.1.6 Light yield . . . 19
2.1.7 Proportionality and energy resolution . . . 19
2.1.8 Temperature stability of the emission . . . 19
2.2 Halogen scintillators . . . 20
2.3 Oxide-based scintillators . . . 20
2.4 Utilization of scintillators . . . 21
2.4.1 Scintillation probe construction . . . 22

3 GGAG and GSAG **24**
3.1 Gadolinium Gallium Aluminium Garnet . . . 24
3.2 Gadolinium Scandium Aluminium Garnet . . . 24

4 Instrumentation **26**
4.1 Sintering process . . . 26
4.2 Laser-Diode Floating Zone furnace . . . 26
4.2.1 Passive afterheater . . . 27
4.2.2 Active afterheater . . . 27
4.3 Measurement of optical properties . . . 27

5 Preparation of single crystals **29**
5.1 GGAG single crystals . . . 29
5.1.1 Powder precursor . . . 29
5.1.2 Rod precursor preparation . . . 29
5.1.3 Growth of single crystals . . . 30

5.2 GSAG single crystals . . . 30
5.2.1 Powder precursor . . . 30
5.2.2 Rod precursor preparation . . . 30
5.2.3 Growth of single crystals . . . 32

6 Characterization of single crystals 33
6.1 GGAG . . . 33
6.1.1 Absorption spectra . . . 33
6.1.2 Radioluminescence spectra . . . 35
6.1.3 Scintillation decay . . . 35
6.1.4 Light yield . . . 37
6.1.5 Afterglow . . . 37
6.1.6 Photoluminescence spectra . . . 37
6.1.7 Photoluminescence decay . . . 43
6.2 GSAG . . . 44
6.2.1 Absorption spectra . . . 44
6.2.2 Radioluminescence spectra . . . 46
6.2.3 Scintillation decay . . . 47
6.3 Light yield . . . 48
6.3.1 Afterglow . . . 48
6.3.2 Photoluminescence spectra . . . 50
6.3.3 Photoluminescence decay . . . 51

7 Discussion 55
7.1 Quality of prepared crystals and comparation with literature . . . 55
7.1.1 GGAG . . . 55
7.1.2 GSAG . . . 55
7.2 Effect of afterheater in floating zone method . . . 57
7.3 Iron contamination . . . 58

Conclusions 60

Bibliography 61

List of Figures 73

List of Tables 75

Introduction

Ionizing radiation is present in many aspects of human life, ranging from nuclear reactors and atomic bombs to non-destructive testing, high-energy physics, and medical diagnostics and treatments. To harness the benefits and potential dangers of ionizing radiation effectively, sensitive and efficient detectors are essential to assess its impact.

Scintillators are materials that transform energy, converting high-energy photons of ionizing radiation into visible-light flashes, which can then be processed by photomultipliers and converted into electrical signals. Garnet scintillators, which are oxide-based materials, are particularly valued for their short scintillation times and high light yield. These properties can be tailored to specific applications through co-doping. Furthermore, garnet scintillators are user-friendly because of their chemical and thermal stability, as well as their robust mechanical properties.

Currently, intensive research is underway to enhance the scintillation properties of these materials, aiming for their application in high-energy physics (e.g. SpaCal - Spaghetti Calorimeters at LHCb, CERN) and potentially in Time-of-Flight Positron Emission Tomography (ToF-PET).

Gadolinium Gallium Aluminum Garnet (GGAG) is a product of the past decade's research on scintillators, offering excellent light yield and time resolution. However, its production is costly, as it is typically carried out using the Czochralski method with expensive iridium crucibles and ZrO_2 thermal shields, due to its high melting point of 1800°C. The reactivity of gallium oxide with more affordable molybdenum (Mo) or tungsten (W) crucibles at the melting point precludes their use.

Gadolinium Scandium Aluminum Garnet (GSAG) represents an effort to further shorten the scintillation time of GGAG while enabling growth in less expensive molybdenum crucibles by eliminating gallium from the composition.

We propose the preparation of a series of GGAG and GSAG samples using a promising crucible-free laser-diode floating zone method, which could circumvent the aforementioned limitations. Our goal is to measure the optical and scintillation properties, compare them with existing literature, and evaluate the feasibility of using the laser-diode floating zone method for the research and development of novel scintillation materials.

The growth of single crystals will be carried out in the Laser-Diode Floating Zone Furnace at the MGML laboratory, Faculty of Mathematics and Physics, Charles University, Prague. The prepared powder precursors for all our single crystals will be provided by Pavel Boháček from the Institute of Physics of the Czech Academy of Sciences. The seed crystals for the GSAG single crystals will be supplied by the Crytur company, while the seed crystal for GGAG will be grown by Pavel Boháček at the Institute of Physics.

Measurements of the optical and scintillation properties will take place at the Institute of Physics of the Czech Academy of Sciences, conducted by Romana Kučerková and Alena Beitlerová, with analysis by the author of this thesis.

This thesis is organized into seven chapters. The first chapter explains the basics of scintillation physics, the origins of luminescence, and methods for producing scintillators. The second chapter discusses common parameters of scintillators,

focusing on well-known scintillators and their applications. The third chapter presents the current state of knowledge on GGAG and GSAG materials. The fourth chapter describes the instrumentation used in this research. The fifth chapter details the process of preparing single crystals. The sixth chapter characterizes the single crystals, and the seventh chapter discusses the results, comparing them with the existing literature. The conclusion summarizes our findings.

1 Physics of scintillators

1.1 Luminescence

Luminescent phenomena are naturally occurring (e.g., fireflies, jellyfish, rotting wood, or aurora) and have fascinated people since time immemorial. The term luminescence was first used in 1888 by Eilhart Wiedermann to describe all processes in which light radiation is not associated with the rise in temperature [1, 2]. The phenomenon of luminescence was studied thoroughly by George Stokes in the 19th century, who discovered that the frequency of absorbed light is always higher than that of radiated light, which is known as the Stokes shift [1, 2].

The modern definition of luminescence according to Sergej Ivanovich Vavilov [3] is following:

> *Luminescence is the surplus of the radiation emitted by a body above the thermal radiation, that has a finite time of duration, significantly higher than the period of light waves (10^{-15} s).*

Luminescent material (also luminophore, phosphor) is a substance that converts some of the forms of energy to visible light (VIS), ultraviolet, or infrared radiation (together near-VIS) [1]. Luminescent material contains luminescent centres in which the conversion of energy to light occurs. The centre can be an intrinsic component of the material or can be artificially created by a suitable dopant [1].

We can distinguish several types of luminescence according to the form of energy converted to light [1]:

- **Photoluminescence** caused by excitation by electromagnetic radiation typically from the near-visible area of energies (stars on the ceiling of the children's room)
- **Radioluminescence** caused by excitation by ionizing radiation (watch hands containing radium)
- **Chemiluminescence** caused by excitation by chemical reactions (luminol, lightsticks)
- **Bioluminescence** caused by excitation by enzymatic reaction in living organisms (fireflies, jellyfish)
- **Triboluminescence** caused by excitation by the energy of mechanical deformation (rapid deformation of a sugar cube)
- **Sonoluminescence** caused by excitation by sound waves (imploding bubbles in water e.g. cavitation by mantis shrimp)
- **Electroluminescence**, caused by excitation by electric current (electroluminescent displays in cars)

One can also distinguish luminescence by the rate of decrease in light intensity [1]. **Fluorescence** is a very fast process ($< 10^{-8}$ s), the luminescent centre is excited from the ground state and returned by the spontaneous emission process.

Fosforescence is a slower process ($> 10^{-6}$), typical conversion via a forbidden transition, during which the system returns from excited states through (cascade) metastable energy levels.

1.1.1 Luminescence according to the band model of solids

Atoms in the crystal lattice are surrounded by the number of neighbouring atoms, resulting in effective valence-shell overlap. According to the band model of solids, this leads to a huge number of energy levels with very close energies, which we call energy bands. The energy bands in dielectric materials form a significant gap (> 5 eV) between the valence band and the conduction band [4].

The scintillation process starts with the excitation of a valence electron into the conduction band, which creates a pair of free electrons in the conduction band and a hole in the valence band. In the forbidden gap, there might be rare energy levels that are close to the conduction band and can act as traps for the excited electron. When the electron is trapped, at such an energy level, the energy supplied by an external source is needed to excite the electron again into the conduction band. The presence of traps is caused by impurities or other imperfections in the crystal lattice and is determinative of the time characteristic of the luminescence process. They are undesirable for scintillation material and crucial for persistent luminophore. The presence of traps is determined in the process of preparation of the material and could be difficult to influence later. At the luminescent centre, the recombination of electrons in the conduction band and holes in the valence band can occur while emitting light [5, 1].

The width and energy position of the forbidden gap (and the position of the impurity energy level) can be influenced by doping or co-doping of the mother material (which can determine whether the impurity will form a trap) [6, 7, 8, 9]. This approach is called band-gap engineering and led to the creation of several modern scintillation materials [10, 11].

1.2 Process of scintillation

The scintillation effect can be divided into three consecutive processes: conversion of the energy of the incoming photons into the scintillator material; transport of energy to the luminescence centre and luminescence by recombination of the electron and hole [2]. A schematic representation of the scintillation process is shown in Figure 1.1

1.2.1 Conversion

Absorption of ionising radiation in matter occurs through the photoelectric effect (ph), Compton scattering (C) and the production of electron-positron pairs (ep) [1]. The total cross section can be written as a sum of the respective cross sections:

$$\sigma_{total} = \sigma_{ph} + \sigma_C + \sigma_{ep} \tag{1.1}$$

The photoelectric effect can occur on the bonded electrons when part of the photon momentum is transferred to the atom. During the photoelectric effect, the

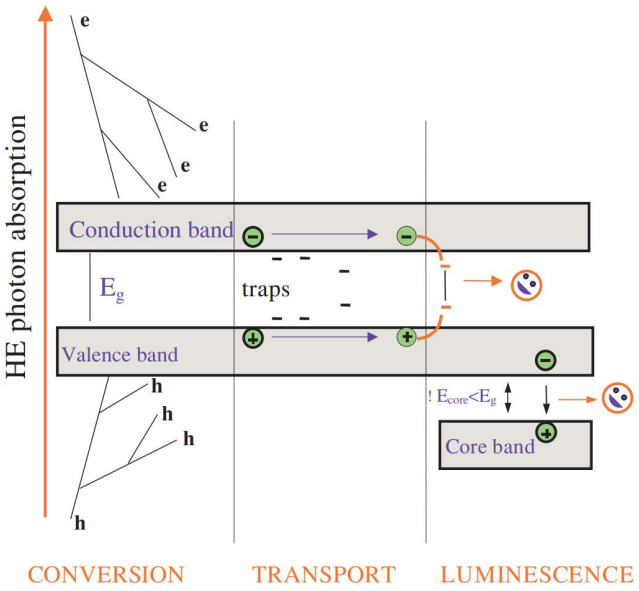


Figure 1.1 Scintillation process divided into three consecutive parts: conversion, transport and luminescence [12].

incoming photon is fully absorbed by the electron from the inner electron shell of an atom. The electron is ejected from the shell and obtains a kinetic energy equal to the difference between the energy of the incoming photon and the binding energy of the electron (a.k.a. ionisation or output work) [1].

$$E_{electron} = hf_{photon} - W_{output} \tag{1.2}$$

Compton scattering is an interaction between photon and electron when part of the photon energy E_γ is transferred to the weakly bonded electron [5]. The photon carries away energy $E_\gamma{}'$ and the electron gains energy $E_\gamma - E_\gamma{}'$. This electron can produce another secondary electron. Applying the law of conservation of energy and momentum, we obtain the following formula [1]:

$$E_\gamma{}' = E_\gamma \frac{1}{1 + \frac{E_\gamma}{m_e c^2}(1 - \cos\theta)} \tag{1.3}$$

where θ is the angle between incident and scattered photon, m_e is the mass of the electron and c is the speed of light.

If the energy of the incident photon is greater than $2m_e c^2 = 1022$ keV, the production of positron-electron pairs can occur in the Coulombic field of the atomic nuclei. If the energy of the photon exceeds $E_\gamma > 4m_e c^2$, production can occur in the electric field of the electron, although the probability of such a process is approximately three orders lower [1].

Through these three processes, release of energetic electrons from the inner shell occurs, and holes with high energy interact with ions in the crystal lattice. The result is the creation of a strongly spatially inhomogeneous concentration of thermalised electrons in the conduction band and holes in the valence band. The conversion process usually occurs on a subpicosecond time scale [5, 1].

1.2.2 Transport

The electrons created in the conduction band and the holes in the valence band are transferred by the diffusion process [5, 1]. From the point of view of the band model of solids, electrons as well as holes can be trapped in shallow or deep traps that exist in the forbidden band gap. The release of the trap is caused by the supply of activation energy. The activation energy of the shallow traps is low and corresponds to the energy of thermal processes in the crystal lattice. The release of the electron from the shallow trap is not negligible, and thus shallow traps cause a delay in the scintillation response. The activation energy of deep traps is higher than that of thermal processes, electrons are likely to stay in such holes, and the presence of deep traps usually leads to a reduction in scintillation light yield (LY) [10, 1, 5].

The electron traps in the materials are caused by defects in the crystal lattice and are practically exclusively incorporated at the moment of scintillator manufacturing, single-crystal growth. Unsparing treatment or radiation damage can induce the further generation of traps during their operational life [13].

Traps are located inside the forbidden gap as extra energy levels, so one way to improve the scintillation properties of a material is band-gap engineering. By tuning the composition of the scintillator by a dopant or codopant, we can in certain cases reduce the size of the forbidden gaps in such a way that traps fall into the conducting (valence) band. Using this approach, we can achieve a faster scintillation response, as band gap engineering is mainly useful to reduce the number of shallow traps [10, 1].

1.2.3 Luminescence

When transport is successful and the electron is not trapped in a deep trap, the process of recombination occurs at the luminescent centre. The characteristic time of luminescent recombination can be observed experimentally by measuring the scintillation response at low temperatures [1, 5].

1.3 Production of scintillators

1.3.1 Czochralski method

Czochralski method of single crystal growth was discovered by accident by the Polish scientist, chemist, and metallurgist Jan Czochralski in 1916 [14]. Since then, it has been used successfully for the preparation of various materials. Today, it is the most important industrial method for the production of large amounts of single crystals [14, 15, 16]. It should be noted that it is the main method for the production of single silicon crystals, which are the foundation for semiconductor components and information technology in general [16].

The schematic overview of the principle of the Czochralski method and the illustration of the gradual technological steps are given in 1.2. The stoichiometric mixture of the purified starting materials is melted in the crucible, which is heated by resistance or induction heating. The material of the crucible is critical because the crucible must withstand the temperature of melting point of the

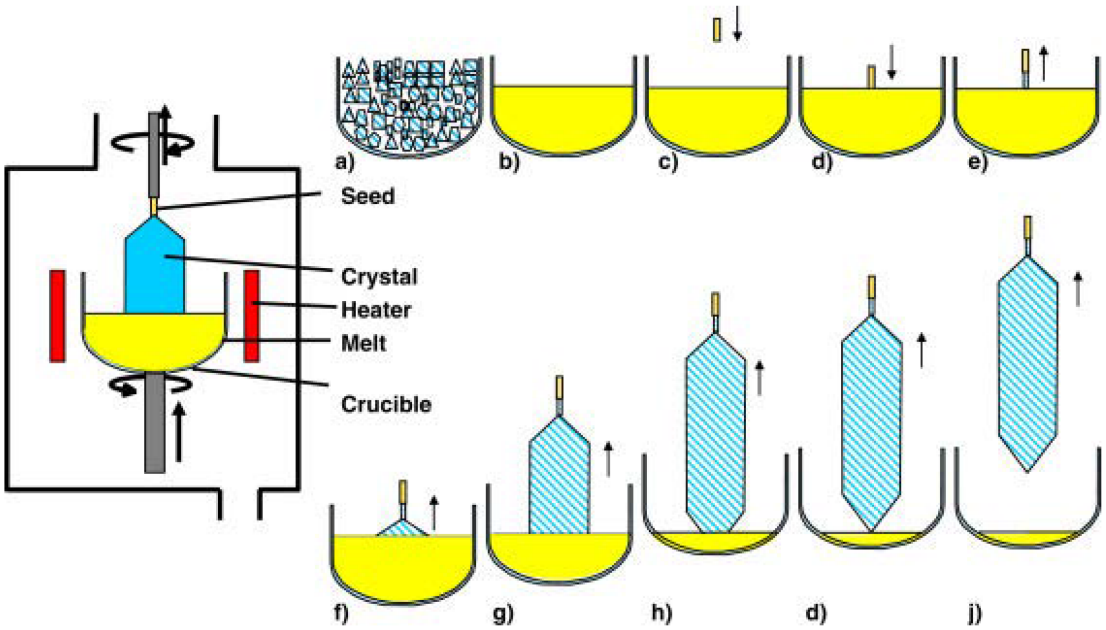


Figure 1.2 Schematic of the principle of the Czochralski method (left) and illustration of the different steps (a–j) of the Czochralski process for growing a Si crystal. (a) The polycrystalline feedstock is melted (b) in a crucible. (c, d) Seeding procedure: The seed crystal is dipped into the melt, followed by Dash necking (e), shouldering (f), cylindrical growth (g), growth of end cone (h), lift off (i), cooling down and removing of the crystal (j) [17].

grown material. Then a seeding procedure takes place: the seed crystal is dipped in the melt, followed by dash necking, shouldering, cylindrical growth, growth of the end cone, lift off, cooling, and removal of the crystal [17].

The advantage of the Czochralski method is the possibility to produce single crystals in (relatively) large quantities. The setup is usually equipped with a set of afterheaters to reduce the temperature gradient, which suppresses the internal mechanical stress that causes cracks and improves the overall quality of the single crystals produced [15].

The production of single crystal scintillator materials using the Czochralski method has several specifics [15]. The melting points of commercially produced scintillation materials are 1970°C (YAG:Ce) [18], 1850°C (GGAG) [19] or 2020°C (LuAG) [20]. This imposes a strong limitation on the material of the crucible; suitable materials are only platinum or iridium, which are both very costly. At such high temperatures, the crucible has to be protected, so growth takes place in a protective atmosphere of argon or varigon ($5\%H_2$+$95\%Ar$), which is suboptimal for oxide-based scintillators, as this supports the creation of oxygen vacancies in the crystal lattice of the scintillator [21].

The main problem of the Czochralski growth of GGAG is the evaporation of the volatile Ga_2O_3 from the melt [22]. This is handled by adding Ga_2O_3 to the precursor mixture above the stoichiometric amounts and the growth in the atmosphere that contains a few percentages of O_2 [10, 23, 24, 25]. Gallium evaporation creates cation vacancies that inevitably lead to the formation of anionic vacancies, vacancy clusters, and trapping centres [24]. Furthermore, the use of an oxygen-poor growth atmosphere leads to oxygen vacancies, which act as

electron traps [21], thus contributing to a longer scintillation response. In addition, the deposition of Ir particles from the crucible on the surface of grown crystals has been reported [23].

1.3.2 Micro-pulling-down (μ-PD)

The micro-pulling-down method was first introduced in 1982 under the name Shaped Melt Lowering by Shintaro Miyazawa [26] and was perfected during the 1990s at Tohoku University Japan, where the first prepared material was $LiNbO_3$ [27]. The schematic overview of the method is given in Figure 1.3. The crucible with one or more capillaries is placed onto the afterheated and is heated by induction of the radio frequency coil. The starting material in the crucible is melted, and the seed touch is performed with the seed rod from the bottom. Moving the seed crystal down causes the melt to crystallise. At the same time, the melt spills across the punch as a result of the wettability of the surface. The shape of the punch can thus determine the shape of the prepared single crystal.

Micro-pulling-down method is suitable for the preparation of small quantities of single crystals, a diameter of up to 5 mm and a length of several cm are achievable. The preparation is relatively fast; the pulling speed can be as high as 0.1 mm / min and is therefore suitable for performing composition scan studies. The overall quality of the crystals is influenced by the fact that the pulling speed of the crystallisation process is far from equilibrium [29].

The disadvantages of the method are similar to the Czochralski method and are determined primarily by the presence of the crucible. The growth process must be performed in a protective inert or slightly reductive atmosphere. The cost of the crucible material is the main component contributing to the price of prepared single crystal [30].

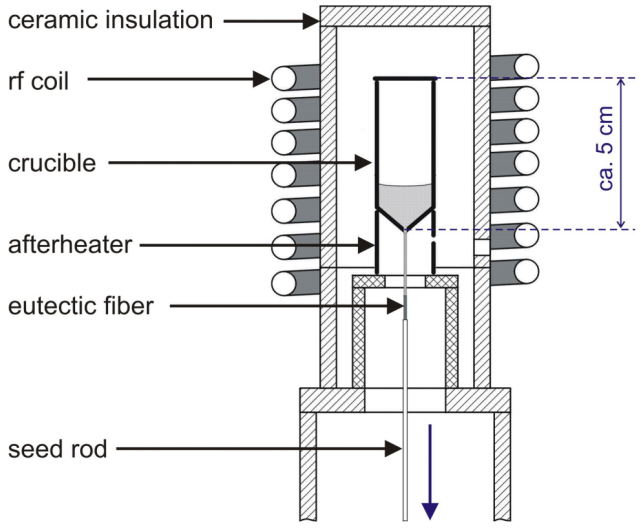


Figure 1.3 Schematic representation of micro-pulling-down method [28].

1.3.3 Floating zone method

All the disadvantages of the methods listed above can be solved using crucible-free methods, since the crucible is the weak point of the growth process in several aspects [10, 24, 31, 16, 30, 32]. One of them, the floating zone method, has achieved significant instrumental progress triggered by its use in the growth of single crystals of high T_c superconductors [33]. Very popular implementations are mirror optical furnaces with halogen or xenon lamps also known as Optical Floating Zone (OFZ) or Travelling Solvent Zone Method (TSZM) [34, 35, 36, 37], which makes higher temperatures of up to 3000 °C attainable [38, 37, 39, 40, 41, 42] with lower energy consumption compared to conventional crucible methods [43]. The furnaces with laser heating, known as the Laser-Diode Floating Zone Method (LDFZM) or Laser-Heated Pedestal Growth (LHPG) are the most advanced instruments of single crystal growth by floating zone [43]. The influence of the number of lasers on the uniformity of the heating has been investigated [44]. Several fibre laser single crystals have been grown [45, 46, 47, 48, 49, 50]. In terms of scintillators, BGO and LSO materials have been successfully prepared [51].

In the literature, we have found three cases of the use of the optical floating zone method to the growth of GGAG [38, 52, 23]. Articles from Suzuki (2012,[52]) and Yoshikawa (2013, [23]) study the influence of different oxygen concentrations on scintillating properties and persuasively show that suppressing the slow decay component can be related to reducing oxygen vacancies or improving stoichiometry due to growth in an oxygen-rich atmosphere. The article from Wu (2021, [38]) focusses on finding the optimal $(Ce_xGd_{1-x})_3Ga_2Al_3O_{12}$ $(x = 0 - 0.8)\%$ composition and also supports the hypothesis of an oxygen-rich atmosphere-induced improvement of the scintillation properties due to inhibition of Ga_2O_3 evaporation.

2 Scintillation parameters and materials

The scintillator works as spectral and energy transformer; it converts a high-energy photon from the X- or gamma-ray range into a bunch of UV–vis ones, i.e., to a flash of light [10]. The flash of light should be easily and with great sensitivity detectable by classic photomultipliers, photodiodes, or other methods of light detection [1]. The different practical uses needs different scintillation permormance. The scintillation material must be chosen in mind with the practical application and should be chosen according to its performance in following aspects [1, 10]:

a) **High scintillation efficiency** - Scintillation material should transform ionising radiation to detectable light with high scintillation efficiency and thus produce a high light yield.

b) **Short scintillation lifetime** - The luminescence lifetime should be short for two consecutive events to be distinguishable.

c) **Proportionality** - This transformation should be linear in terms of light yield (number of radiated photons) proportional to the energy delivered in the widest range possible.

d) **Transparency** – Scintillation material should be transparent for the emitted wavelength to ensure effective light detection.

e) **Optical quality and production** – Material production should be cheap and well managed in terms of the size, amount and optical quality needed for the application.

f) **Refractive index** – Refractive index of material should be close to the refractive index of the glass to ensure an effective connection of the scintillator and the photomultiplier or other detection device.

g) **Type of radiation discrimination** – Some applications require different scintillation responses for different types of ionising radiation.

h) **Stability** – Scintillation material should be durable and resistant to chemical and physical processes. The material should not deteriorate over time and upon exposure to ionising radiation; it should have a high radiation resistance.

2.1 Scintillation material parameters

2.1.1 Density, effective atomic number, and attenuation coefficient

Cross-sections of the photoelectric effect, Compton scattering, and production of positron-electron pairs are strongly dependent on the density and atomic number of materials. Generally, a higher density and atomic number signifies a higher conversion efficiency [10].

The density depends on the chemical composition of the scintillator and the atomic numbers of the elements represented. The effective atomic number Z_{eff} is the weighted average of the atomic numbers represented in the scintillator that can be determined:

$$Z_{eff} = \sqrt[2.94]{\sum_{i=1}^{n} f_i \left(Z_i\right)^{2.94}} \tag{2.1}$$

where f_i are fractions of the total number of electrons connected to each chemical element and Z_n is the atomic number of the respective element [1].

The ability to stop photon radiation is determined by the attenuation coefficient μ [cm], which is given by the density and the chemical elements inside the material [1, 5]. The intensity of the radiation after the passage through the material is as follows:

$$I = I_0 \exp\left(-\mu x\right) \tag{2.2}$$

where I_0 is the original intensity and x is the width of the material. For the attenuation given by photoelectric effect only, the attenuation coefficient is proportional $\approx \rho {Z_{eff}}^{3-4}$ [1]. We can define the mass attenuation coefficient μ/ρ which is independent on density. The inverse of the linear attenuation coefficient μ corresponds to the photon mean free path λ [cm], i.e. the average distance the gamma-ray intensity is reduced by a factor e [1].

The mass attenuation of photons with various energies in lead is shown in Figure 2.1. For low-energy photons, the photo effect is the most important, for the energy range $0.6 - 4$ MeV, the Compton effect plays a major role and for higher energies, the production of positron-electron pairs is the most important.

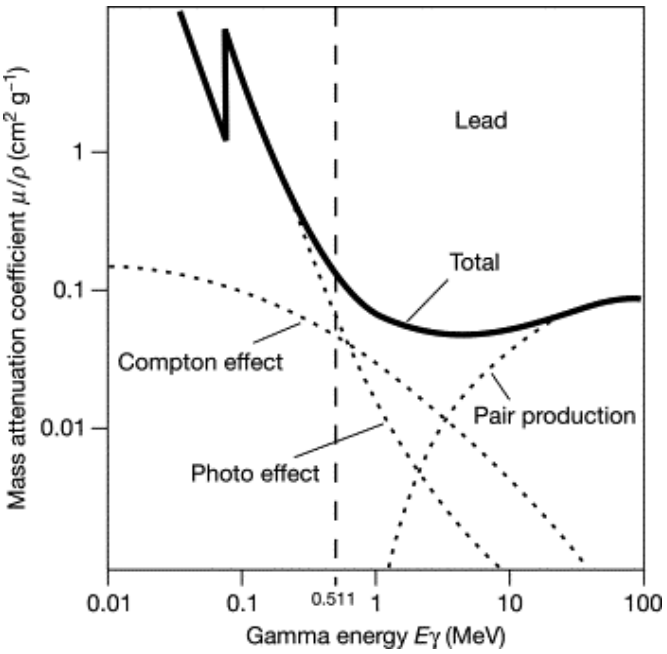


Figure 2.1 Mass atenuation coefficients of photons with different energy in lead [53].

2.1.2 Position of emission

The energy of the scintillation photons produced by the scintillator is important because of the sensitivity of the detector. Photomultipliers and photodiodes are most sensitive in the wavelength range of 300 to 500 nm. [1]

2.1.3 Scintillation efficiency and relative efficiency

The number of photons produced during scintillation conversion of the incident photon with energy E is defined as:

$$N = \frac{E}{\beta E_g} SQ \tag{2.3}$$

where E_g is the size of the forbidden gap of the material, and S and Q are quantum efficiencies of transport and luminescence. The phenomenological parameter β is 2-3 for most materials [10].

Energetic efficiency of scintillation η is defined as

$$\eta = \frac{\langle hf \rangle}{E} SQ \tag{2.4}$$

where $\langle hf \rangle$ is the mean energy of produced scintillation photons and can be calculated as

$$\langle hf \rangle = \frac{\int_{f_{min}}^{f_{max}} hf \cdot I(f) df}{\int_{f_{min}}^{f_{max}} I(f) df} \tag{2.5}$$

where $I(f)$ is the intensity of scintillation emission at frequency f and f_{min}, f_{max} are minimal and maximal frequencies, respectively [1].

2.1.4 Scintillation lifetime

The scintillation lifetime is a characterisation of the time after which the response of the scintillator is detected after interaction with ionising radiation. The emission is spread over time, so the lifetime of the scintillation is the time after which the intensity decreases to the $1/e$ of the original intensity [1].

The scintillation lifetime is primarily a characteristic of the luminescent centre, but it can be prolonged by traps in the course of the transport process. As the presence of traps is determined by the presence of defects in the material, which are dependent on the preparation process, the preparation method is crucial for the performance of the scintillator [10].

The time dependence of the intensity is usually fitted as the sum of the $N = 1 - 3$ exponentials:

$$I(t) \ = \ \sum_{i=1}^{N} A_i e^{-\frac{t}{\tau_i}} \tag{2.6}$$

where τ_i are the time constants and A_i are the amplitudes. The amount of light belonging to the time constants is determined by light sum (LS)[1]

$$LS_i = \frac{A_i \tau_i}{\sum_{j=1}^{N} A_j \tau_j} \cdot 100\% \tag{2.7}$$

2.1.5 Afterglow

Afterglow includes all other delayed processes that occur after scintillation emission, which is important in terms of the detection of ionizing radiation. The time after which light emission is considered afterglow is arbitrarily defined and usually is several milliseconds [1]. The delay in emission is caused by defects in the scintillator, such as shallow and deep traps. The afterglow is considered undesirable in terms of scintillator performance as it decreases the light yield, but is very important in other persistent luminophores. The standard for measuring the afterglow characteristics of scintillators is bismuth germanate $Bi_4Ge_3O_{12}$ (BGO) with a nearly five-order-of-magnitude drop in signal intensity after excitation cutoff.

2.1.6 Light yield

The light yield (LY) is the normalized amount of light that is released from the scintillation material after the absorption of 1 MeV of energy. Halogen scintillators are superior to oxide-based ones in terms of light yield that reaches up to 120,000 photons per MeV [11, 1]. The best widely used oxide-based scintillator, which is currently gadolinium gallium aluminium garnet $Gd_3(Al,Ga)_5O_{12}$ (GGAG) can reach up to 70 000 – 80 000 ph/MeV [54]

So-called integral light yield is often represented as a fraction of released photons, measured as radioluminescence spectra, compared to the standard BGO sample under the same experimental conditions. GGAG has an integral light yield of several hundred percent compared to BGO [10, 25, 24].

2.1.7 Proportionality and energy resolution

Proportionality is closely related to light yield and refers to the change in light yield dependent on the change in energy of the incident ionizing radiation. Good proportionality is key for achieving high-energy resolution of the scintillation detectors.

The energy resolution is the relative difference between the energy of two particles that can be distinguished. A scintillation detector with good energy resolution can not only register incident radiation but also determine its energy and possibly identify the source of the radiation, which is useful for gamma spectroscopy [11].

2.1.8 Temperature stability of the emission

The emission properties of the scintillation materials are temperature dependent and have the best efficiency at low temperatures, when thermal processes are negligible. For most applications, the stability around room temperature (300K) is sufficient, although some require stability up to 600K. The negative effects of thermal processes result mainly in decreased light yield and shortening of the lifetime at higher temperatures [1].

2.2 Halogen scintillators

Halogen scintillators occupy a prominent position within the broad family of scintillating materials, known for their high light yield, fast response times, and outstanding energy resolution (compared to those of oxide-based materials), which make them particularly valuable in various radiation detection applications that require high sensitivity and imaging applications. These materials typically contain halogen elements, such as iodine or bromine, combined with alkali metals or other compounds, forming crystals like sodium iodide (NaI). Halogen scintillators are extensively used in medical imaging, such as in gamma cameras for nuclear medicine, as well as in radiation detection instruments for security and environmental monitoring [11, 10].

However, the properties of halogen scintillators, such as hygroscopicity, low mechanical durability, and lower radiation hardness compared to those of some oxide-based scintillators, restrict their application in certain high-radiation or moisture-prone environments or require a special container, which can make the halogen-based solution more expensive.

The sodium iodine doped with thallium (NaI:Tl) is the most important example of halogen-based scintillators and one of the most widely used scintillating materials due to its excellent light yield (up to 40,000 ph/MeV) and high efficiency in detecting gamma rays. The scintillation lifetime of about 230 ns is fast enough for most applications and emission at 410 nm is suitable for use in scintillation probes with photomultipliers. It was discovered early after the discovery of the photomultiplier in 1948 [55]. Single crystals are produced by the Bridgman-Stockbarger method in large quantities (single crystals with a diameter of up to 80 cm and weighing up to 500 kg [1]) and in various shapes. Single crystals for commercial use are usually hermetically encapsulated in the aluminum sheath.

Another example of halogen-based scintillators is $LaBr_3$:Ce5% which was discovered at the beginning of the 21st century. It provides intensive emission in near UV 355 nm, which gives superior energy resolution 2.7% at 662 keV. The resolution can be further improved to 2% by co-doping the material with Sr [6]. This scintillator also has a light yield of up to 88,000 ph/MeV and is thus suitable to replace NaI:Tl in medical applications [1].

2.3 Oxide-based scintillators

Oxide-based scintillators are a prominent category within the family of scintillating materials, known for their robustness, high density, and superior radiation hardness. These materials are highly suitable for applications requiring high-energy radiation detection. One of the key advantages of oxide-based scintillators is their high density and atomic number, which enhance their efficiency in stopping and detecting high-energy photons, such as gamma rays and X-rays. This results in high detection efficiency and good energy resolution, essential for precise radiation measurements and particularly imaging. [56, 10, 11]

Furthermore, oxide-based scintillators are known for their excellent radiation hardness, in contrast to halogen-based materials. They exhibit good mechanical strength and chemical stability (not hygroscopic), making them less prone to damage and degradation over time, and no further encapsulation is needed. The

emission spectra of oxide-based scintillators can also be customized through doping with various activator ions, which can adjust their emission wavelengths to match the sensitivity ranges of common photodetectors. This tunability, combined with their intrinsic properties, makes oxide-based scintillators highly versatile and effective in a wide range of applications, including medical imaging, homeland security, and industrial non-destructive testing.

Bismuth germanate ($Bi_4Ge_3O_{12}$, BGO) is one of the oldest oxide-based scintillators, discovered in 1973 [57]. It combines high density (7.13 g/cm^3), high effective atomic number ($Z_{eff} = 74$), and fast and cheap production. Its utilization includes heavy-ions detection, PET scan detectors, and gamma spectroscopy. The main disadvantage is the low light yield (8,000 ph/MeV). Today, BGO is reference material for comparing scintillation integral light yield (usually as a percentage of BGO) and afterglow, which are extremely low (up to 3 orders of magnitude drop) [1].

Synthetically produced garnets expand the group of natural garnets with the structural formula $A_3B_2[XO_4]_3$. In independent tetrahedra XO_4, elements other than silicon (such as in natural garnets), such as Ge, Ga, Al, V, or Fe, can be present [58]. Today, any cubic material with the formula $A_3B_2[XO_4]_3$, which is structurally identical to natural garnets, is classified as a garnet, regardless of the specific elements it contains [59].

Yttrium aluminium garnet ($Y_3Al_5O_{12}$, YAG) is the most used garnet optical material. By doping YAG with an activator ion, we can achieve laser (Nd, Er, ...) or scintillation properties (Ce, Eu, Pr, etc.). One of the standard scintillation materials is YAG doped with Ce^{3+}, first prepared in the 1960s. Immediately after, the isostructural lutecium aluminum garnet ($Lu_3Al_5O_{12}$, LuAG) was introduced with superior density and the effective atomic number (6.67 g/cm^3, $Z_{eff} = 74$) was introduced. Unfortunately, the light yield of LuAG achieves only 26,000 ph/MeV [56].

Recent advances in the field of garnet scintillators are numerous multicomponent garnets. After the introductory study of single-crystal scintillators with composition: $(Gd, Lu, Y)_3(Ga, Al)_5O_{12} : Ce$, which for specific compositions revealed their excellent scintillation performance [60], their single-crystal growth, luminescence, scintillation characteristics and mechanisms were studied in numerous laboratories around the world [56, 61, 62, 63, 64, 65, 66, 67, 68, 69, 70, 71]. In 2012, using an iridium crucible, the Czochralski-grown 2-inch diameter single crystal of $Gd_3Al_2Ga_3O_{12} : Ce$ (GGAG:Ce) was reported [72] with high density (6.67g/cm^3), light yield (LY) of 46,000 ph/MeV and leading decay time of 88 ns in scintillation response. Further tuning of Ga/Al ratio revealed in $Gd_3Ga_xAl_{5-x}O_{12} : Ce$ Czochralski grown crystals at $x = 2.7$ LY of 58000 ph/MeV (approaching the theoretical limit [54]) and at $x = 2.4$ excellent energy resolution of 4.2%@662 keV [72].

2.4 Utilization of scintillators

Scintillators are vital in a wide range of applications due to their ability to convert high-energy radiation to visible light, making them crucial tools in radiation detection and imaging. We would like to mention several applications to demonstrate the importance of scintillators in today's society.

- **Medicine** - in medical imaging, scintillators are used both in radiology and nuclear medicine. Scintillators are used as detectors of gamma rays emitted by source of ionizing radiation either outside the patients body, or even radioisotope bound to the molecule inside patients body in devices such as positron emission tomography (PET/TOF-PET), single-photon emission computed tomography (SPECT), computational tomography (CT) or proton therapy [11].

- **High energy physics** - scintillators are indispensable in particle detectors and calorimeters, which are used to measure the energy and properties of particles produced in high-energy collisions [REF]. Large-scale experiments, such as those conducted at the Large Hadron Collider (LHC), utilize vast arrays of scintillating materials to track particles' paths and measure their energies with high precision. Scintillators are chosen for their high density and radiation hardness [25, 10, 73].

- **Astrophysics and space exploration** - scintillation detectors are used in space telescopes and other instruments to observe cosmic phenomena such as gamma-ray bursts, solar flares, and cosmic ray interactions [11, 1]. In planetary science, scintillators are used in instruments aboard space probes and rovers to analyze the composition of planetary surfaces and atmospheres. For instance, the Mars Science Laboratory's Curiosity rover is equipped with the Dynamic Albedo of Neutrons (DAN) instrument, which uses scintillators to detect hydrogen and infer the presence of water or ice below the Martian surface [74].

- **Homeland security** - radiation detectors equipped with scintillators are employed at ports, border crossings, and critical infrastructure to detect and identify radioactive materials, helping to prevent smuggling and unauthorized use of nuclear materials [75, 11]

- **Environmental monitoring** - scintillators are used to measure radiation levels in the environment, ensuring public safety and compliance with regulatory standards [76].

- **Industrial non-destructive testing (NDT)** - scintillators are used in radiography to inspect the integrity of materials and structures without causing damage. This is crucial for quality control in industries such as aerospace, automotive, and construction, where ensuring the safety and reliability of components is paramount.[77, 78]

2.4.1 Scintillation probe construction

Scintilation detector is the device that upon interaction with ionising radiation expresses (optical, electrical, etc.) response. If the response is proportional to the energy of the ionising radiation, we call such a detector spectrometer [1].

For the detection of the ionising radiation, we need to construct a scintillation probe. The scintillation probe consists of a scintillator (single-crystal, powder, ceramics, etc.), where the ionising radiation transforms into near-VIS light, a light guide that transfers light from the scintillator to the photomultiplier. The

photomultiplier contains the sensitive photodiode, which upon impact of light will produce the electron. The electron is then accelerated and multiplied in the system of electrodes (dynodes). The multiplicity factor in current photomultipliers is $10^5 - 10^7$. The electrical signal is then processed by electronics, computer and appropriate software. The spectral sensitivity of the photomultipliers is given mainly by the choice of the photodiode material [79, 1]

3 GGAG and GSAG

3.1 Gadolinium Gallium Aluminium Garnet

The search for new scintillating materials nowadays takes place using the band gap and defects engineering R&D strategies [10, 11]. A successful example of band gap engineering is the Ce^{3+} doped oxide scintillator of the garnet family $Gd_3(Al,Ga)_5O_{12}$ (GGAG) [72], which exhibits high density ($>$ 6 g/cm^3) and Ce^{3+} $5d \rightarrow 4f$ fast emission with a light yield approaching 60,000 ph/MeV, the fast component of scintillating decay of $\approx$ 60 ns and energy resolution below 5%@662 keV where all these parameters depend on Ga/Al ratio [61]. The crystal growth, luminescence, and scintillation mechanisms of Ce doped $(Gd,Lu,Y)_3(Ga,Al)_5O_{12}$ single crystals were studied in a number of laboratories worldwide [62, 63, 64, 65, 66, 67, 68, 69, 70, 71, 80, 81, 82]. The scintillation properties of Ce-doped single-crystal garnets can be further optimised by Mg^{2+} (Ca^{2+}) codoping [61, 83, 7, 9, 84]

Although a highly promising material, the production of GGAG is very expensive [30]. The commercial production of GGAG is carried out by the Czochralski method using costly iridium crucibles and ZrO_2 thermal shield due to the high melting point of 1800 °C [19]. Due to the reactivity of gallium oxide with cheaper Mo or W crucibles around the melting point, their use is excluded [30]. Kharkiv research group published several articles on garnet growth in nonprecious crucibles [30, 85, 86] and achieved light yield as high as 28000 ph/MeV for YAG:Ce. An effort has also been made to improve the properties of Ce:YAG by Mg codoping [87]. Another approach is to prepare one single crystal using almost all the melt using the Czochralski method and then to prepare several samples with different properties by cutting the plates from the plates of the single crystal at different places along its growth direction [25].

3.2 Gadolinium Scandium Aluminium Garnet

Gadolinium-scandium-aluminium garnet (GSAG) was studied mainly for its potential as a solid-state laser host [88, 89]. The first article on the scintillation properties of GSAG:Ce was published in 1994 [90], the scintillation properties of GSAG transparent ceramics have also been published [91]. Scandium can partially or fully substitute both Al and Ga in the GGAG host [63]. The effect of Sc codoping has recently been investigated in two papers [92, 93]. In the first article, it has been shown that partial substitution of Sc leads to a decrease in the band gap from 6.67 to 6.53 eV [92]. In the second article, researchers investigated the composition $Gd_3Sc_2(Al_{3x}Ga_x)O_{12}$ with $x = (1, 2, 3)$ and reported the highest light yield and the shortest scintillation decay time of 24 000 ph / MeV and 12 ns (11%) + 56 ns (89%), respectively, for the sample with $x = 2$ [93].

The complete substitution of Ga creates the possibility of the preparation of GSAG in the Mo crucibles using the micro-pull method, which has been thoroughly investigated and compared to the Ir crucibles by Zapadlík et al. [94] in composition $Gd_{2.88}Sc_{1.89}Al_{3.23}O_{12}$ with concentration Pr^{3+} 0. 1% and 0.1, 0.2 and 0.3% Ce^{3+} concentration. The scintillation decay time of 120 ns (100%) with

excitation by ^{127}Cs and light yield of over 10,000 ph / MeV have been achieved with composition GSAG:Ce0.3% prepared in Mo crucible.

4 Instrumentation

4.1 Sintering process

The sintering process was carried out in the superkanthal heating furnace developed in cooperation with *CLASIC* company. The sintering takes place inside a sapphire tube and could be performed both in vacuum (up to 10^{-6} mbar using a turbomolecular vacuum pump) or in the flow of the preferred atmosphere. The maximum attainable temperature is up to 1800 °C.

4.2 Laser-Diode Floating Zone furnace

The Laser-Diode Floating Zone furnace was already described in the author's bachelor thesis [95]. Single crystal growth was performed using an LDFZ furnace made by the Japanese company *Crystal Systems Corporation*. The model *FZ-LD-5-200W-VPO-PC_EG* is equipped with five laser-diode units of power 200 W each. Laser units can be moved forward and backward to focus on the surface of the melt zone and to compensate for the different diameters of grown crystal. There is also the possibility of tilting the laser-diode units up to 35 °, which is used for special modes of growth.

The movement is performed with an upper and lower moving rod. The movement during growth could be set at range 0.1 – 300 mm/h, during preparation there is a possibility of fast movement up to 150 mm/min. During growth, it is customary to use counter-rotation of both rods and a moving speed of approximately 1 mm/h.

The growth chamber is capable of withstanding a vacuum and a pressure of up to 0.95 MPa. The moving rods are sealed with an O-ring. The maximum pressure and flow of the working gas are continuously adjustable. The visual inspection of the growing single crystal is realised by a camera with an automatic aperture. Inside the furnace there is a pyrometer which can work in not only the continuous mode but also the scanning mode. The pyrometer can snap the temperature profile of 50 mm in both upper and lower directions from the melt zone and can provide useful information on the temperature profile of the hot zone, the growing single crystal, and the distribution of heat inside the precursor. The absolute value of the temperature measured by the pyrometer is dependent on the emissivity of the measured surface, which must be entered into the system. The values of emissivity can be found in the literature or empirically determined by melting point of the material.

The cooling system of the furnace is ensured using two chillers responsible for cooling of laser-diode units and absorbers.

The control unit consists of the lower part with laser-diode units power sources, the central part with computer using for the control of furnace power, tilting of laser-diode units, and rotation and pulling speeds of both the seed and the grown crystal parts. The upper part controls the flow of the working gas into the chamber.

The furnace itself is divided into three parts: upper and lower parts with motors for both rotation and pulling of the rods on which the seed and grown

crystals are placed, and the centre part, where laser-diode units, absorbers, gas chamber, its lighting, and the pyrometer are located.

4.2.1 Passive afterheater

We managed to operate the laser furnace with a passive afterheater made of rhodium-platinum alloy. The passive afterheater is a tube with diameter of 10 mm and height of 25 mm placed directly under the hot zone of the furnace. Part of the thermal radiation is reflected back into the grown crystal and absorbed. As we showed[95, 96] this results in a reduction in the temperature gradient and thus in a better optical quality of the crystal mainly in terms of the number of cracks in the grown single crystal.

4.2.2 Active afterheater

The temperature gradient using the passive afterheater is still very high and leads to a number of cracks in the grown single crystals of the GGAG and GSAG materials. The logical next step is the improvement of the passive afterheating with an active heating unit, which we realised through the platinum coil heated by the electrical current releasing Joule heat.

The ceramic extension placed on the top part of the passive afterheater containing the platinum coil was made by CLASIC company. Electrical contacts were pulled out of the gas chamber using vacuum-compatible components and connected to the power source. The electrical current is adjustable. The setup is shown in Figure 4.1.

4.3 Measurement of optical properties

Absorption spectra were measured using the Shimadzu 3101PC near-VIS (UV/VIS/NIR) spectrophotometer in the range 190-800 nm. Radioluminescence (RL), photoluminescence excitation (PLE), and photoluminescence emission (PL) spectra and PL decay curves were measured by a custom-made spectrofluorometer

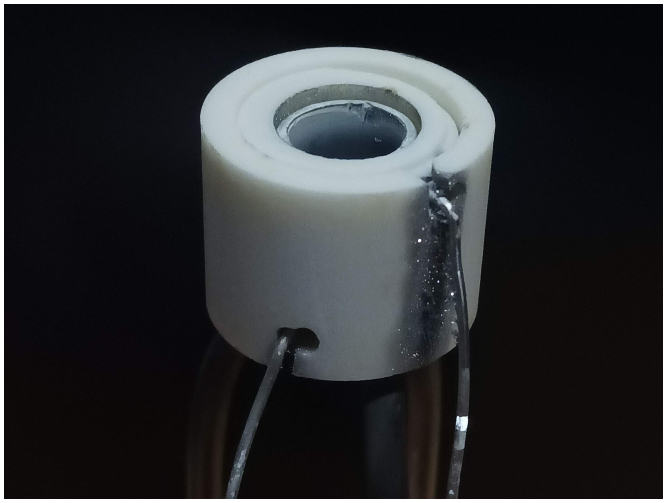


Figure 4.1 Active afterheater setup.

5000M (Horiba Jobin Yvon, Wildwood, MA, USA) using a W X-ray tube (40 kV, 15 mA, Seifert), steady-state xenon lamp (EQ-99X LDLS - Energetic, a Hamamatsu Company), and nanosecond nanoLED pulsed light sources (fast decays measured by time-correlated single-photon counting technique, Hamamatsu) as the excitation sources, respectively. The detection part of the setup involved a single-grating monochromator and a photon-counting detector TBX-04 (IBH Scotland). The measured spectra were corrected for the spectral dependence of the detection sensitivity (RL, PL) and of the excitation energy (PLE). The convolution procedure was applied to the photoluminescence and scintillation decay curves to determine true decay times (SpectraSolve software package, Ames Photonics). For every RL spectrum, the standard BGO crystal scintillator ($Bi_4Ge_3O_{12}$) was measured under the same experimental conditions to obtain quantitative intensity information.

A routine spectrally unresolved scintillation decay was measured by means of fast photomultiplier (PMT) R7207-01, Hamamatsu working in the current regime, and Keysight InfiniiVision DSOX6002A digital oscilloscope where the sample was optically coupled directly to the PMT photocathode.

Scintillation light yield (LY) was determined by the pulse height spectroscopy of scintillation response, using the HPMT (Hybrid Photomultiplier) model DEP PPO 475C, spectroscopy amplifier ORTEC model 672 (shaping time t = 1 μs) and multichannel buffer ORTEC 927TM. The sample was optically coupled to HPMT using a silicon grease; several layers of Teflon tape were put over the sample as a reflector. Photoelectron yield (LY) was obtained from the Gaussian fit of the photopeak in the pulse-height spectra. Quantum efficiency for both samples was calculated using RL spectra. Finally, light yield was calculated:

$$LY = PhY/QE. \tag{4.1}$$

5 Preparation of single crystals

5.1 GGAG single crystals

5.1.1 Powder precursor

The starting materials for the preparation of the GGAG:Ce,Mg single crystals were the oxides: Gd_2O_3 (99.999 %, Alfa Aesar), Ga_2O_3 (99. 999 % of the Slovak firm OMK Žarnovica), Al_2O_3 (99. 997 %, Alfa Aesar), CeO_2 (99,99 %) and MgO (99.998 %, Alfa Aesar). The precursors were prepared from a sintered mixture of oxides of the starting composition $Gd_{2.985}Ce_{0.015}Ga_{2.7}Al_{2.3}O_{12}$ or $Gd_{2.9847}Ce_{0.015}Mg_{0.0003}Ga_{2.7}Al_{2.3}O_{12}$. The sintering process was as follows: 1160°C/14h + twice 1170 °C/18h + 1450 °C/24h; between individual steps the material was remixed in an agate mortar.

5.1.2 Rod precursor preparation

The polycrystalline rod precursor is necessary for the single-crystal growth by a floating zone, and its quality is fundamental for the achievement of stable and reproducible growth. The steel form (as described [95, 96]) with an inner diameter of 8 mm was placed in a vacuum chamber to stretch out the inner flexible latex capsule. The capsule was gradually filled with approximately 5 mm steps by a powder precursor, regularly compressed by a piston since its fullness, and closed by a silicon plug on top. The vacuum was then unsealed, the steel form was disassembled, and the entire latex capsule was pulled out. In the next step, the latex form was compressed in a monostatic press for 20 minutes at a pressure of 2 t/cm^2. The compressed precursor rod was sintered in superkanthal furnaces protected by insertion into a sapphire tube in a flowing oxygen atmosphere of 0.05 l / min. The precursor was always pre-sintered at 800 °C for 12 hours, cooled to drill a hole for the holder, and then sintered at 1450 °C for 24 hours. The temperature profiles of pre-sintration and sintration are shown in Figure 5.1.

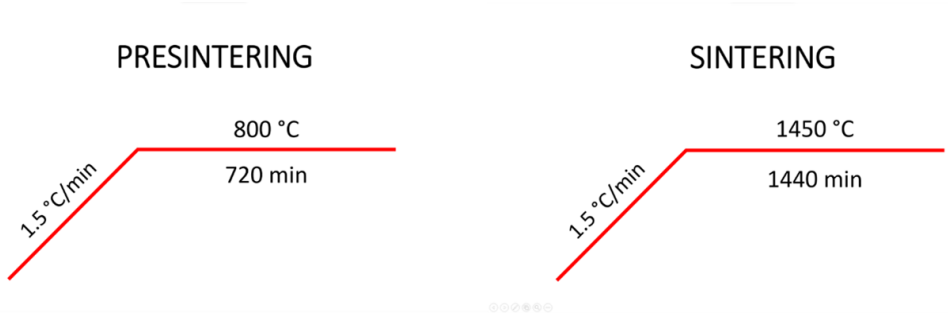


Figure 5.1 Presintering and sintering temperature profiles of GGAG and GSAG rod precursors.

5.1.3 Growth of single crystals

The experiments were carried out in a laser diode furnace *FZ-LD-5-200W-VPO-PC-EG* from Crystal Systems Corporation, Japan, equipped with 5x200 W laser diode units surrounding the hot zone in the horizontal plane. The diodes produce near-infrared radiation of wavelength $\lambda = (976 \pm 5)$ nm of the 4x8 mm^2 beam spot. In LDF a pyrometer is installed on a lift that operates in the range ± 40 mm below and above the hot zone. We used an empirical value of the emissivity 0.870 calibrated by the melting point of Nd:YAG at 1970°C.

Commercial single crystals of GGAG produced by Crytur Company were used as seed. The growth processes were carried out at O_2 pressure 0.3 MPa. During the connection of the precursor rod to the seed crystal, a small portion of $Ar + 5\%H_2$ was added to the atmosphere, initiating the melting.

In all growth cycles, we used an afterheater, which consists of the stage and the central upper tube surrounding the single crystal just below the hot zone, both made of alloy Pt/Rh to be resistant to oxygen. The compact size allows the afterheater to be inserted inside the commercial quartz chamber. The afterheater is fixed in the bottom on a screw with a low pitch for a precise location, typically 2-3 mm below the laser beams. The operation principle is based on the back reflection of the IR radiation from the hot zone into the grown single crystal. The installation inside the laser furnace is possible because of the very precise focus of the laser beams; even at maximum power, the lasers cannot melt the material of the afterheater located 2-3 millimeters below the hot zone. The arrangement can be seen in Figure 5.2a. The example of a single crystal prepared is shown in Figure 5.2b.

5.2 GSAG single crystals

5.2.1 Powder precursor

The starting material for the growth of the GSAG single crystal was mixed of 5N purity oxides (Gd_2O_3, Al_2O_3) and 4N (Sc_2O_3 and CeO_2) to the (various) compositions using agate mortars and pestles. The material was then repeatedly heated at temperatures of 1160 °C – 1450°C and re-mixed, which led, according to X-ray analysis, to the formation and increase of the garnet phase content in the mixture. The process was finished when, in the XRD spectra, the ratio of the heights of the dominant peaks of the main foreign phase, perovskite $GdAlO_3$, and the garnet phase, decreased to under 0.1.

5.2.2 Rod precursor preparation

Polycrystalline precursor rods were prepared by an identical procedure as in reference [95, 96] from a powder precursor described above. Both pre-sintering and final sintering of the precursor rods inserted in pure sapphire tubes took place in flowing O2 at a rate of 0.07 l/min of ambient pressure. The temperature profiles of both processes were same as for GGAG rod precursors and are shown in Figure 5.1.

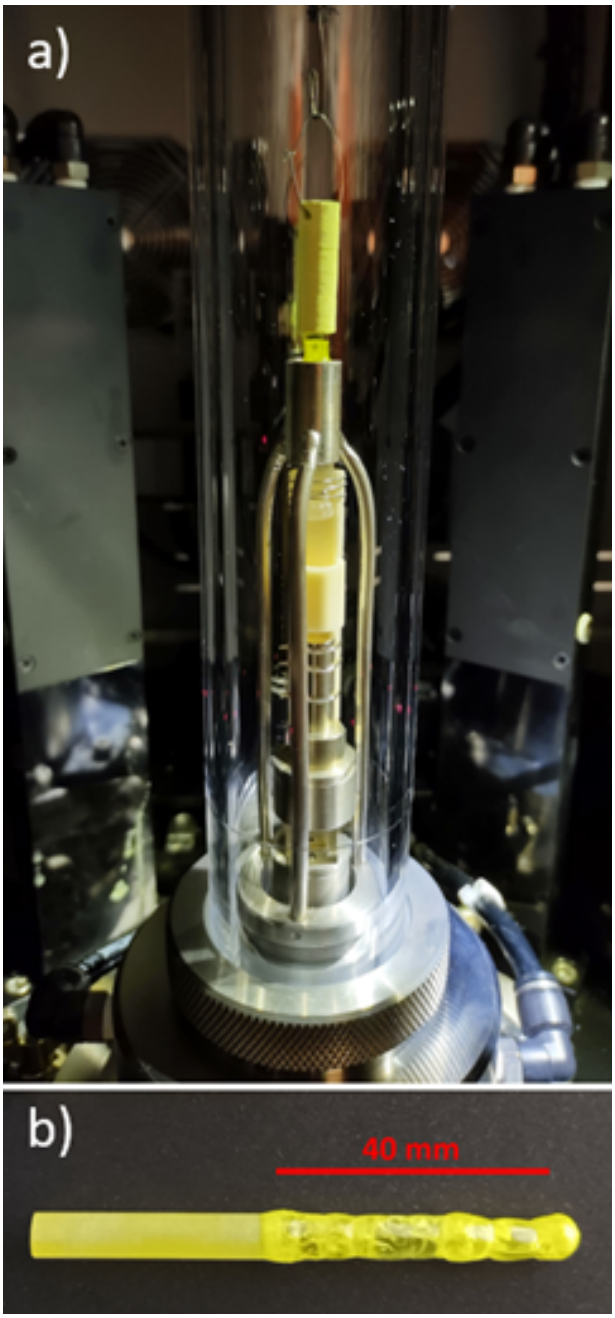


Figure 5.2 **a)** Arrangement of afterheater, rod precursor and seed crystal in LDFZM furnace. **b)** The example of GGAG single crystal prepared.

5.2.3 Growth of single crystals

A single crystals of GSAG have been prepared in a laser diode furnace (LDF) $FZ - LD - 5 - 200W - VPO - PC - EG$ from Crystal Systems Corporation, Japan, in arrangement with a passive Pt/Rh afterheater described elsewhere [95, 96]. The single crystal / melt interface at the bottom of the hot zone was approximately 1 mm above the afterheating edge - see Figure 5.3. The growing process was performed using a focusing lens, which reduced the spot size of each laser diode to a 4 x 4 mm^2 beam profile.

The single crystal was grown on an orientated seed rod in a crystallographic direction $\langle 100 \rangle$. The growth process was carried out at an oxygen overpressure of 0.4 MPa. To initiate the melting of the precursor using monochromatic lasers of wavelength $\lambda = (810 \pm 10)$ nm, a mixture of $Ar + 5\%H_2$ had to be injected into the quartz chamber for a couple of minutes.

The growth rate was 2.0 mm/h, while the precursor rod fed the hot zone at 1.6 mm/h. The majority of the growth was performed at a power that oscillated around the value of 610 W. We rotated the seed/precursor rod at 45/10 rpm counter-rotation. During growth, the diameter of the grown single crystal was very unstable as a result of bubble formation in the melt. Bubbles caused inflation of the hot zone that led to a wider diameter of the grown single crystal. When the bubbles burst, the hot zone narrowed in shock, leading to a lower diameter of the grown single crystal. The origin of the bubbles is apparently not in the low quality of the sintered rod precursor because they occur just above the single-crystal/melt interface.

We suppose an equilibrium between the oxygen dissolved in the melt and the composition of the single crystal. We have not found any way to suppress the formation of these bubbles. Examples of the too-wide hot zone with raised bubbles, the narrow hot zone after the bubble burst, and the ideal shape of the hot zone are shown in Figure 2. Nevertheless, we have found that the creation of bubbles stabilises (or already small bubbles very effectively burst) when the diameter of the single crystal is about 1/3 lower than the polycrystalline precursor, and the hot zone has a shape of a regular trapezoid.

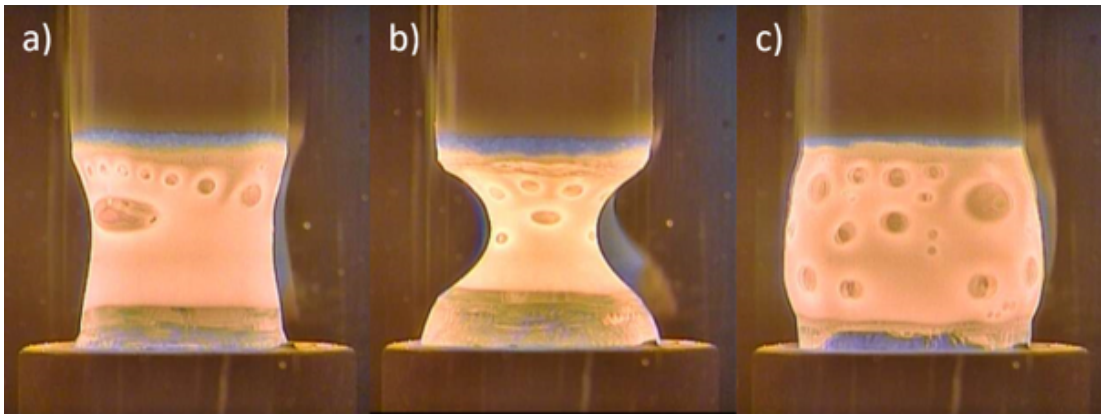


Figure 5.3 The shape of hot zone during GSAG growth **a)** ideal **b)** too narrow **c)** too wide. The visible bubbles are unwanted at every case and are directly responsible for the irregular diameter of the single crystal and consequent creation of the cracks

6 Characterization of single crystals

6.1 GGAG

Of the four GGAG crystals, a total of 22 samples were prepared. Where possible, 2 discs with a thickness of approximately 1 mm were cut from the beginning, middle, and end of each single crystal. The necessary work was performed by technicians in the Optical and Mechanical Workshops of the Institute of Physics of the Czech Academy of Sciences, Na Slovance 1999/2, 182 00 Praha 8. The samples were then measured in the Department of Optical Materials of the Institute of Physics, Czech Academy of Sciences, Cukrovarnická 10/112 162 00 Praha 6. Measurement was performed according to the methodology described in 4.3 Measurement of optical properties. In table 6.1 Measured samples of GGAG, there is a list of all the samples prepared and measured.

#	Sample	Precursor	Composition	Date of growth
1	6 start	MFF6	Gd 2.985 Ce 0.015 Ga 2.7 Al 2.3 O 12	02.06.2022
2	6 start	MFF6	Gd 2.985 Ce 0.015 Ga 2.7 Al 2.3 O 12	02.06.2022
3	6 mid	MFF6	Gd 2.985 Ce 0.015 Ga 2.7 Al 2.3 O 12	02.06.2022
4	6 mid	MFF6	Gd 2.985 Ce 0.015 Ga 2.7 Al 2.3 O 12	02.06.2022
5	6 end	MFF6	Gd 2.985 Ce 0.015 Ga 2.7 Al 2.3 O 12	02.06.2022
6	6 end	MFF6	Gd 2.985 Ce 0.015 Ga 2.7 Al 2.3 O 12	02.06.2022
7	4 start	MFF4	Gd 2.985 Ce 0.015 Ga 2.7 Al 2.3 O 12	23.05.2022
8	4 start	MFF4	Gd 2.985 Ce 0.015 Ga 2.7 Al 2.3 O 12	23.05.2022
9	4 end	MFF4	Gd 2.985 Ce 0.015 Ga 2.7 Al 2.3 O 12	23.05.2022
10	4 end	MFF4	Gd 2.985 Ce 0.015 Ga 2.7 Al 2.3 O 12	23.05.2022
11	5 start	MFF5	Gd 2.985 Ce 0.015 Ga 2.7 Al 2.3 O 12	27.05.2022
12	5 start	MFF5	Gd 2.985 Ce 0.015 Ga 2.7 Al 2.3 O 12	27.05.2022
13	5 mid	MFF5	Gd 2.985 Ce 0.015 Ga 2.7 Al 2.3 O 12	27.05.2022
14	5 mid	MFF5	Gd 2.985 Ce 0.015 Ga 2.7 Al 2.3 O 12	27.05.2022
15	5 end	MFF5	Gd 2.985 Ce 0.015 Ga 2.7 Al 2.3 O 12	27.05.2022
16	5 end	MFF5	Gd 2.985 Ce 0.015 Ga 2.7 Al 2.3 O 12	27.05.2022
17	2 start	MFF2	Gd 2.985 Ce 0.015 Mg 0.0003 Ga 0.27 Al 2.3 O 12	21.06.2022
18	2 start	MFF2	Gd 2.985 Ce 0.015 Mg 0.0003 Ga 0.27 Al 2.3 O 12	21.06.2022
19	2 mid	MFF2	Gd 2.985 Ce 0.015 Mg 0.0003 Ga 0.27 Al 2.3 O 12	21.06.2022
20	2 mid	MFF2	Gd 2.985 Ce 0.015 Mg 0.0003 Ga 0.27 Al 2.3 O 12	21.06.2022
21	2 end	MFF2	Gd 2.985 Ce 0.015 Mg 0.0003 Ga 0.27 Al 2.3 O 12	21.06.2022
22	2 end	MFF2	Gd 2.985 Ce 0.015 Mg 0.0003 Ga 0.27 Al 2.3 O 12	21.06.2022

Table 6.1 Measured samples of GGAG.

6.1.1 Absorption spectra

Room temperature (RT) absorption spectra of GGAG samples are shown in Figure 6.2. Distinct structures are observable within the examined spectral range, including:

i. well resolved transitions of Ce^{3+} $4f \rightarrow 5d^1$ at 443 nm and Ce^{3+} $4f \rightarrow 5d^2$ at 341 nm



Figure 6.1 Cut samples of GGAG.

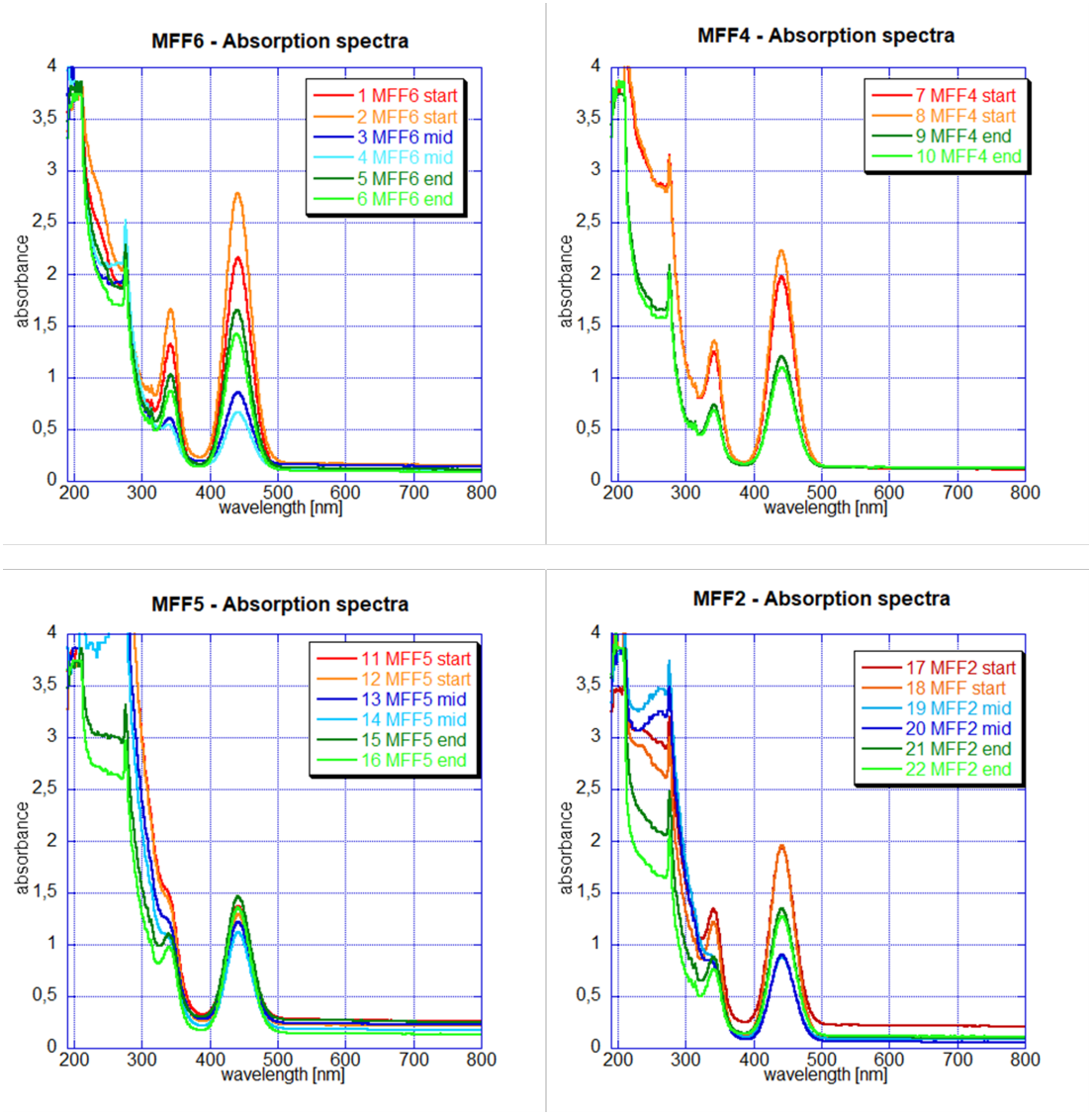


Figure 6.2 Absorption spectra of GGAG samples.

ii. sharp absorption peaks at 276 nm and 305-312 nm attributed to ${}^8S_{7/2} \rightarrow {}^6 I_x$ and ${}^8S_{7/2} \rightarrow {}^6 P_x$ transitions of Gd^{3+} ions, respectively

iii. codoping with Mg results in the appearance of the broad band attributed to the Ce^{4+} charge transfer absorption transition between 220 nm and 350 nm [61, 7, 97, 98]. However, charge transfer absorption can be observed in all samples, which could be explained by stabilisation of Ce^{4+} due to the pressurised oxygen atmosphere during the growth process.

iv. bandgap edge can be seen at 210 nm, well in correspondence with previously published data [80]

Absorption spectra of the samples from single-crystal MFF5 exhibit anomalous absorption at 340 nm. This behaviour can be explained by the presence of colour centres, which are not connected to Ce, as previously observed and studied in YAG [13].

6.1.2 Radioluminescence spectra

RT luminescence spectra of the GGAG samples are presented and compared to the standard BGO scintillator measured under the same geometric conditions, in Figure 6.3. An emission band originating from the Ce^{3+} $5d^1 \rightarrow 4f$ transition is observed at 525 nm [72]. The spectra integrals compared to the BGO standard samples are compared in Table 6.2

6.1.3 Scintillation decay

Figure 6.4 display two examples of spectrally unresolved scintillation decays of GGAG samples excited by the ^{137}Cs radioisotope source (662 keV). The decay curves are approximated by the sum of two exponentials in the following form:

$$I(t) = \sum_{i=1}^{2} A_i e^{-\frac{t}{\tau_i}} + background \tag{6.1}$$

where A_i and τ_i are the amplitude of the i-th component and decay time of the i-th component, respectively. The portion of the light released by the i-th component, commonly referred to as the light sum (LS_i), can be calculated as:

$$LS_i = \frac{A_i \tau_i}{\sum_{i=1}^{2} A_i \tau_i} \tag{6.2}$$

The values of light sum for each component are provided in Table 6.2. The scintillation response in Mg codoped material is faster, as indicated by shorter decay time constants and higher light sum for the fast component. This acceleration is attributed to Mg codoping which stabilizes Ce^{4+} in higher concentration, consistent with [61, 72]. Nevertheless, the decay in the Mg-free sample is significantly faster compared to the Czochralski grown sample with the same host composition [72] which can be explained by stabilization of Ce^{4+} center due to the oxygen-rich growth atmosphere.

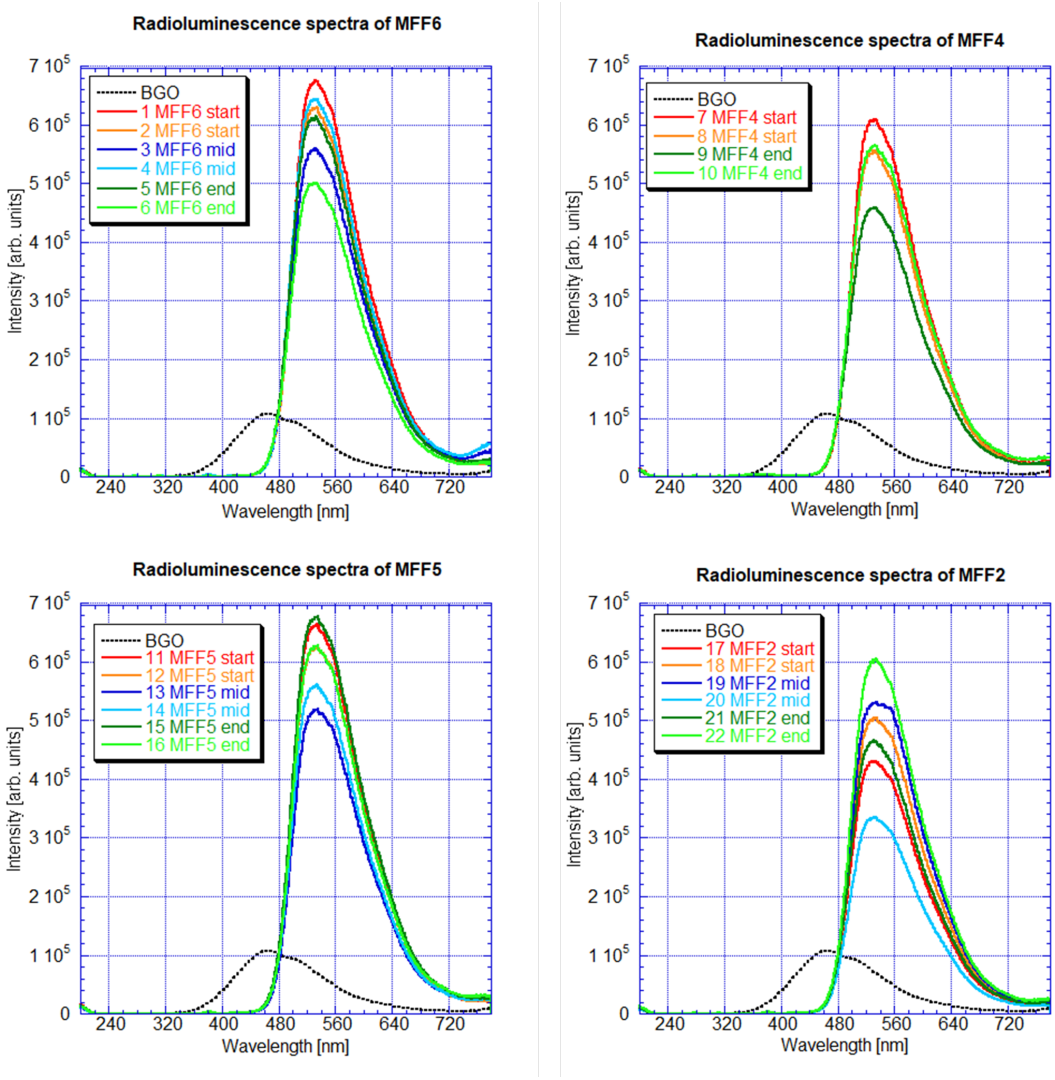


Figure 6.3 Radioluminescence spectra of GGAG samples.

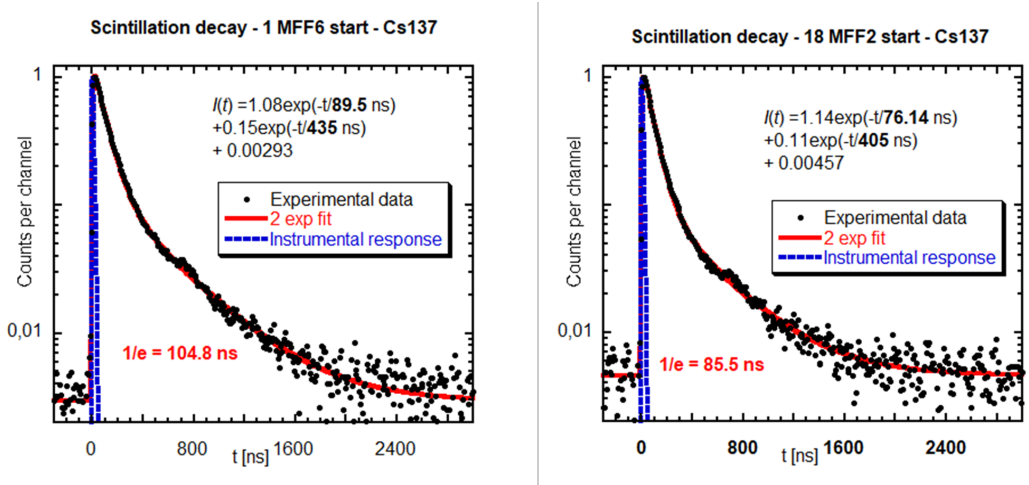


Figure 6.4 Scintillation decays of GGAG MFF6 start and MFF2 start samples.

Sample	Scintillation decay				LY	Photoluminescence decay				Integral LY
	1 [ns]	LS1 [%]	2 [ns]	LS2 [%]	[ph/keV]	1 [ns]	LS1 [%]	2 [ns]	LS2 [%]	[%BGO]
6 start	89.5	60	435	40	**43.7**	49.5	85	93	15	485
6 start	90.5	63	408	37	**42.0**	51.5	95	163	5	447
6 mid	65.8	54	514	46	**36.3**	49.1	81	83	19	413
6 mid	64.4	55	517	45	**35.4**	49.2	84	86	16	473
6 end	73.8	53	437	47	**35.6**	48.8	84	90	16	443
6 end	71.7	49	447	51	**39.5**	48.3	82	89	18	366
4 start	76.2	62	425	38	**38.1**	49.2	88	93	12	434
4 start	74.1	61	403	39	**37.5**	48.4	88	96	12	398
4 end	76.5	50	441	50	**40.5**	49.6	81	86	19	339
4 end	74.9	47	461	53	**38.9**	49.9	83	89	17	420
5 start	58.9	78	415	22	**30.5**	49.8	97	148	3	478
5 start	63.0	74	435	26	**31.1**	50.8	98	164	2	454
5 mid	59.7	72	411	28	**32.7**	50.9	94	112	6	385
5 mid	62.9	71	444	29	**33.0**	50.9	91	99	9	411
5 end	68.4	63	414	37	**37.3**	51.1	89	94	11	493
5 end	69.1	62	439	38	**38.0**	50.1	87	91	13	460
2 start	70.7	65	401	35	**33.8**	50.0	85	86	15	317
2 start	76.1	66	405	34	**38.1**	50.8	86	86	14	370
2 mid	60.9	67	454	33	**32.5**	50.0	84	80	16	402
2 mid	62.5	66	429	34	**32.5**	51.2	88	85	12	248
2 end	69.7	58	435	42	**38.2**	50.3	85	90	15	341
2 end	74.2	53	469	47	**40.3**	50.4	82	87	18	437

Table 6.2 Scintillation and photoluminescence decay time constants, light sums and light yield of GGAG samples.

6.1.4 Light yield

Figure 6.5 presents a comparison of the pulse height spectra between GGAG samples and a BGO and GGAG reference, with a shaping time set to 1 µs. The calculated scintillation light yield values, as well as the RL spectra integrals compared to the standard BGO sample, are provided in Table 6.2.

6.1.5 Afterglow

Figure 6.6 displays the measured and normalised afterglow curves of the GGAG samples, compared to the BGO reference in Figure 6.6. BGO is generally regarded as a scintillator that exhibits an extremely low afterglow that demonstrates almost five orders of magnitude of the decrease in signal intensity after X-ray cutoff [99]. Our samples exhibit a more than three-order-of-magnitude drop in signal intensity after X-ray cutoff, indicating that afterglow is not a detrimental issue in their scintillation performance.

6.1.6 Photoluminescence spectra

The photoluminescence excitation spectra in 6.7, measured at $\lambda_{em} = 530$ nm, are dominated by Ce^{3+} $4f \rightarrow 5d^1$ (443 nm) and $4f \rightarrow 5d^2$ (341 nm) transitions, which are well aligned with the absorption spectra (see Figure 6.2). The photoluminescence emission spectra for the excitation wavelengths 340nm and 400nm, shown in 6.8 and 6.9, respectively, consist of a broad band peaking at 530 nm. This emission originates from the Ce^{3+} $5d^1 \rightarrow 4f$ transition and is in good agreement with the radioluminescence spectra shown in 6.3.

The relatively less effective excitation below 350 nm in GGAG:Ce,Mg is due

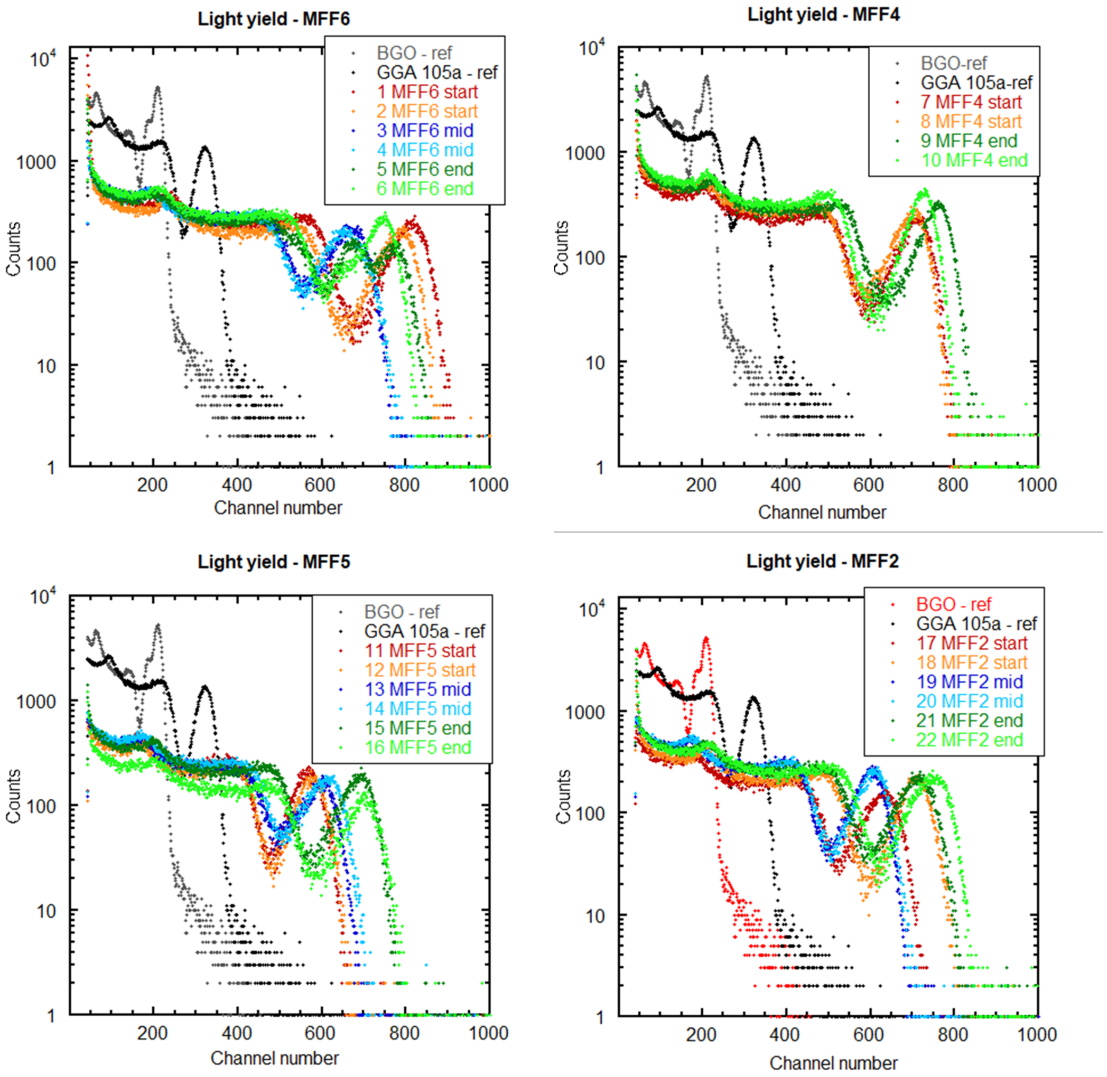


Figure 6.5 Pulse height spectra of GGAG samples and BGO reference, with a shaping time set to 1 µs.

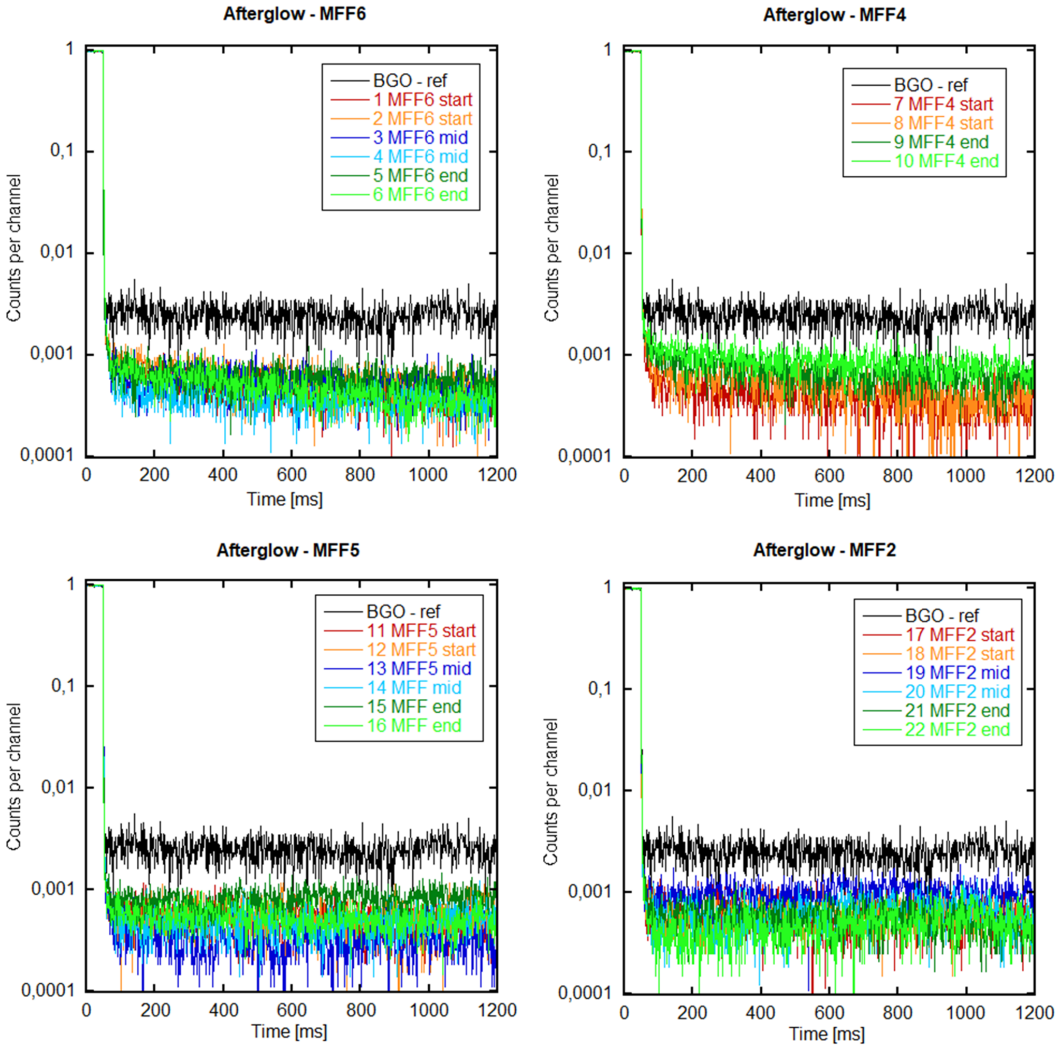


Figure 6.6 Measured and normalised afterglow curves of the GGAG samples, compared to the BGO reference.

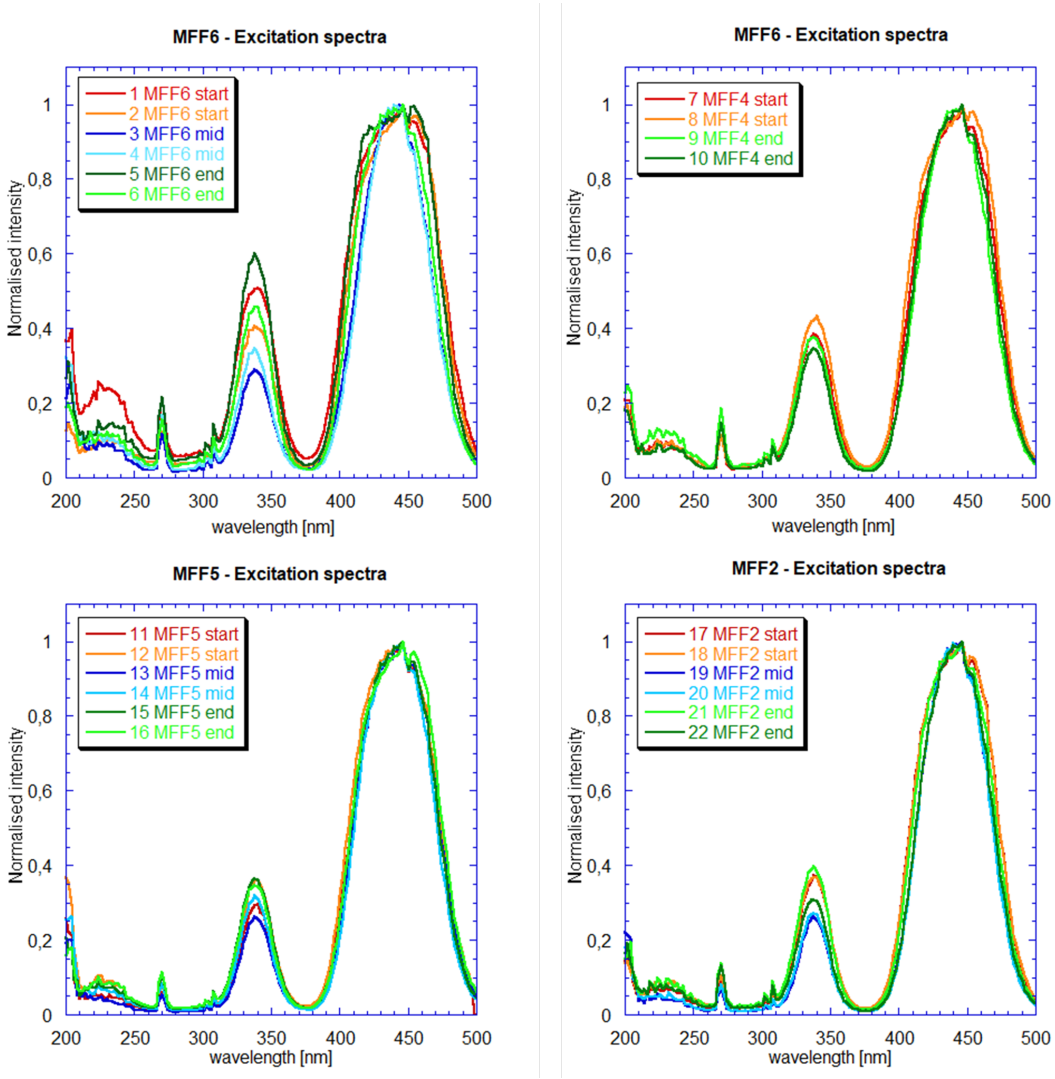


Figure 6.7 Normalised photoluminescence excitation spectra of GGAG samples measured at $\lambda_{em} = 530$ nm.

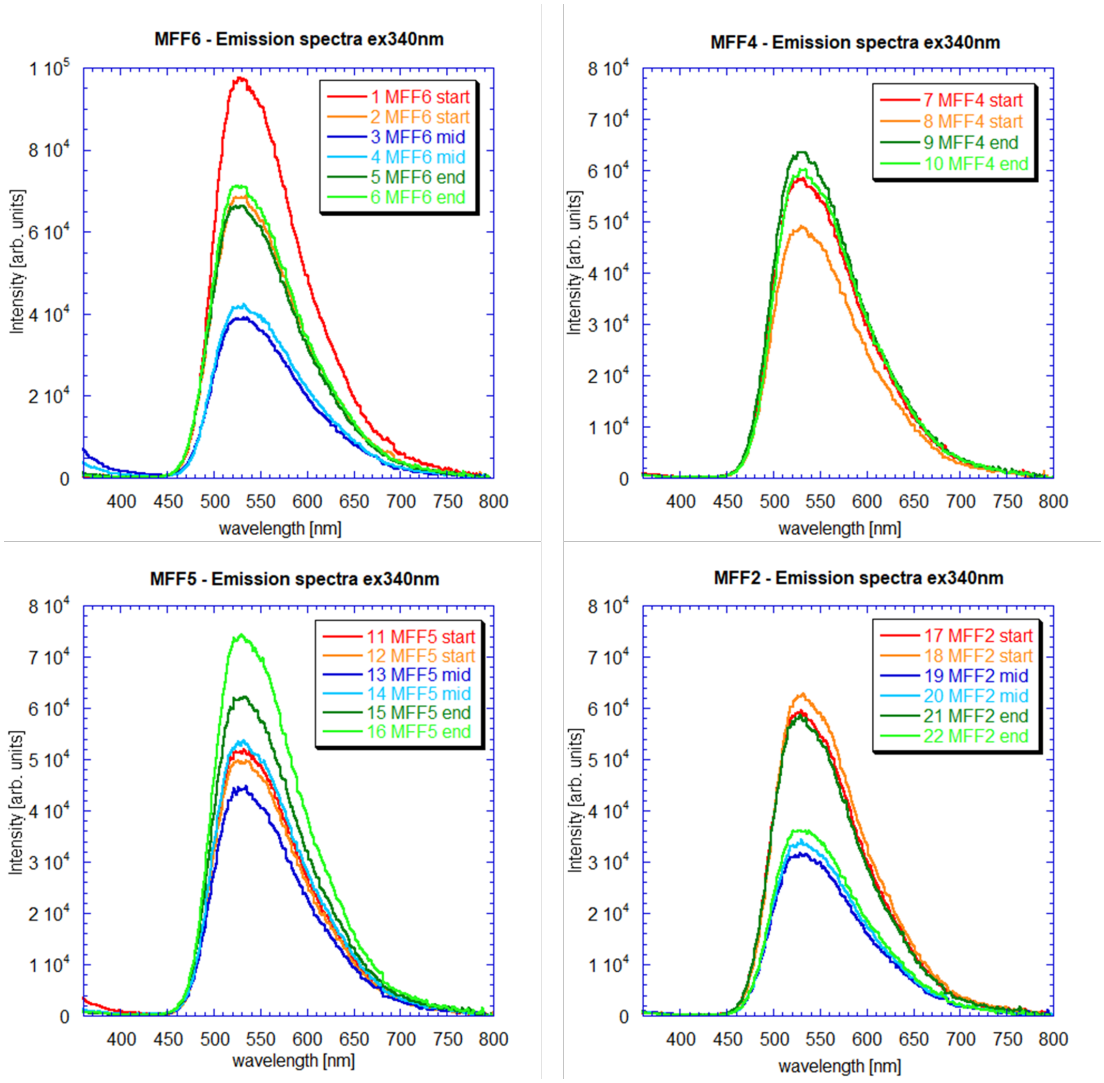


Figure 6.8 Photoluminescence emission spectra of GGAG samples for the excitation wavelengths 340 nm.

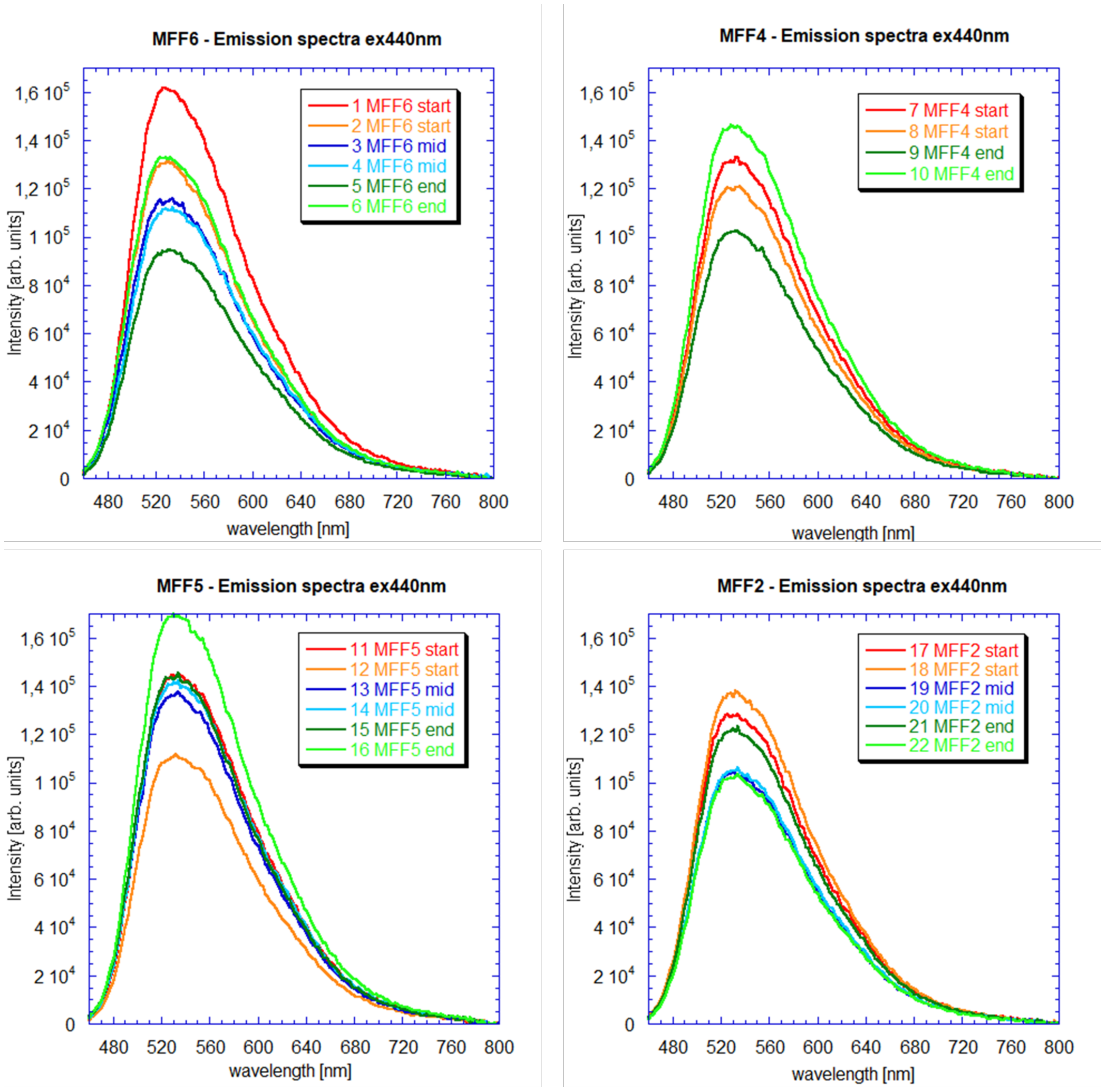


Figure 6.9 Photoluminescence emission spectra of GGAG samples for the excitation wavelengths 440 nm.

to competing charge transfer (CT) absorption with several peaks at 302 – 312 nm and a sharp peak at 270 nm arising from Gd^{3+} $4f \rightarrow 4f$ transitions. The edge of the host band is observable at 205 nm. Excitation to the Ce^{3+} absorption bands, the Gd^{3+} absorption bands, and the edge of the host band in Gd -concentrated garnets doped with Ce^{3+} consistently results in only the Ce^{3+} emission due to efficient energy transfer from the Gd sublattice to the Ce^{3+} dopant [99] and efficient trapping of excitons by Gd cations [100].

6.1.7 Photoluminescence decay

Figures 6.10 show two examples of RT photoluminescence decay curve of the emission Ce^{3+} $4f \rightarrow 5d^1$ ($\lambda_{ex} = 454$ nm, $\lambda_{em} = 530$ nm) of the GGAG samples. The decay times evaluated in Table 2 are very close to the values in the literature taking into account their dependence on the host composition [60, 101].

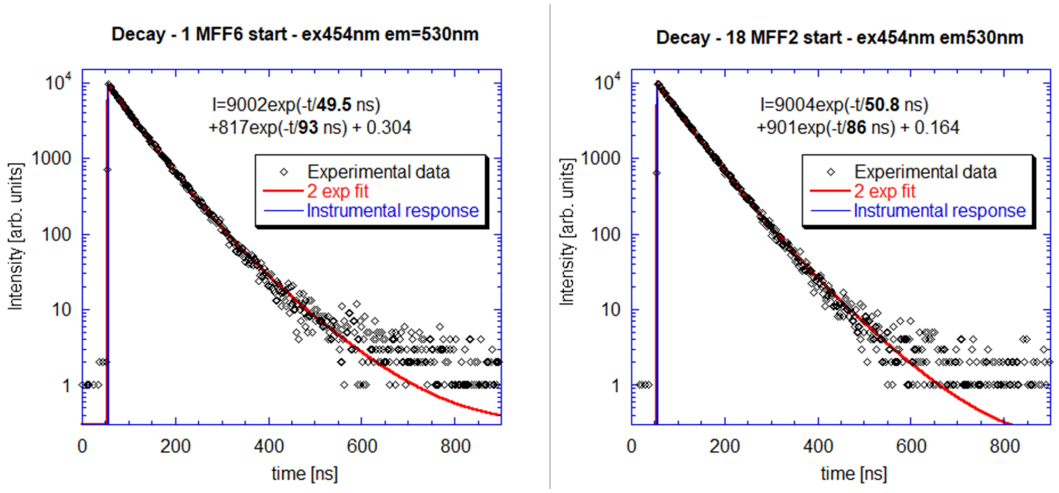


Figure 6.10 Photoluminescence decays of MFF6 1start and MFF2 2start samples from GGAG single crystals measured for $\lambda_{ex} = 454$ nm, $\lambda_{em} = 530$ nm.

6.2 GSAG

From the ten single crystals of GSAG with different compositions, 15 samples were prepared. The discs with a thickness of approximately 1 mm were cut from the parts of single crystal that exhibited the fewest cracks. The necessary work was performed by technicians in the Optical and Mechanical Workshops of the Institute of Physics of the Czech Academy of Sciences, Na Slovance 1999/2, 182 00 Praha 8. The samples were then measured in the Department of Optical Materials of the Institute of Physics of the Czech Academy of Sciences, Cukrovarnická 10/112 162 00 Praha 6. Measurements were performed according to the methodology described in 4.3 Measurement of optical properties.

The optical properties measured in the GSAG samples were unfortunately heavily affected by iron Fe^{3+} contamination, as described and analysed in detail in 7.3 Iron contamination. The only single crystal not affected by iron contamination was GSAG1. During and after preparation and measurement of single-crystal GSAG2-5, precautions are taken in the hope of eliminating contamination. The single crystals GSAG7-8 were prepared with the same composition as the single crystals 2,3 in the hope of repeating growth without contamination. The single crystal GSAG MIX was prepared last, using a mixture of the remaining precursors of GSAG1-3. Unfortunately, the single crystals grown in the second wave were also contaminated with iron. In table 6.3 Measured samples of GSAG, there is a list of all the samples prepared and measured.

#	Sample	Precursor	Composition	Date of growth
1	1 start	GSAG1	Gd2.874 Ce0.006 Sc1.89 Al3.23 O12	17.12.2022
2	2 start	GSAG1	Gd2.874 Ce0.006 Sc1.89 Al3.23 O12	17.12.2022
3	3 end	GSAG1	Gd2.874 Ce0.006 Sc1.89 Al3.23 O12	17.12.2022
4	4 end	GSAG1	Gd2.874 Ce0.006 Sc1.89 Al3.23 O12	17.12.2022
5	LUMIR	GSAG2	Gd2.871 Ce0.006 Mg0.003 Sc1.89 Al3.23 O12	13.03.2023
6	MARCEL	GSAG2	Gd2.871 Ce0.006 Mg0.003 Sc1.89 Al3.23 O12	20.03.2023
7	CECIL	GSAG3	Gd2.835 Ce0.03 Mg0.015 Sc1.89 Al3.23 O12	04.04.2023
8	DALIBOR	GSAG4	Gd2.749 Lu0.245 Ce0.006 Sc1.6 Al3.4 O12	17.04.2023
9	ERNEST	GSAG5	Gd2.904 Ce0.006 Sc1.57 Al3.52 O12	24.04.2023
10	HILBERT	GSAG7	Gd2.871 Ce0.006 Mg0.003 Sc1.89 Al3.23 O12	09.09.2023
11	HUGO	GSAG8	Gd2.835 Ce0.03 Mg0.015 Sc1.89 Al3.23 O12	12.01.2024
12	BOSS	GSAG8	Gd2.835 Ce0.03 Mg0.015 Sc1.89 Al3.23 O12	17.01.2024
13	MAXA	GSAGMIX	Gd2.859 Ce0.014 Mg0.007 Sc1.89 Al3.23 O12	19.06.2023
14	MAXB	GSAGMIX	Gd2.859 Ce0.014 Mg0.007 Sc1.89 Al3.23 O12	19.06.2023
15	MAXC	GSAGMIX	Gd2.859 Ce0.014 Mg0.007 Sc1.89 Al3.23 O12	19.06.2023

Table 6.3 Measured samples of GSAG.

6.2.1 Absorption spectra

The RT absorption spectra of GSAG samples are shown in 6.11. All spectra exhibit well-resolved transitions of Ce^{3+} $4f \rightarrow 5d^1$ at 443 nm, and most also show Ce^{3+} $4f \rightarrow 5d^2$ at 341 nm. When visible, the sharp absorption peaks at 276 nm and 305-312 nm are attributed to of ${}^8S_{7/2} \rightarrow {}^6I_x$ and ${}^8S_{7/2} \rightarrow {}^6P_x$ transitions of Gd^{3+} ions, respectively.

The position of the edge of the bandgap varies significantly between samples depending on the level of Fe^{3+} contamination. For the GSAG1, GSAG4-5, GSAG7

and GSAGMIX single-crystals, the bandgap edge is observed at 210 nm, well in correspondence with previously published data [80]. However, for GSAG3 and GSAG8, a shift of the band gap edge is observed to 330 nm, which can be attributed to the Fe^{3+} impurities [102, 103].

Some samples exhibit anomaly low absorption under the bandgap. This is most pronounced in samples GSAG2-3, but GSAG7 and GSAGMIX are also affected. This is likely an instrumentation defect; because of the poor quality of the samples, cracks may have scattered light, resulting in lower measured absorption.

All single-crystal absorption spectra show absorption below 340 nm caused by the stabilization of Ce^{4+}, due to growth in a pure oxygen atmosphere. Additional absorption, mainly in GSAG2-5 and GSAGMIX, can be explained by the presence of color centers, not associated with Ce, as previously observed and studied in YAG [13].

The absorption spectrum of the sample GSAGMIX MAXC is inconclusive as a result of the poor optical quality of the sample.

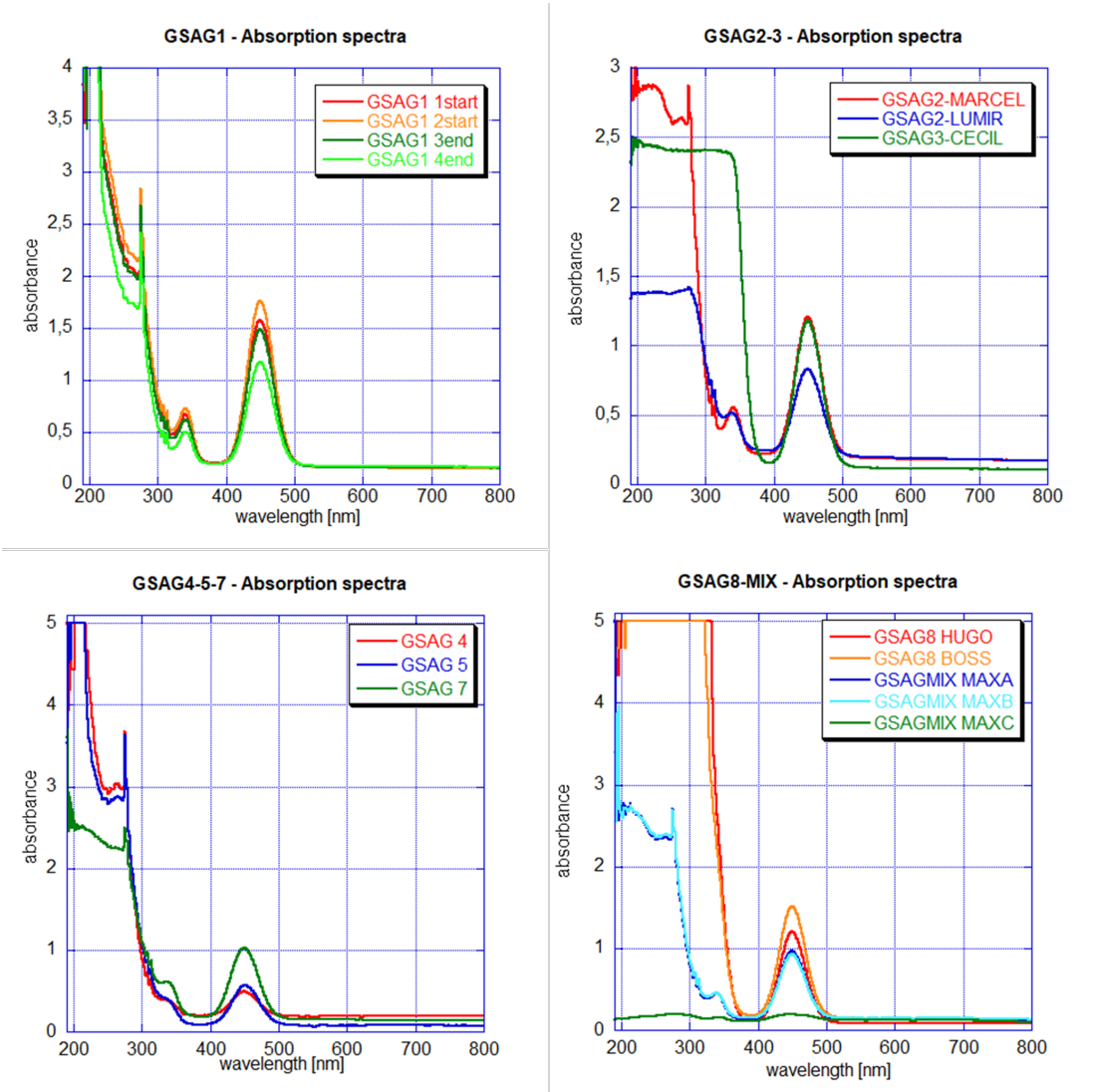


Figure 6.11 Absorption spectra of GGAG samples.

6.2.2 Radioluminescence spectra

The RT radioluminescence spectra in 6.12 are dominated by Ce^{3+} luminescence due to the $5d^1 \rightarrow 4f$ transition, peaking at 553 nm [24]. Furthermore, there are tiny emission lines from $4f \rightarrow 4f$ transitions of Gd^{3+} at 277 nm ($^6I_x \rightarrow^8 S_{7/2}$) and 313 nm ($^6P_x \rightarrow^8 S_{7/2}$), as well as Tb^{3+} (accidental impurity of powder raw material Gd_2O_3) at 381 nm ($^5D_3 \rightarrow^7 F_6$) and 414 nm ($^5D_3 \rightarrow^7 F_5$) which we show in detail for GSAG1 in 6.13. The spectra integrals are compared to the BGO standard samples in Table 6.4.

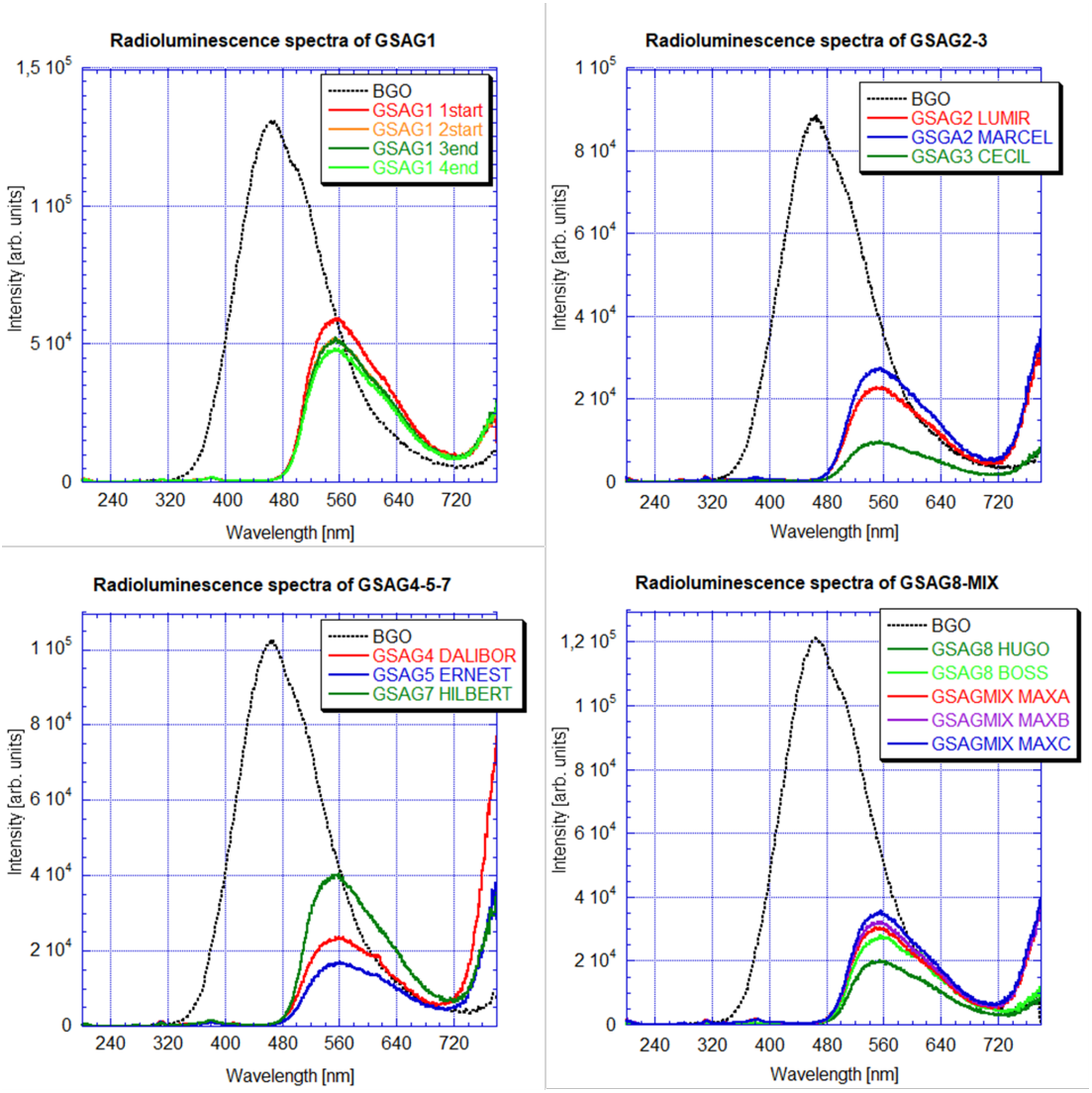


Figure 6.12 Radioluminescence spectra of GSAG samples.

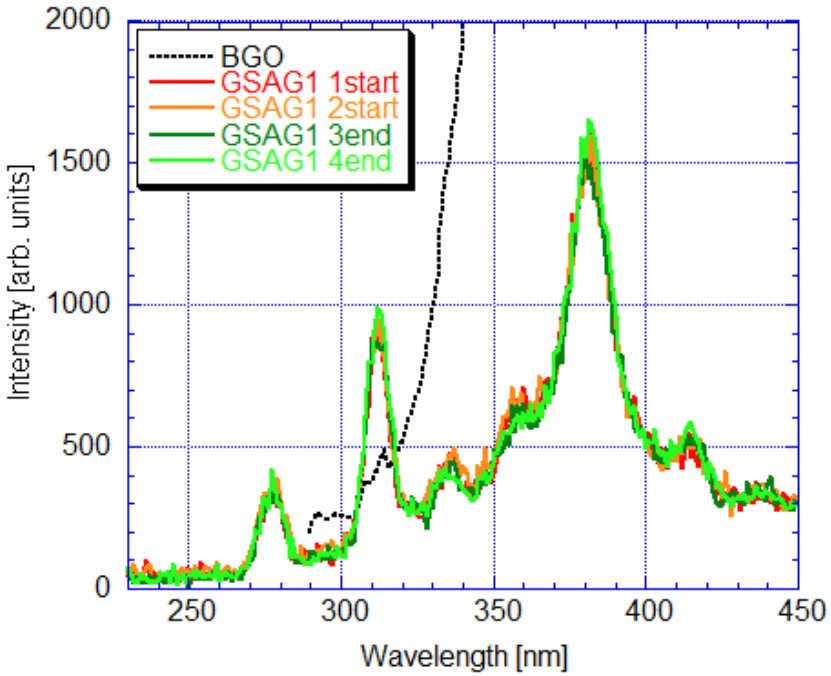


Figure 6.13 Detail of radioluminescence spectra for GSAG1 samples.

6.2.3 Scintillation decay

Figure 6.14 show two examples of the spectrally unresolved scintillation decays of GSAG samples excited by the ^{239}Pu radioisotope source. The decay curves are approximated by the sum of two exponentials in the following form:

$$I(t) = \sum_{i=1}^{2} A_i e^{-\frac{t}{\tau_i}} + background \tag{6.3}$$

where A_i and τ_i are the amplitude of the i-th component and decay time of the i-th component, respectively. The portion of the light released by the i-th

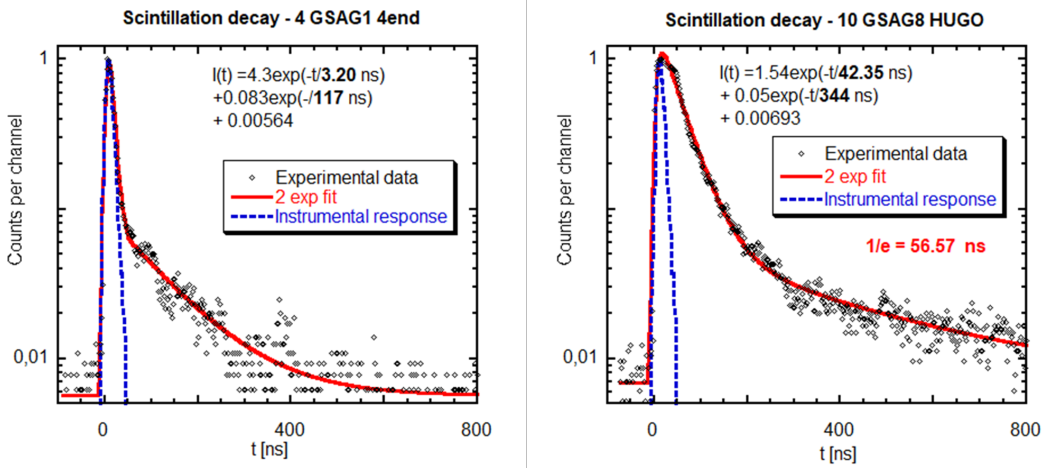


Figure 6.14 Scintillation decays of GSAG1 4end and GSAG HUGO samples.

component, which is commonly called a light sum (LS_i), can be calculated as:

$$LS_i = \frac{A_i \tau_i}{\sum_{i=1}^{2} A_i \tau_i} \tag{6.4}$$

The values of the light sum for each component are in Table 6.4.

6.3 Light yield

Calculated scintillation light yield values as well as the RL spectra integrals compared to the BGO standard sample are shown in Table 6.4.

6.3.1 Afterglow

The measured and normalized afterglow curves of the samples are shown and compared with the BGO reference in Figure 6.15. Our best sample (GSAG 3end) approaches three orders of magnitude signal drop after 100 ms from the X-ray

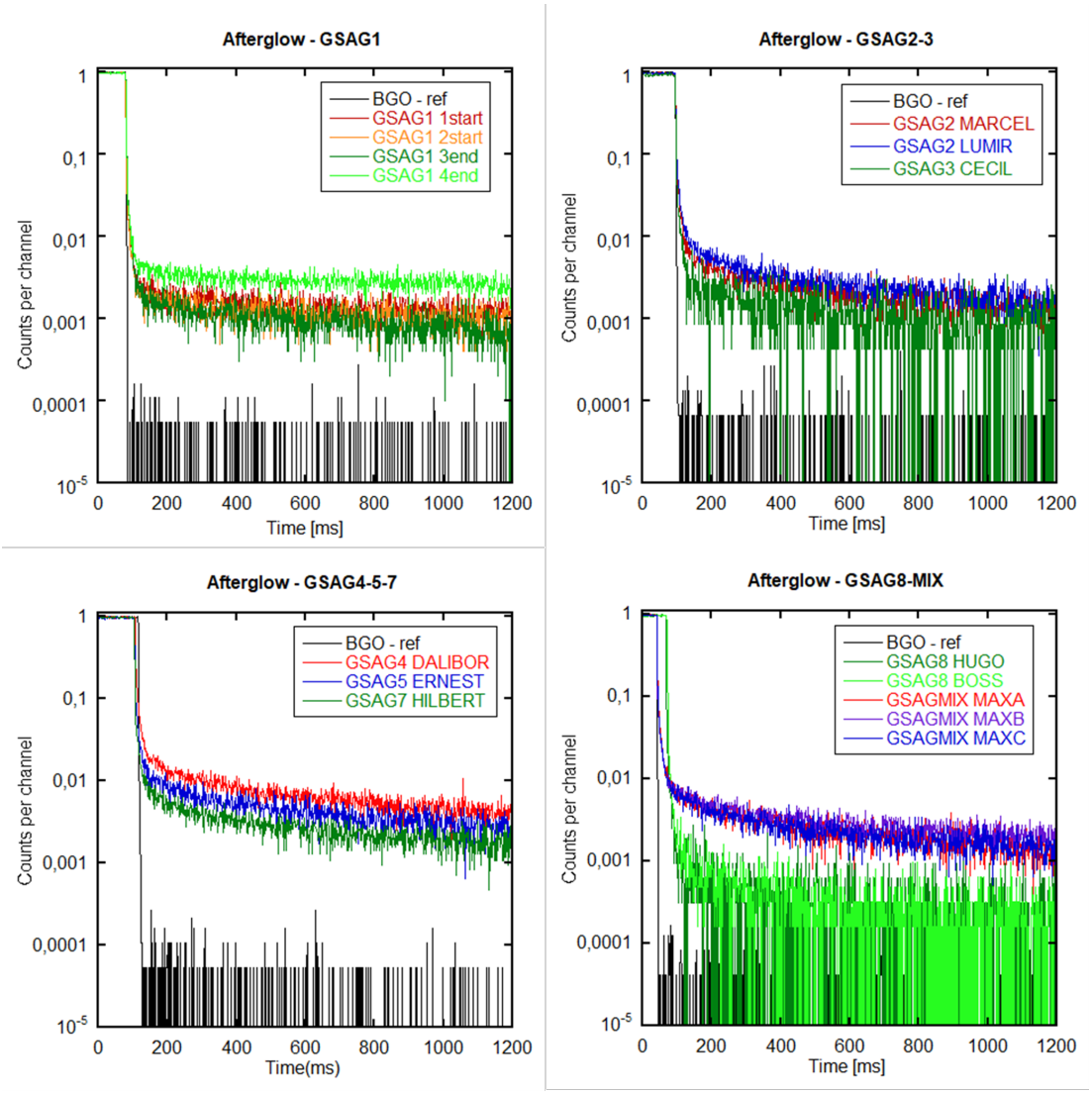


Figure 6.15 Afterglow of GSAG samples.

Sample	Scintillation decay				LY	Photoluminescence decay ex452						Integral LY
	1 [ns]	LS1 [%]	2 [ns]	LS2 [%]	[ph/keV]	1 [ns]	LS1 [%]	2 [ns]	LS2 [%]	3 [ns]	LS3 [%]	[%BGO]
1 start	6.2	40	153	60	**2.8**	36.6	82	105	18	—	—	39
2 start	2.9	31	94	69	**2.8**	36.6	83	110	17	—	—	34
3 end	6.5	28	175	72	**2.6**	36.1	82	111	18	—	—	34
4 end	3.2	59	117	41	**2.6**	36.7	82	111	18	—	—	32
LUMIR	11.9	26	136	74	**1.7**	34.1	82	106	18	—	—	23
MARCEL	2.6	28	99	72	**1.6**	34.5	82	102	18	—	—	28
CECIL	10.8	37	88	63	**1.5**	30.2	77	100	23	—	—	10
DALIBOR	—	—	—	—	—	33.1	71	89	29	—	—	22
ERNEST	2.8	16	94	84	—	32.6	73	96	27	—	—	16
HILBERT	29.5	51	109	49	**1.5**	35.5	86	123	14	—	—	34
HUGO	42.4	79	344	21	**1.6**	2.5	2	32	78	105	20	14
BOSS	50.4	65	326	35	**1.8**	5.2	2	33	80	108	18	20
MAXA	18.2	24	140	76	**1.5**	28.3	60	74	40	—	—	22
MAXB	10.3	16	112	84	**1.5**	26.7	53	69	47	—	—	23
MAXC	16.6	21	155	79	**1.6**	24.4	48	67	52	—	—	25

Sample	Photoluminescence decay ex339nm			
	1 [ns]	LS1 [%]	2 [ns]	LS2 [%]
1 start	35.2	70	92	30
2 start	37.6	89	118	11
3 end	34.3	67	85	33
4 end	40	74	94	26
LUMIR	30.4	57	74	43
MARCEL	31.4	60	77	40
CECIL	25.5	71	100	29

Table 6.4 Scintillation and photoluminescence decay time constants, light sums and light yield of GSAG samples.

cutoff, which is comparable to the results obtained by -PD method after annealing in air [94]. Other samples perform significantly worse, showing only a drop of two orders of magnitude of 100 ms after the X-ray cutoff, indicative of the presence of much slower components, mainly due to Fe^{3+} impurity.

6.3.2 Photoluminescence spectra

The photoluminescence excitation spectra in 6.16, measured at $\lambda_{em} = 550$ nm (560 nm for GSAG8), are dominated by Ce^{3+} $4f \rightarrow 5d^1$ (443 nm) and $4f \rightarrow 5d^2$ (341 nm) transitions, which are well aligned with absorption spectra (see 6.11). We can see that we get Ce^{3+} emission even for the excitation wavelengths of Gd^{3+}, due to the charge transfer from Gd^{3+} sublattice to the Ce^{3+} centers. These effects appear to be stronger in the GSAG7-8 and GSAGMIX samples.

Photoluminescence emission spectra were measured for both excitation wavelengths of Ce^{3+} (λ_{ex}= 340 nm and λ_{ex}= 460 nm) and are shown in Figures 6.17 and 6.18, respectively. All peaks have the same shape, when normalized, and the

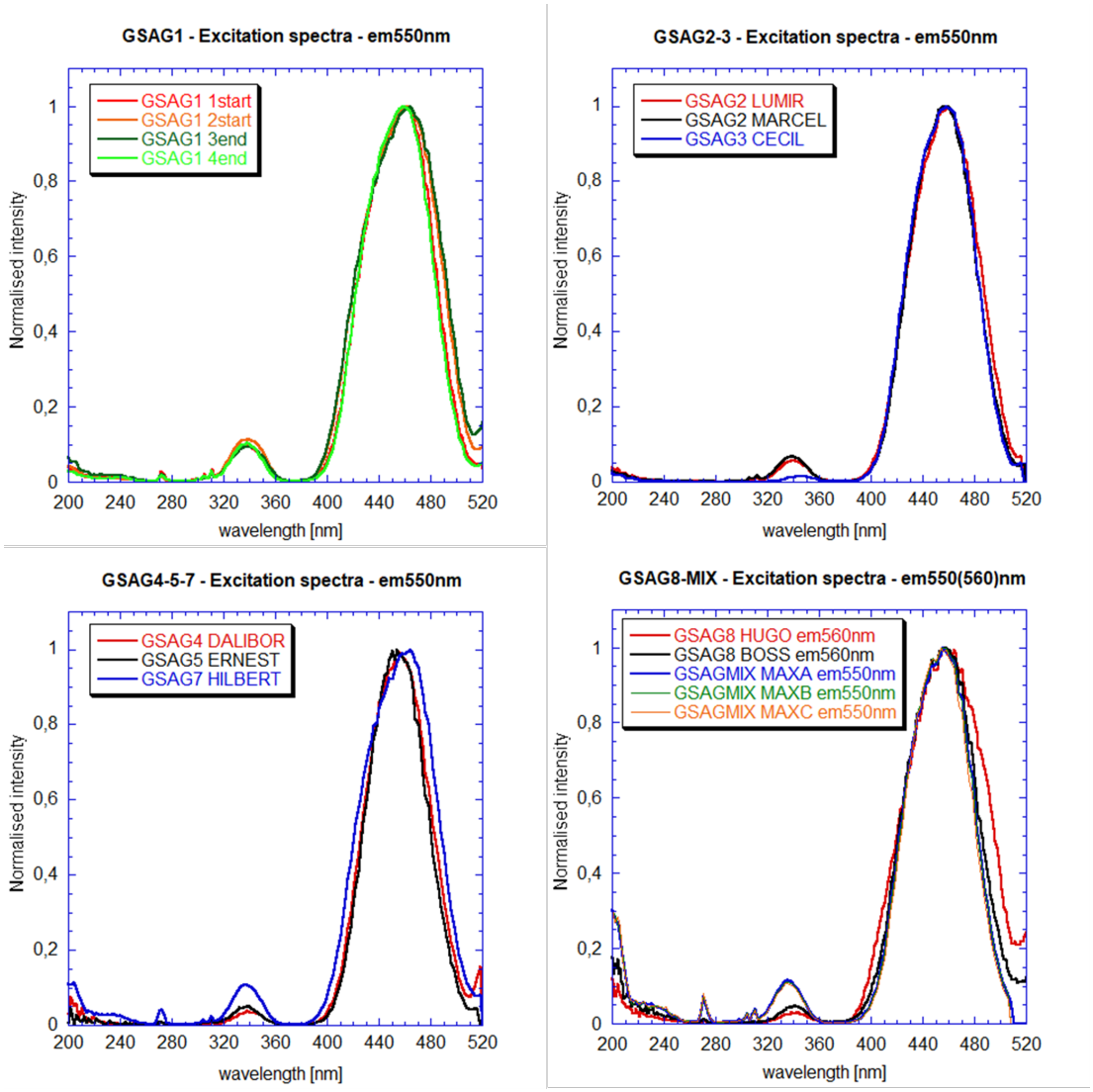


Figure 6.16 Photoluminescence excitation spectra for emission wavelength $\lambda_{em} = 550$ nm of GSAG samples.

intensity of the peak is related to the optical quality of the crystal and the level of Fe3+ impurity. It is evident that the samples exhhibiting lower intensity for excitation 460 nm are relatively even weaker at 340 nm. A decrease in intensity is observed for the GSAG3-5 and GSAG8 samples. For some samples, only emission spectra were measured at 460 nm excitation.

6.3.3 Photoluminescence decay

Figure 6.19 shows 3 examples of RT photoluminescence decay curve of the Ce^{3+} $4f \rightarrow 5d^1$ emission (ex=452nm, em=550nm) and Ce3+ 4f $\rightarrow$ 5d2 (λ_{ex}=339 nm, λ_{em}=550 nm) of GSAG samples. The decay times evaluated are shown in Table 6.4.

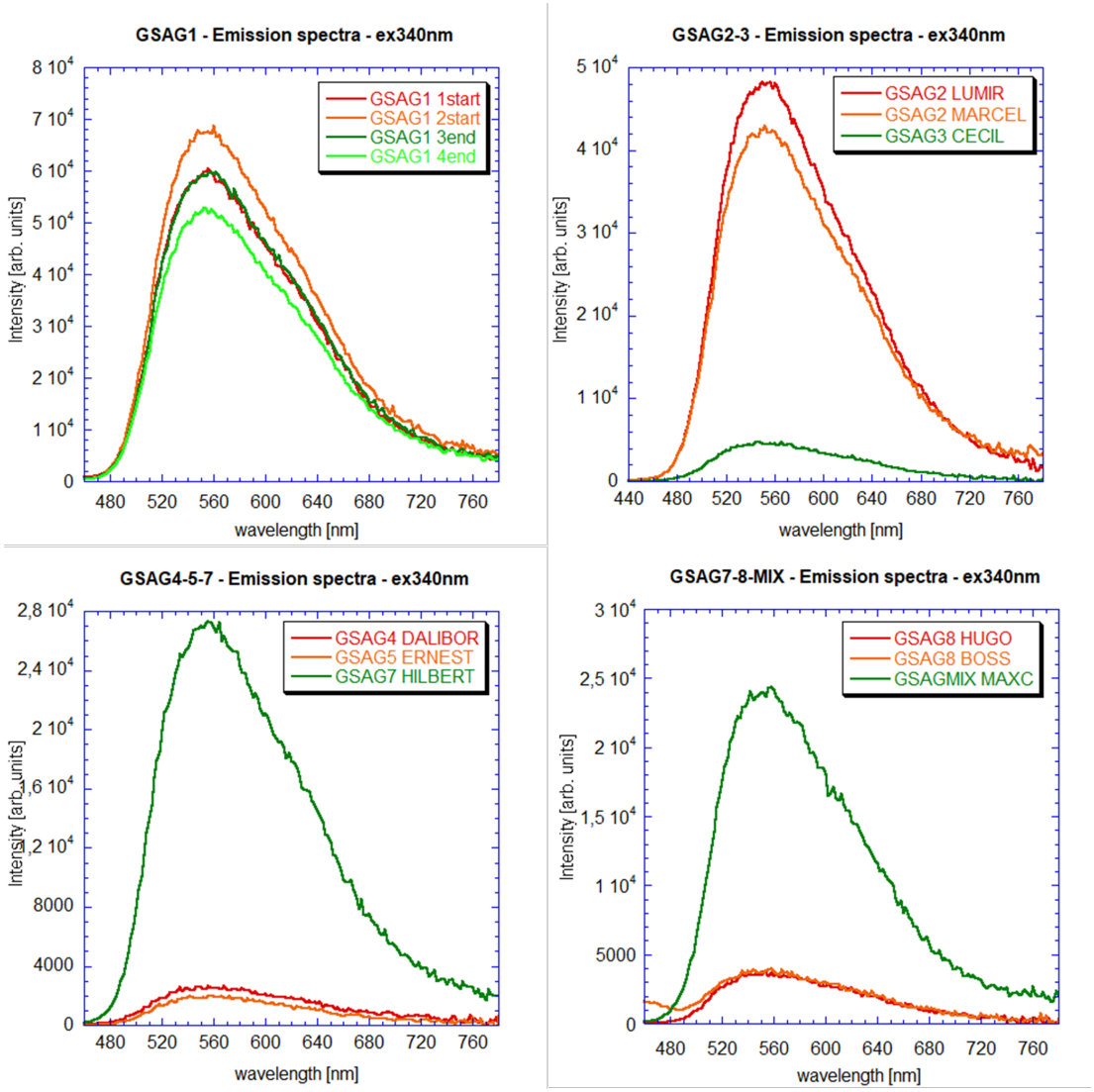


Figure 6.17 Photoluminescence emission spectra for excitation wavelength $\lambda_{ex} = 340$ nm of GSAG samples.

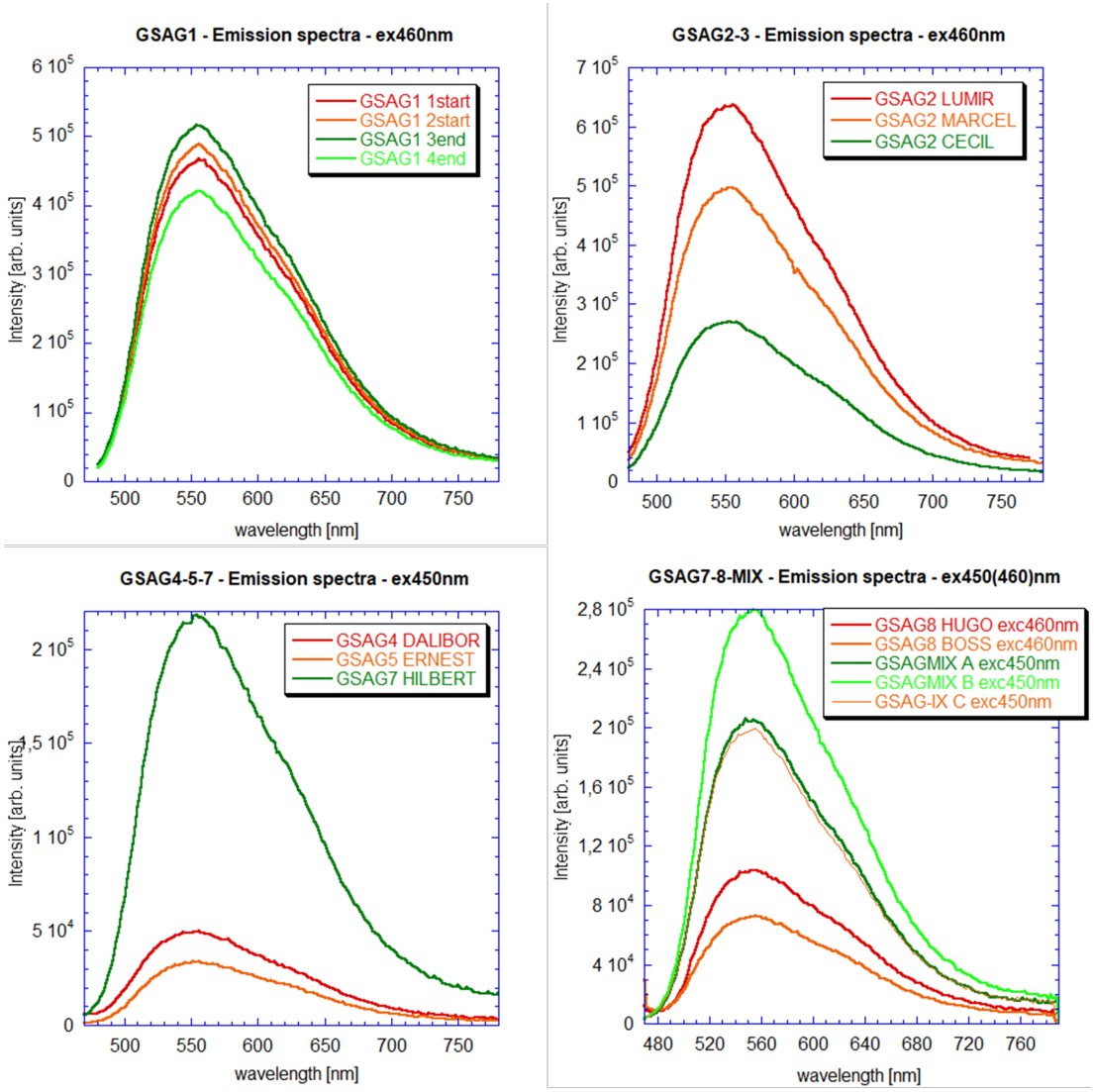


Figure 6.18 Photoluminescence emission spectra for excitation wavelength $\lambda_{ex} = 460$ nm of GSAG samples.

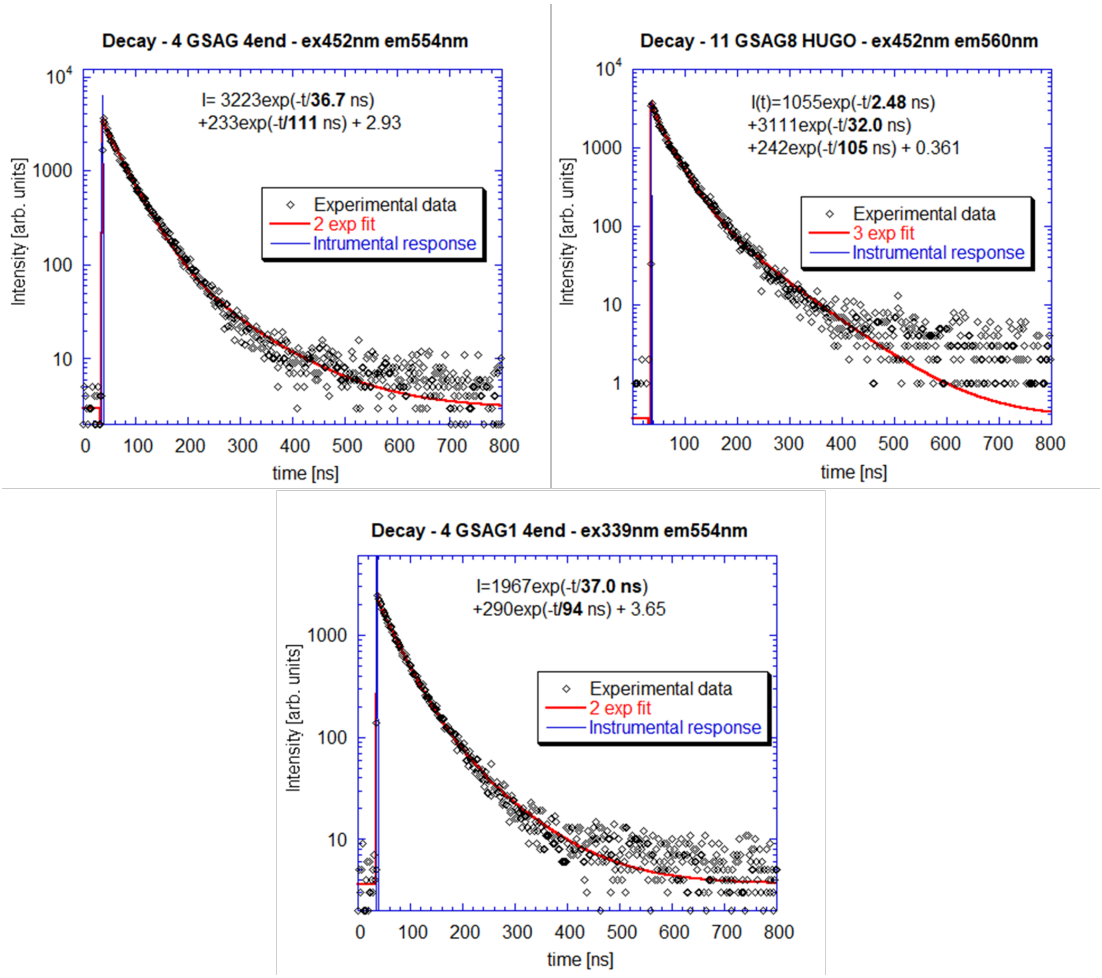


Figure 6.19 Photoluminescence decays of GSAG1 - 4 end and GSAG8 HUGO for excitation $\lambda_{ex} = 452$ nm and emission $\lambda_{ex} = 554$ nm and photoluminescence decay of GSAG1 - 4 end for excitation $\lambda_{ex} = 339$ nm and emission $\lambda_{ex} = 554$ nm.

7 Discussion

7.1 Quality of prepared crystals and comparation with literature

7.1.1 GGAG

The scintillation properties achieved by the GGAG:Ce single crystal can hardly be compared with the literature, because crystals studied of given composition have never been prepared by a floating zone method, with similar Al/Ga ratio and Ce dopant concentration. On top of that, to the best of our knowledge, our samples are the first one ever prepared by the laser-diode floating zone method. However, our samples overcame the scintillation response of samples prepared in halogen mirror furnace from papers [52, 23] in terms of the fast scintillation time component. Scintillation light yield could not be compared as it was not studied in the mentioned papers.

The samples in paper [38] are characterized by a scintillation time component (71 - 88 ns) similar to ours, but a higher light sum of the fast component has been achieved (80- 88% compared to ours 60%). Our material beats them in terms of scintillation light yield. We achieved a scintillation light yield as high as 42000 ph/MeV, which is 8000 ph/MeV more compared to grown samples and 3000 ph / MeV more compared to their samples after annealing in [38].

Compared with state-of-the-art GGAG-based scintillators grown by conventional methods [104, 105, 106], their effective scintillation decay times are within 60-140 ns and the scintillation light yield varies from 28000 to 50000 ph/MeV. It is safe to say that our samples are perfectly competitive with them in terms of simultaneous consideration of the scintillation speed and light yield.

7.1.2 GSAG

In the GSAG absorption spectra we can see smooth broad absorption below 340 nm, belonging to charge transfer absorption of Ce^{4+} [24, 98]. To support the latter ascription, we compared our GSAG:Ce absorption data with those of the sample from Zapadlík et al. [94] prepared in an iridium crucible under an atmosphere of N_2 (4N) (Fig. 2 in [94]). The difference is clearly visible in Figure 7.1 and its shape is shown in the difference spectrum in the inset. The difference spectrum is obtained by subtracting the absorption spectrum of the GSAG taken by Zapadlik et al. from the GSAG – start 2 one. Before subtraction, the reflection losses were subtracted from both curves, and the curve from [94] is normalized to the same value as the GSAG - start 2 at 451 nm. The enhancement of the absorption spectra below 350 nm and the difference spectrum in the inset of Figure 7.2 is closely similar to the CT absorption spectrum of Ce^{4+} reported in [62]. For GAGG:Ce,Mg garnet in [63] and LYSO:Ce,Mg(Ca) and LYSO:Ce,Mg(Ca) orthosilicate [64] the presence of Ce^{4+} is directly confirmed by XANES photoelectron spectroscopy and is clearly correlated with the changes described above in absorption spectra.

Furthermore, we annealed the sample GSAG - end 3 in the reduction atmosphere ($Ar + 5\%H_2$) for 9 h at 1200 °C, which should reduce Ce^{4+} to Ce^{3+}, and

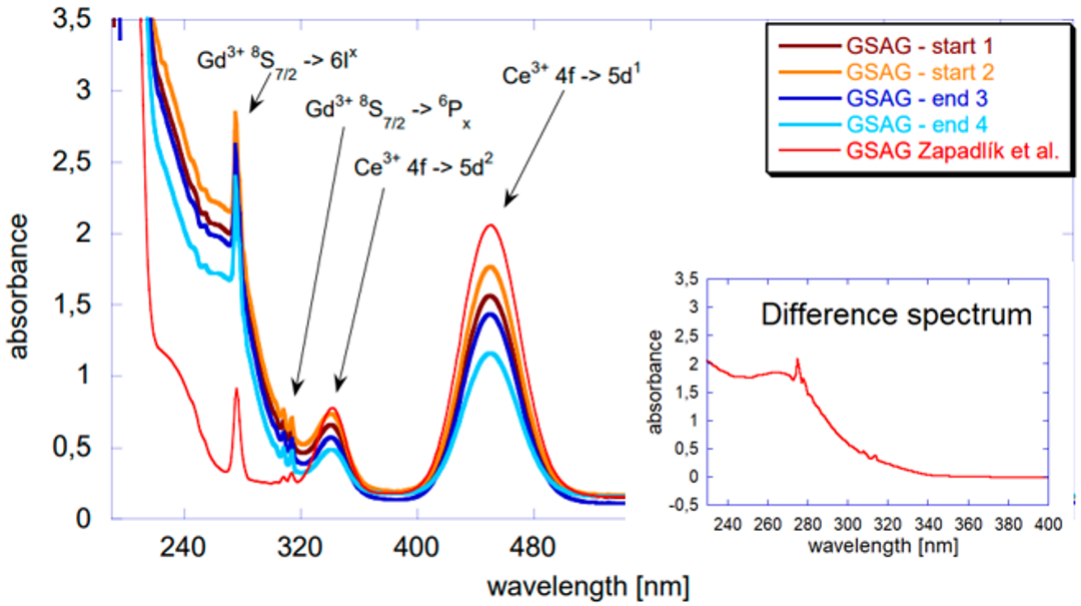


Figure 7.1 In the top graph there is RT absorption spectra of GSAG1 samples compared with GSAG sample from Zapadlík [94]. Difference spectrum obtained by subtracting the absorption spectra of GSAG taken by Zapadlík from the GSAG - start 2 one is in the inset

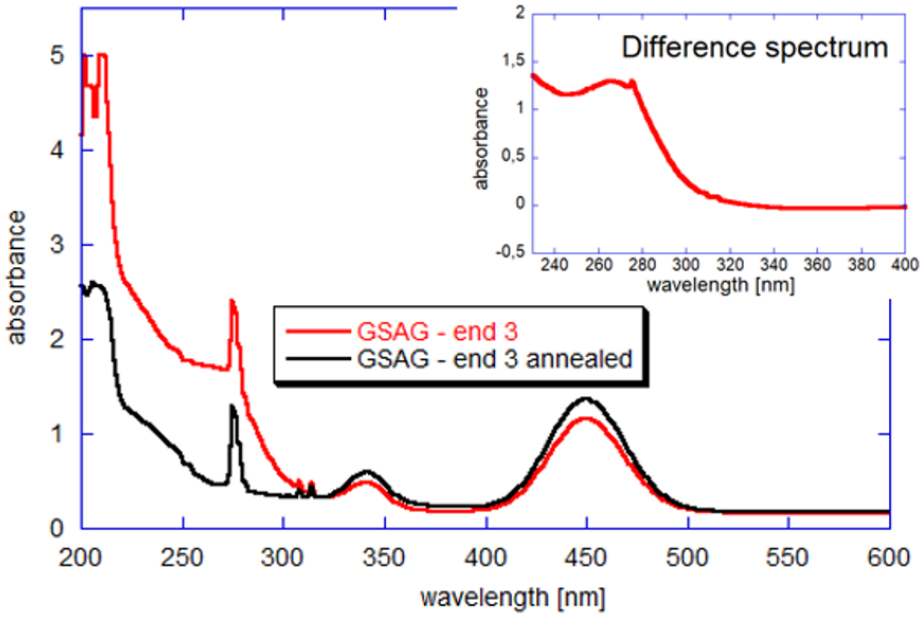


Figure 7.2 Comparison of absorption spectra of GSAG - end 3 before and after annealing. In the inset there is difference spectrum obtained by subtracting annealed spectra from unannealed.

measured the absorption spectrum, see 7.2. There is an apparent decrease in absorbance in the UV spectral region and the difference spectrum, constructed analogously to 7.1, shows a shape closely similar (inset of 7.2). This result provides further evidence that the enhanced absorbance in the UV spectra region in LFZ grown samples belongs to the charge transfer transition of Ce^{4+}, which is stabilized by the pressurized oxygen atmosphere in the growth process. Regarding the concentration Ce^{3+} measured by the amplitude of absorption $4f \rightarrow 5d^1$, it is within the variation 10% with the exception of the GSAG – end 4 sample where the origin of a somewhat larger decrease of the amplitude of the absorption bands $4f5d^{1,2}$ is not understood. An abrupt increase in absorbance below 220 nm can be attributed to the onset of host band-to-band transitions and is positioned similarly to GAGG [80].

All samples presented have a slow component in the scintillation decay (90-180 ns), which is significantly shorter than the dominant component (263 ns) measured in samples prepared by μ-PD method [94], where the even slower component of 1010 ns is present. However, the LY of our sample set (2600 – 2800 ph/MeV) is only about one-third of that of samples prepared by -PD method (8900 ph/MeV).

The use of an oxygen atmosphere results in the stabilization of Ce^{4+}, as evidenced by the related charge-transfer absorption transition in absorption spectra. Its presence visibly accelerates the scintillation decay in comparison with samples prepared by the μ-PD technique. Photoluminescence decays show partial ionization of the excited state $5d^1$ of Ce^3+, which might be one of the reasons for lower LY and slower tail due to delayed luminescence.

A very fast and weak component in scintillation decay is obtained in both measurement setups (with ps X-ray excitation comparatively less) and might also be a sign of some quenching that lowers LY. It might be related to the lower quality of the crystal itself, but its nature is unclear and needs further investigation.

7.2 Effect of afterheater in floating zone method

The passive afterheating system was used for the first time for the growth of Nd single crystals [96, 95], and we used a passive or active afterheater for all our growth processes. Consequently, we do not have a direct comparison of single crystals prepared with and without the afterheater.

However, the optical quality of our crystals was primarily affected by cracks. During the process of cutting samples from the single crystal, it was evident that most cracks were confined to the surface (less than 1 mm from the surface), allowing us to obtain crack-free samples. Our single crystals were not cloudy in volume, did not suffer from microcracks, nor did they exhibit a polycrystalline structure. These imperfections were commonly observed in the single crystals prepared by Yun Shi from the Shanghai Institute of Ceramics, Chinese Academy of Sciences, who presented a poster titled "Growth of Ce Scintillation Crystals with Characteristics of High Light Yield and Fast Decay by the Optical Floating Zone Method" at the SCINT2024 conference. In our best knowledge in the literature there are no other presented pictures of GGAG single crystals prepared by the floating zone method.

We conducted only a few growth runs with the active afterheater. The growth process was observed to be more stable and required fewer interventions from

the operator. Upon visual inspection, the single crystals grown with the active afterheater were similar to those grown with the passive afterheater. Unfortunately, we could not compare the quality of the crystals based on optical and scintillation measurements because all of the crystals were GSAG crystals with Fe impurities. The presence of Fe^{3+} excludes any meaningful comparison of the quality of the single crystals.

7.3 Iron contamination

During the growth of GGAG samples, we did not find any sign of contamination of our samples. However, the very first single crystal of GSAG prepared showed anomalous emission in radioluminescence spectra above 720 nm. In Figure 7.3 you can see the comparison of radioluminescence spectra between sample from single crystal prepared by the micro-pulling-down method in the Mo crucible, sample from single crystal prepared by the Czochralski method and sample GSAG1 1start. All single crystals were of the same composition - $Gd_{2.874}Ce_{0.006}Sc_{1.89}Al_{3.23}O_{12}$.

The first suspicion of the source of contamination was the agate mortar and pestle, which is shared between users in the MGML lab. All subsequent powder rod preparations were performed with brand new mortar that was not used for any other materials, but the contamination problem persisted. We further investigated and the origin of the emission was confirmed by measuring the radioluminescence spectra of single-crystal GSAG3 by a CCD camera detector, which showed the peak of emission at 800 nm. Subsequent measurement of photoluminescence decay spectra with excitation 266 nm and emission 760 nm (maximum for the detector) showed a single exponential decay with time constant of 6.532 ms, which confirms contamination by Fe^{3+} ions [102, 107], shown in Figure 7.4 .

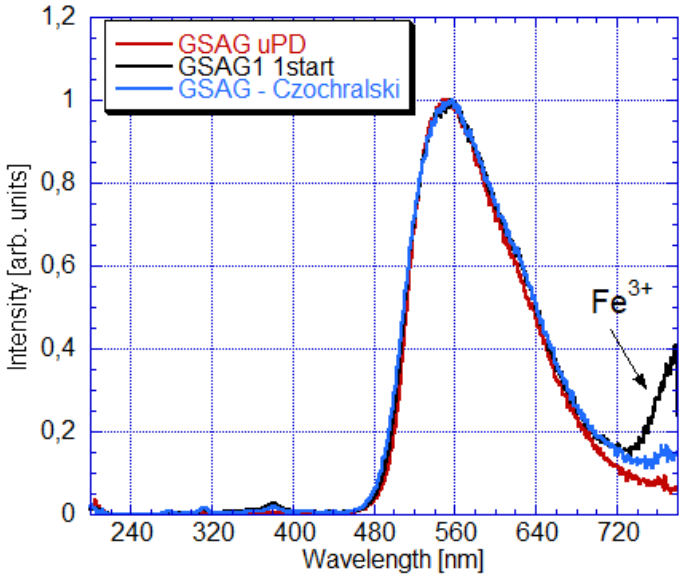


Figure 7.3 Comparison of radioluminescence spectra of GSAG prepared by floating-zone, micro-pulling-down and Czochralski methods.

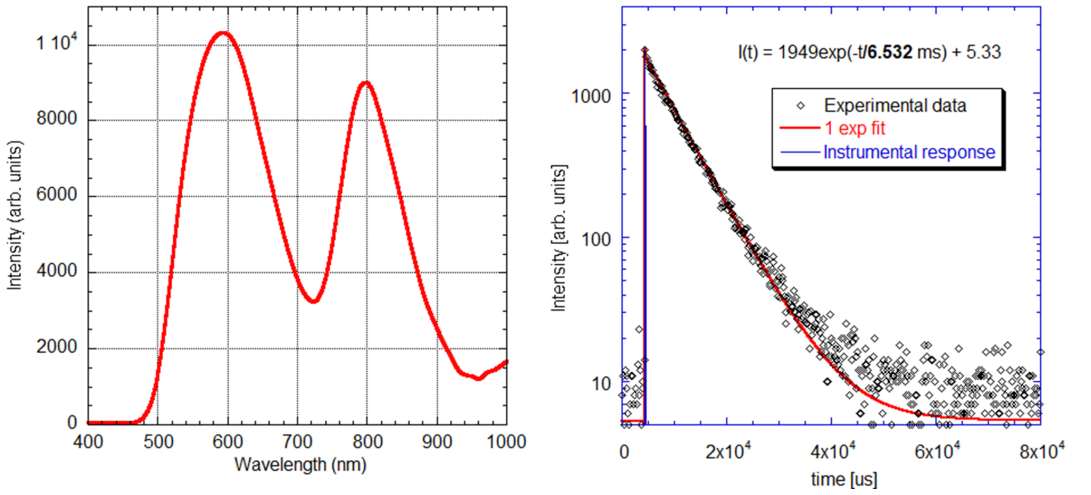


Figure 7.4 Radioluminescence spectra of GSAG3 single-crystal by CCD camera detector and measurement of photoluminescence decay with excitation at 266 nm and emission 760 nm showing 6.5 ms decay time typical for Fe^{3+} [102, 107]

The following measurement of the radioluminescence spectra for all powder precursors in 7.5 showed the infrared emission, which varied strongly in intensity between the precursors. The precursors 2,4 had very intensive emission, but in the 3 and 4 it was almost negligible. In single crystals prepared from the precursors (see above), the emission of Fe^{3+} 800 nm relative to the emission of Ce^{3+} 560 nm is even stronger.

These measurements showed that the source of contamination Fe^{3+} comes at least partially from the Institute of Physics. Futher investigation is needed to locate the precise source (primary ingredients, furnace, laboratory environment, etc.). An interesting question for the users of the floating zone furnace is how the contamination acts during the growth of a single crystal by the floating zone method according to the segregation coefficient of impurity. The growth in the Mo crucible was performed by micro-pulling down to answer these questions, but the results are not available just yet.

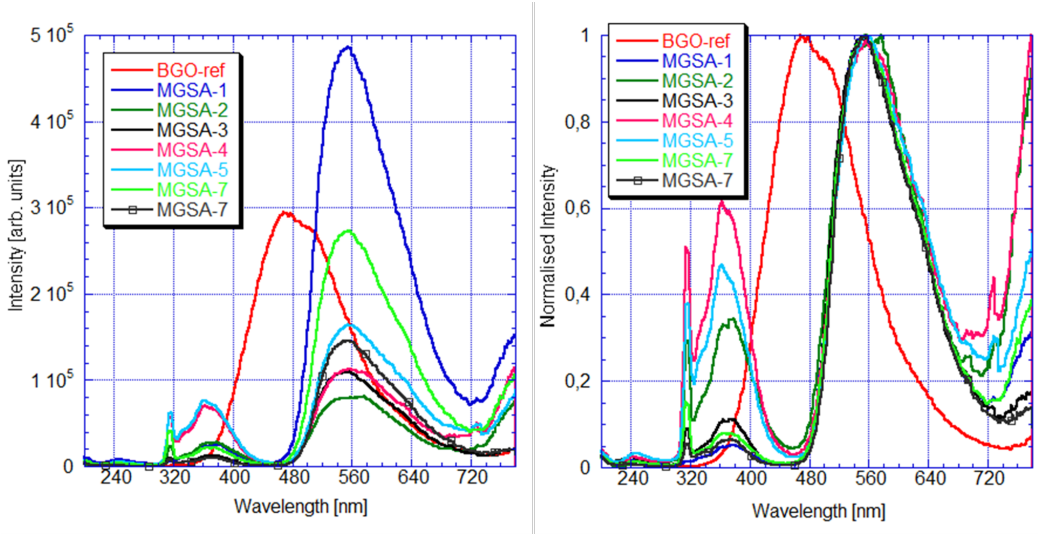


Figure 7.5 Radioluminescence spectra of GSAG precursors, absolute and normalised.

Conclusions

We enhanced the furnace in the MGML laboratory by incorporating both passive and active afterheaters, significantly reducing the temperature gradient, improving the achievable temperature of the hot zone, and consequently the quality of the crystals. The use of an afterheater in the floating zone method is unprecedented and addresses a major drawback of this method: the extremely high temperature gradient.

We successfully prepared two series of single crystals of GGAG and GSAG using the laser-diode floating zone method for the first time documented in literature. Despite the presence of numerous cracks, the optical quality of our single crystals was sufficient to conduct scintillation measurements.

Our crystals represent the highest optical quality among those prepared by the floating zone method, as documented in the literature with light yield of 42000 ph/MeV and scintillation decay 89.5ns(61%)+435nm(39%) for the GGAG:Ce and LY 38100 ph/MeV with scintillation decay 76ns(66%)+405nm(34%) fot GGAG:Ce,Mg. We had the opportunity to compare the optical quality of our samples with the latest work by Yun Shi from the Shanghai Institute of Ceramics, Chinese Academy of Sciences, who presented a poster titled *"Growth of Ce Scintillation Crystals with Characteristics of High Light Yield and Fast Decay by the Optical Floating Zone Method"* at the SCINT2024 conference. Our single crystals demonstrated superior quality, free from visible unwanted color centers.

The scintillation performance of our samples is fully comparable with the best results in the literature for crystals prepared by the floating zone method and is on par with those prepared by micro-pulling-down. We presented our work as a poster at the International Conference of Luminescence 2023 in Paris and intend to publish our results on GGAG later this year.

The growth of GSAG single crystals has presented particular challenges because of the formation of numerous bubbles. However, with the aid of the active afterheater, we achieved single crystals with good optical quality. Unfortunately, iron contamination adversely affected our work and the scintillation performance of the samples, resulting in a very low light yield despite and high afterglow.

We were able to publish the results of samples from the GSAG1 crystal [108] and presented them at the SCINT2024 Conference in Milan.

Our work convincingly demonstrates that the laser-diode floating zone method is a promising and potentially significant technique for the research and development of new scintillation materials (as well as laser materials, as shown in [95]). The principle of the floating zone method, particularly the surface heating of the hot zone, makes it well suited for the preparation of small samples for research purposes. However, it is not feasible for industrial-scale growth of single crystals.

Bibliography

1. Jarý, V.; Pejchal, J. *Scintilační materiály*. Academia, 2023.
2. Harvey, E. Newton. A history of luminescence from the earliest times until 1900. *Memoirs of the American Philosophical Society, v. 44*. 1957.
3. Vavilov, Sergej Ivanovich. *The Human Eye and the Sun: Hot and Cold Light*. Elsevier, 2016.
4. Kittel, C.; McEuen, P. *Introduction to solid state physics*. John Wiley & Sons, 2018.
5. Blasse, George; Grabmaier, BC; Blasse, G; Grabmaier, BC. *A general introduction to luminescent materials*. Springer, 1994.
6. Alekhin, Mikhail S; Biner, Daniel A; Krämer, Karl W; Dorenbos, Pieter. Improvement of LaBr3: 5% Ce scintillation properties by Li+, Na+, Mg2+, Ca2+, Sr2+, and Ba2+ co-doping. *Journal of Applied Physics*. 2013, vol. 113, no. 22. Available from DOI: 10.1063/1.4810848.
7. Kamada, Kei; Nikl, Martin; Kurosawa, Shunsuke; Beitlerova, Alena; Nagura, Aya; Shoji, Yasuhiro; Pejchal, Jan; Ohashi, Yuji; Yokota, Yuui; Yoshikawa, Akira. Alkali earth co-doping effects on luminescence and scintillation properties of Ce doped $Gd_3Al_2Ga_3O_{12}$ scintillator. *Optical Materials*. 2015, vol. 41, pp. 63–66. Available from DOI: 10.1016/j.optmat.2014.10.008.
8. Nagura, Aya; Kamada, Kei; Nikl, Martin; Kurosawa, Shunsuke; Pejchal, Jan; Yokota, Yuui; Ohashi, Yuji; Yoshikawa, Akira. Improvement of scintillation properties on Ce doped $Y_3Al_5O_{12}$ scintillator by divalent cations co-doping. *Japanese Journal of Applied Physics*. 2015, vol. 54, no. 4S, 04DH17. Available from DOI: 10.7567/JJAP.54.04DH17.
9. Tamulatis, G.; Dosovitskiy, G.; Gola, A.; Korjik, M.; Mazzi, A.; Nargelas, S.; Sokolov, P.; Vaitkevičius, A. Improvement of response time in GAGG:Ce scintillation crystals by magnesium codoping. *Journal of Applied Physics*. 2018, vol. 124, no. 21, p. 215907. Available from DOI: 10.1063/1.5064434.
10. Nikl, Martin; Yoshikawa, Akira. Recent R&D Trends in Inorganic Single-Crystal Scintillator Materials for Radiation Detection. *Advanced Optical Materials*. 2015, vol. 3, no. 4, pp. 463–481. Available from DOI: 10.1002/adom.201400571.
11. Dujardin, C.; Auffray, E.; Bourret-Courchesne, E.; Dorenbos, P.; Lecoq, P.; Nikl, M.; Vasil'ev, A. N.; Yoshikawa, A.; Zhu, R.-Y. Needs, Trends, and Advances in Inorganic Scintillators. *IEEE Transactions on Nuclear Science*. 2018, vol. 65, no. 8, pp. 1977–1997. Available from DOI: 10.1109/TNS.2018.2840160.
12. M., Nikl. Scintillation detectors for x-rays. *Measurement Science and Technology*. 2006, vol. 17, no. 4, R37. Available from DOI: 10.1088/0957-0233/17/4/R01.

13. Varney, Chris R.; Selim, Farida A. Color centers in YAG. *AIMS Materials Science*. 2015, vol. 2, no. 4, pp. 560–572. Available from DOI: 10.3934/matersci.2015.4.560.

14. Tomaszewski, Paweł E. Jan Czochralski—father of the Czochralski method. *Journal of Crystal Growth*. 2002, vol. 236, no. 1, pp. 1–4. Available from DOI: 10.1016/S0022-0248(01)02195-9.

15. Yoshikawa, A; Chani, V; Nikl, M. Czochralski growth and properties of scintillating crystals. *Acta physica polonica A*. 2013, vol. 124, no. 2, pp. 250–264. Available from DOI: 10.12693/APhysPolA.124.250.

16. Zhao, Wenhan; Li, Jiancheng; Liu, Lijun. Control of Oxygen Impurities in a Continuous-Feeding Czochralski-Silicon Crystal Growth by the Double-Crucible Method. *Crystals*. 2021, vol. 11, no. 3, p. 264. Available from DOI: 10.3390/cryst11030264.

17. Friedrich, J. Methods for Bulk Growth of Inorganic Crystals: Crystal Growth. In: *Reference Module in Materials Science and Materials Engineering*. Elsevier, 2016. Available from DOI: 10.1016/B978-0-12-803581-8.01010-9.

18. Crytur s.r.o. *YAG:Ce* [online]. 2024. Available also from: www.crytur.cz/materials/yagce/. Accessed 14.7.2024.

19. Crytur s.r.o. *GGAG+* [online]. 2024. Available also from: www.crytur.cz/materials/ggag/. Accessed 14.7.2024.

20. Crytur s.r.o. *LuAG:Pr* [online]. 2024. Available also from: www.crytur.cz/materials/luag-pr/. Accessed 14.7.2024.

21. Laguta, V.; Buryi, M.; Arhipov, P.; Sidletskiy, O.; Laguta, O.; Brik, M. G.; Nikl, M. Oxygen-vacancy donor-electron center in $Y_3Al_5O_{12}$ garnet crystals: Electron paramagnetic resonance and dielectric spectroscopy study. *Phys. Rev. B*. 2020, vol. 101, p. 024106. Available from DOI: 10.1103/PhysRevB.101.024106.

22. Lamoreaux, RH; Hildenbrand, DL; Brewer, L. High-Temperature Vaporization Behavior of Oxides II. Oxides of Be, Mg, Ca, Sr, Ba, B, Al, Ga, In, Tl, Si, Ge, Sn, Pb, Zn, Cd, and Hg. *Journal of physical and chemical reference data*. 1987, vol. 16, no. 3, pp. 419–443. Available from DOI: 10.1063/1.555799.

23. Yoshikawa, Akira; Fujimoto, Yutaka; Yamaji, Akihiro; Kurosawa, Shunsuke; Pejchal, Jan; Sugiyama, Makoto; Wakahara, Shingo; Futami, Yoshisuke; Yokota, Yuui; Kamada, Kei; Yubuta, Kunio; Shishido, Toetsu; Nikl, Martin. Crystal growth and characterization of $Ce : Gd_3(Ga, Al)_5O_{12}$ single crystal using floating zone method in different O_2 partial pressure. *Optical Materials*. 2013, vol. 35, no. 11, pp. 1882–1886. Available from DOI: 10.1016/j.optmat.2013.02.021.

24. Bartosiewicz, Karol; Markovskyi, Anton; Horiai, Takahiko; Szymański, Damian; Kurosawa, Shunsuke; Yamaji, Akihiro; Yoshikawa, Akira; Zorenko, Yuriy. A study of Mg^{2+} ions effect on atoms segregation, defects formation, luminescence and scintillation properties in Ce^{3+} doped $Gd_3Al_2Ga_3O_{12}$ single crystals. *Journal of Alloys and Compounds*. 2022, vol. 905, p. 164154. Available from DOI: 10.1016/j.jallcom.2022.164154.

25. Martinazzoli, Loris; Nargelas, Saulius; Boháček, Pavel; Calá, Roberto; Dušek, Michal; Rohlíček, Jan; Tamulaitis, Gintautas; Auffray, Etiennette; Nikl, Martin. Compositional engineering of multicomponent garnet scintillators: towards an ultra-accelerated scintillation response. *Mater. Adv.* 2022, vol. 3, pp. 6842–6852. Available from DOI: 10.1039/D2MA00626J.

26. Miyazawa, Shintaro. Shaped Melt Lowering (SML): A novel growth technique permitting $k_{eff} = 1$. *Journal of Crystal Growth*. 1982, vol. 60, no. 2, pp. 331–337. Available from DOI: 10.1016/0022-0248(82)90107-5.

27. Yoon, Dae-Ho; Fukuda, Tsuguo. Characterization of $LiNbO_3$ micro single crystals grown by the micro-pulling-down method. *Journal of Crystal Growth*. 1994, vol. 144, no. 3, pp. 201–206. ISSN 0022-0248. Available from DOI: 10.1016/0022-0248(94)90456-1.

28. Klimm, Detlef; Acosta, Maria F.; Santos, Ivanildo A. dos; Ranieri, Izilda M.; Ganschow, Steffen; Merino, Rosa I. Growth of Self Organized Eutectic Fibers from LiF Rare Earth Fluoride Systems. *MRS Proceedings*. 2013, vol. 1508, p. 401. Available from DOI: 10.1557/opl.2013.487.

29. Yoshikawa, Akira; Nikl, Martin; Boulon, Georges; Fukuda, Tsuguo. Challenge and study for developing of novel single crystalline optical materials using micro-pulling-down method. *Optical Materials*. 2007, vol. 30, no. 1, pp. 6–10. Available from DOI: https://doi.org/10.1016/j.optmat.2006.10.030.

30. Sidletskiy, O.; Arhipov, P.; Tkachenko, S.; Gerasymov, Ia.; Kurtsev, D.; Jarý, V.; Kučerková, R.; Nikl, M.; Lebbou, K.; Auffray, E. Garnet Crystal Growth in Non-precious Metal Crucibles. In: Korzhik, Mikhail; Gektin, Alexander (eds.). *Engineering of Scintillation Materials and Radiation Technologies*. Cham: Springer International Publishing, 2019, pp. 83–95. ISBN 978-3-030-21970-3.

31. Zharikov, Evgeny V. Problems and recent advances in melt crystal growth technology. *Journal of Crystal Growth*. 2012, vol. 360, pp. 146–154. Available from DOI: 10.1016/j.jcrysgro.2011.11.049.

32. Shepherd, John A.; Gruner, Sol M.; Tate, Mark W.; Tecotzky, Melvin. Study of afterglow in x-ray phosphors for use on fast-framing charge-coupled device detectors. *Optical Engineering*. 1997, vol. 36, no. 11, pp. 3212–3222. Available from DOI: 10.1117/1.601530.

33. Revcolevschi, A.; Jegoudez, J. Growth of large high-T_c single crystals by the floating zone method: A review. *Progress in Materials Science*. 1997, vol. 42, no. 1, pp. 321–339. Available from DOI: 10.1016/S0079-6425(97)00022-4.

34. Kimura, Shigeyuki; Kitamura, Kenji. Floating Zone Crystal Growth and Phase Equilibria: A Review. *Journal of the American Ceramic Society*. 1992, vol. 75, no. 6, pp. 1440–1446. Available from DOI: 10.1111/j.1151-2916.1992.tb04207.x.

35. Kimura, S.; Kitamura, K.; Shindo, I. Growth of rare earth garnet crystals by the floating zone method. *Journal of Crystal Growth*. 1983, vol. 65, no. 1, pp. 543–548. Available from DOI: 10.1016/0022-0248(83)90100-8.

36. Kimura, S.; Shindo, I. Single crystal growth of YIG by the floating zone method. *Journal of Crystal Growth*. 1977, vol. 41, no. 2, pp. 192–198. Available from DOI: 10.1016/0022-0248(77)90045-8.

37. Kimura, S.; Shindo, I.; Kitamura, K.; Mori, Y.; Takamizawa, H. Evaluation of yttrium iron garnet single crystals grown by the floating zone method. *Journal of Crystal Growth*. 1978, vol. 44, no. 5, pp. 621–624. Available from DOI: 10.1016/0022-0248(78)90310-X.

38. Wu, Tong; Wang, Ling; Shi, Yun; Xu, Tianzhao; Wang, Hui; Fang, Jinghong; Ni, Jinqi; He, Huan; Wang, Chaoyue; Wan, Bo; Ding, Dongzhou; Zhou, Zhenzhen; Liu, Qian; Li, Qin; Yu, Jianding; Huang, Xintang; Shichalin, Oleg.; Papynov, E. K. Fast $(Ce, Gd)_3Ga_2Al_3O_{12}$ Scintillators Grown by the Optical Floating Zone Method. *Crystal Growth & Design*. 2022, vol. 22, no. 1, pp. 180–190. Available from DOI: 10.1021/acs.cgd.1c00779.

39. Tolksdorf, W. Growth of yttrium iron garnet single crystals. *Journal of Crystal Growth*. 1968, vol. 3-4, pp. 463–466. Available from DOI: 10.1016/0022-0248(68)90201-7.

40. Vlášková, K.; Colman, R. H.; Proschek, P.; Čapek, J.; Klicpera, M. Evidence for spin-glass ground state in fluorite-defect $Er_2Zr_2O_7$ single crystals. *Phys. Rev. B*. 2019, vol. 100, p. 214405. Available from DOI: 10.1103/PhysRevB.100.214405.

41. Kawata, Masanobu; Toshima, Hiroaki; Miyazawa, Yasuto; Morita, Shoji. Growth of gadolinium indium gallium garnet (GInGG) single crystal by the floating zone method. *Journal of Crystal Growth*. 1993, vol. 128, no. 1, Part 2, pp. 1011–1015. Available from DOI: 10.1016/S0022-0248(07)80088-1. Crystal Growth 1992.

42. Erdei, S.; Ainger, F.W. Crystal growth of YVO_4 using the LHPG technique. *Journal of Crystal Growth*. 1993, vol. 128, no. 1, Part 2, pp. 1025–1030. Available from DOI: 10.1016/S0022-0248(07)80091-1. Crystal Growth 1992.

43. Rey-García, Francisco; Ibáñez, Rafael; Angurel, Luis Alberto; Costa, Florinda M.; Fuente, Germán F. de la. Laser Floating Zone Growth: Overview, Singular Materials, Broad Applications, and Future Perspectives. *Crystals*. 2021, vol. 11, no. 1. Available from DOI: 10.3390/cryst11010038.

44. Ito, Toshimitsu; Ushiyama, Tomoharu; Yanagisawa, Yuji; Tomioka, Yasuhide; Shindo, Isamu; Yanase, Atsushi. Laser-diode-heated floating zone (LDFZ) method appropriate to crystal growth of incongruently melting materials. *Journal of Crystal Growth*. 2013, vol. 363, pp. 264–269. Available from DOI: 10.1016/j.jcrysgro.2012.10.059.

45. Stone, J.; Burrus, C. A.; Dentai, A. G.; Miller, B. I. Nd:YAG single-crystal fiber laser: Room-temperature cw operation using a single LED as an end pump. *Applied Physics Letters*. 1976, vol. 29, no. 1, pp. 37–39. Available from DOI: 10.1063/1.88863.

46. Fejer, MM; Nightingale, JL; Magel, GA; Byer, RL. Laser-heated miniature pedestal growth apparatus for single-crystal optical fibers. *Review of scientific instruments*. 1984, vol. 55, no. 11, pp. 1791–1796. Available from DOI: 10.1063/1.1137661.

47. Rudolph, P; Fukuda, T. Fiber crystal growth from the melt. *Crystal Research and Technology: Journal of Experimental and Industrial Crystallography*. 1999, vol. 34, no. 1, pp. 3–40. Available from DOI: 10.1007/978-3-662-07214-1.

48. Maxwell, Gisele; Ponting, Bennett; Gebremichael, Eminet; Magana, Ruben. Advances in single-crystal fibers and thin rods grown by laser heated pedestal growth. *Crystals*. 2017, vol. 7, no. 1, p. 12. Available from DOI: 10.3390/cryst7010012.

49. Nie, Craig D; Bera, Subhabrata; Melzer, Jeffrey E; Harrington, James A; Dreyer, Elizabeth FC; Rand, Stephen C; Trembath-Reichert, Stephen; Hoef, Christopher D. Erbium distribution in single crystal YAG fibers grown by laser-heated pedestal growth technique. In: *Solid State Lasers XXIV: Technology and Devices*. SPIE, 2015, vol. 9342, pp. 11–16. Available from DOI: 10.1117/12.2083588.

50. Shen, Yonghang; Chen, Shuying; Zhao, Weizhong; Chen, Jun. Composite Cr^{4+}: YAG–Nd^{3+}: YAG crystal fiber: growth characteristics and passively Q-switched laser operation. In: *Materials, Devices, and Systems for Display and Lighting*. SPIE, 2002, vol. 4918, pp. 20–29. Available from DOI: 10.1117/12.483048.

51. Rey-García, F.; Sedrine, N. Ben; Fernandes, A.J.S.; Monteiro, T.; Costa, F.M. Shifting Lu_2SiO_5 crystal to eutectic structure by laser floating zone. *Journal of the European Ceramic Society*. 2018, vol. 38, no. 4, pp. 2059–2067. Available from DOI: 10.1016/j.jeurceramsoc.2017.11.003.

52. Suzuki, Akira; Kurosawa, Shunsuke; Pejchal, Jan; Babin, Vladimir; Fujimoto, Yutaka; Yamaji, Akihiro; Seki, Mafuyu; Futami, Yoshisuke; Yokota, Yuui; Yubuta, Kunio; Shishido, Toetsu; Kikuchi, Masae; Nikl, Martin; Yoshikawa, Akira. The effect of different oxidative growth conditions on the scintillation properties of $Ce : Gd_3Al_3Ga_2O_{12}$ crystal. *physica status solidi c*. 2012, vol. 9, no. 12, pp. 2251–2254. Available from DOI: 10.1002/pssc.201200327.

53. Schäfers, K.P.; Bolwin, K.; Büther, F.; Hermann, S.; Jacobs, A.H.; Kösters, T.; Kuhlmann, M.; Schäfers, M.; Viel, T. 1.10 - High-Resolution Small Animal Imaging. In: Brahme, Anders (ed.). *Comprehensive Biomedical Physics*. Oxford: Elsevier, 2014, pp. 181–211. ISBN 978-0-444-53633-4. Available from DOI: 10.1016/B978-0-444-53632-7.00110-6.

54. Dorenbos, Pieter. Fundamental Limitations in the Performance of Ce^{3+}–, Pr^{3+}–, and Eu^{2+} –Activated Scintillators. *IEEE Transactions on Nuclear Science*. 2010, vol. 57, no. 3, pp. 1162–1167. Available from DOI: 10.1109/TNS.2009.2031140.

55. Hofstadter, Robert. Alkali halide scintillation counters. *Physical Review*. 1948, vol. 74, no. 1, p. 100. Available from DOI: 10.1103/PhysRev.74.100.

56. Nikl, M.; Yoshikawa, A.; Kamada, K.; Nejezchleb, K.; Stanek, C.R.; Mares, J.A.; Blazek, K. Development of LuAG-based scintillator crystals – A review. *Progress in Crystal Growth and Characterization of Materials*. 2013, vol. 59, no. 2, pp. 47–72. Available from DOI: 10.1016/j.pcrysgrow.2013.02.001.

57. Weber, Marvin J; Monchamp, Roch R. Luminescence of $Bi_4Ge_3O_{12}$: Spectral and decay properties. *Journal of Applied Physics*. 1973, vol. 44, no. 12, pp. 5495–5499. Available from DOI: 10.1063/1.1662183.

58. Geller, Seymour. Crystal chemistry of the garnets. *Zeitschrift für Kristallographie-Crystalline Materials*. 1967, vol. 125, no. 1-6, pp. 1–47.

59. Grew, Edward S; Locock, Andrew J; Mills, Stuart J; Galuskina, Irina O; Galuskin, Evgeny V; Hålenius, Ulf. Nomenclature of the garnet supergroup. *American Mineralogist*. 2013, vol. 98, no. 4, pp. 785–811. Available from DOI: 10.2138/am.2013.4201.

60. Kamada, Kei; Endo, Takanori; Tsutumi, Kousuke; Yanagida, Takayuki; Fujimoto, Yutaka; Fukabori, Akihiro; Yoshikawa, Akira; Pejchal, Jan; Nikl, Martin. Composition engineering in cerium-doped $(Lu,Gd)_3(Ga,Al)_5O_{12}$ single-crystal scintillators. *Crystal Growth & Design*. 2011, vol. 11, no. 10, pp. 4484–4490. Available from DOI: 10.1021/cg200694a.

61. Nikl, Martin; Kamada, Kei; Babin, Vladimir; Pejchal, Jan; Pilarova, Katerina; Mihokova, Eva; Beitlerova, Alena; Bartosiewicz, Karol; Kurosawa, Shunsuke; Yoshikawa, Akira. Defect engineering in Ce-doped aluminum garnet single crystal scintillators. *Crystal Growth & Design*. 2014, vol. 14, no. 9, pp. 4827–4833. Available from DOI: 10.1021/cg501005s.

62. Brylew, Kamil; Drozdowski, Winicjusz; Wojtowicz, Andrzej J; Kamada, Kei; Yoshikawa, Akira. Studies of low temperature thermoluminescence of GAGG: Ce and LuAG: Pr scintillator crystals using the Tmax–Tstop method. *Journal of luminescence*. 2014, vol. 154, pp. 452–457. Available from DOI: j.jlumin.2014.05.035.

63. Dorenbos, Pieter. Electronic structure and optical properties of the lanthanide activated $RE_3(Al_{1-x}Ga_x)_5O_{12}$ (RE = Gd, Y, Lu) garnet compounds. *Journal of Luminescence*. 2013, vol. 134, pp. 310–318. Available from DOI: 10.1016/j.jlumin.2012.08.028.

64. Kitaura, Mamoru; Zen, Heishun; Kamada, Kei; Kurosawa, Shunsuke; Watanabe, Shinta; Ohnishi, Akimasa; Hara, Kazuhiko. Visualizing hidden electron trap levels in $Gd_3Al_2Ga_3O_{12}$: Ce crystals using a mid-infrared free-electron laser. *Applied Physics Letters*. 2018, vol. 112, no. 3, p. 031112. Available from DOI: 10.1063/1.5008632.

65. Kochurikhin, Vladimir; Kamada, Kei; Jin Kim, Kyoung; Ivanov, Mikhail; Gushchina, Liudmila; Shoji, Yasuhiro; Yoshino, Masao; Yoshikawa, Akira. Czochralski growth of 4-inch diameter $Ce : Gd_3Al_2Ga_3O_{12}$ single crystals for scintillator applications. *Journal of Crystal Growth*. 2020, vol. 531, p. 125384. Available from DOI: 10.1016/j.jcrysgro.2019.125384.

66. Laguta, Valentin; Zorenko, Yuriy; Gorbenko, Vitaliy; Iskaliyeva, Ayzhan; Zagorodniy, Yuriy; Sidletskiy, Oleg; Bilski, Paweł; Twardak, Anna; Nikl, Martin. Aluminum and Gallium Substitution in Yttrium and Lutetium Aluminum–Gallium Garnets: Investigation by Single-Crystal NMR and TSL Methods. *The Journal of Physical Chemistry C*. 2016, vol. 120, no. 42, pp. 24400–24408. Available from DOI: 10.1021/acs.jpcc.6b08593.

67. Li, Mingqing; Meng, Meng; Chen, Jie; Sun, Yiyang; Cheng, Guofeng; Chen, Lu; Zhao, Shuwen; Wan, Bo; Feng, He; Ren, Guohao; Ding, Dongzhou. Abnormal Site Preference of Al and Ga in $Gd_3Al_{2.3}Ga_{2.7}O_{12} : Ce$ Crystals. *physica status solidi (b)*. 2021, vol. 258, no. 8, p. 2000603. Available from DOI: 10.1002/pssb.202000603.

68. Nargelas, S; Talochka, Y; Vaitkevičius, A; Dosovitskiy, G; Buzanov, O; Vasil'ev, A; Malinauskas, T; Korzhik, M; Tamulaitis, G. Influence of matrix composition and its fluctuations on excitation relaxation and emission spectrum of Ce ions in $(Gd_xY_{1-x})_3Al_2Ga_3O_{12} : Ce$ scintillators. *Journal of Luminescence*. 2022, vol. 242, p. 118590. Available from DOI: 10.1016/j.jlumin.2021.118590.

69. Ogiegło, Joanna M; Katelnikovas, Arturas; Zych, Aleksander; Justel, Thomas; Meijerink, Andries; Ronda, Cees R. Luminescence and luminescence quenching in $Gd_3(Ga, Al)_5O_{12}$ scintillators doped with Ce^{3+}. *The Journal of Physical Chemistry A*. 2013, vol. 117, no. 12, pp. 2479–2484. Available from DOI: 10.1021/jp309572p.

70. Sidletskiy, O; Gerasymov, Ia; Kurtsev, D; Kononets, V; Pedash, V; Zelenskaya, O; Tarasov, V; Gektin, A; Grinyov, B; Lebbou, K, et al. Engineering of bulk and fiber-shaped YAGG: Ce scintillator crystals. *CrystEngComm*. 2017, vol. 19, no. 6, pp. 1001–1007. Available from DOI: 10.1039/C6CE02330D.

71. Sidletskiy, Oleg; Kononets, Valerii; Lebbou, Kheirreddine; Neicheva, Svetlana; Voloshina, Olesya; Bondar, Valerii; Baumer, Vyacheslav; Belikov, Konstantin; Gektin, Alexander; Grinyov, Boris, et al. Structure and scintillation yield of Ce-doped Al–Ga substituted yttrium garnet. *Materials Research Bulletin*. 2012, vol. 47, no. 11, pp. 3249–3252. Available from DOI: 10.1016/j.materresbull.2012.08.004.

72. Kamada, Kei; Yanagida, Takayuki; Endo, Takanori; Tsutumi, Kousuke; Usuki, Yoshiyuki; Nikl, Martin; Fujimoto, Yutaka; Fukabori, Akihiro; Yoshikawa, Akira. 2inch diameter single crystal growth and scintillation properties of $Ce : Gd_3Al_2Ga_3O_{12}$. *Journal of Crystal Growth*. 2012, vol. 352, no. 1, pp. 88–90. Available from DOI: 10.1016/j.jcrysgro.2011.11.085. The Proceedings of the 18th American Conference on Crystal Growth and Epitaxy.

73. Shwartz, B. A. Scintillation Detectors in Experiments on High Energy Physics. In: Korzhik, Mikhail; Gektin, Alexander (eds.). *Engineering of Scintillation Materials and Radiation Technologies*. Cham: Springer International Publishing, 2017, pp. 211–230. Available from DOI: 10.1007/978-3-319-68465-9_13.

74. Mitrofanov, IG; Litvak, ML; Varenikov, AB; Barmakov, YN; Behar, A; Bobrovnitsky, YI; Bogolubov, EP; Boynton, WV; Harshman, K; Kan, E, et al. Dynamic albedo of neutrons (DAN) experiment onboard NASA's Mars Science Laboratory. *Space science reviews*. 2012, vol. 170, pp. 559–582. Available from DOI: 10.1007/s11214-012-9924-y.

75. Orfano, Matteo; Perego, Jacopo; Cova, Francesca; Bezuidenhout, Charl X; Piva, Sergio; Dujardin, Christophe; Sabot, Benoit; Pierre, Sylvie; Mai, Pavlo; Daniel, Christophe, et al. Efficient radioactive gas detection by scintillating porous metal–organic frameworks. *Nature Photonics*. 2023, vol. 17, no. 8, pp. 672–678. Available from DOI: 10.26434/chemrxiv-2022-9vglj.

76. Kessler, P.; Behnke, B.; Dabrowski, R.; Dombrowski, H.; Röttger, A.; Neumaier, S. Novel spectrometers for environmental dose rate monitoring. *Journal of Environmental Radioactivity*. 2018, vol. 187, pp. 115–121. Available from DOI: 10.1016/j.jenvrad.2018.01.020.

77. Tous, Jan; Horodysky, Petr; Blazek, Karel; Nikl, Martin. High resolution thin scintillator imaging plates used for X-ray NDT applications. In: *2nd International Symposium on NOT in Aerospace*. 2010.

78. Hampel, U; Bieberle, A; Hoppe, D; Kronenberg, J; Schleicher, E; Sühnel, T; Zimmermann, F; Zippe, C. High resolution gamma ray tomography scanner for flow measurement and non-destructive testing applications. *Review of scientific instruments*. 2007, vol. 78, no. 10, p. 103704. Available from DOI: 10.1063/1.2795648.

79. Kerlin, Thomas W.; Upadhyaya, Belle R. Chapter 16 - Nuclear plant instrumentation. In: Kerlin, Thomas W.; Upadhyaya, Belle R. (eds.). *Dynamics and Control of Nuclear Reactors*. Academic Press, 2019, pp. 213–235. Available from DOI: 10.1016/B978-0-12-815261-4.00016-0.

80. Spassky, Dmitry; Fedyunin, F; Rubtsova, E; Tarabrina, N; Morozov, V; Dzhevakov, P; Chernenko, K; Kozlova, N; Zabelina, E; Kasimova, V, et al. Structural, optical and luminescent properties of undoped $Gd_3Al_xGa_{(5-x)}O_{12}$ $(x = 0, 1, 2, 3)$ and $Gd_2YAl_2Ga_3O_{12}$ single crystals. *Optical Materials*. 2022, vol. 125, p. 112079. Available from DOI: 10.1016/j.optmat.2022.112079.

81. Vrubel, Ivan I; Polozkov, Roman G; Shelykh, Ivan A; Khanin, Vasilii M; Rodnyi, Piotr A; Ronda, Cees R. Bandgap engineering in yttrium–aluminum garnet with Ga doping. *Crystal Growth & Design*. 2017, vol. 17, no. 4, pp. 1863–1869. Available from doi: 10.1021/acs.cgd.6b01822.

82. Wang, Chao; Ding, Dongzhou; Wu, Yuntao; Li, Huanying; Chen, Xiaofeng; Shi, Jian; Wang, Qingqing; Ye, Le; Ren, Guohao. Effect of thermal annealing on scintillation properties of $Ce:Gd_2Y_1Ga_{2.7}Al_{2.3}O_{12}$ under different atmosphere. *Applied Physics A*. 2017, vol. 123, pp. 1–6. Available from doi: 10.1007/s00339-017-0997-z.

83. Wu, Yuntao; Meng, Fang; Li, Qi; Koschan, Merry; Melcher, Charles L. Role of Ce^4+ in the scintillation mechanism of codoped $Gd_3Ga_3Al_2O_{12}Ce$. *Physical review applied*. 2014, vol. 2, no. 4, p. 044009. Available from doi: 10.1103/PhysRevApplied.2.044009.

84. Korzhik, Mikhail; Alenkov, Vladimir; Buzanov, Oleg; Dosovitskiy, Georgy; Fedorov, Andrei; Kozlov, Dmitry; Mechinsky, Vitaly; Nargelas, Saulius; Tamulaitis, Gintautas; Vaitkevičius, Augustas. Engineering of a new single-crystal multi-ionic fast and high-light-yield scintillation material $(Gd_{0.5}-Y_{0.5})_3Al_2Ga_3O_12:Ce,Mg$. *CrystEngComm*. 2020, vol. 22, no. 14, pp. 2502–2506. Available from doi: 10.1039/D0CE00105H.

85. Sidletskiy, Oleg; Gerasymov, Iaroslav; Boyaryntseva, Yanina; Arhipov, Pavlo; Tkachenko, Serhii; Zelenskaya, Olga; Bryleva, Kateryna; Belikov, Konstantin; Lebbou, Kheirreddine; Dujardin, Christophe, et al. Impact of carbon co-doping on the optical and scintillation properties of a YAG: Ce scintillator. *Crystal Growth & Design*. 2021, vol. 21, no. 5, pp. 3063–3070. Available from doi: 10.1021/acs.cgd.1c00259.

86. Kofanov, D; Gerasymov, Ia; Sidletskiy, O; Tkachenko, S; Boyaryntseva, Ya; Kurtsev, D; Zelenskaya, O; Okrushko, O; Gorbacheva, T; Viagin, O, et al. LuAG: Ce and LuYAG: Ce scintillation crystals grown under reducing conditions from W crucibles. *Optical Materials*. 2022, vol. 134, p. 113176. Available from doi: 10.1016/j.optmat.2022.113176.

87. Zapadlík, O; Nikl, M; Polák, J; Průša, P; Linhart, V. Engineering of YAG: Ce to improve its scintillation properties. *Optical Materials: X*. 2022, vol. 15, p. 100165. Available from doi: 10.1016/j.omx.2022.100165.

88. Ding, Shoujun; Ren, Hao; Zou, Yong; Liu, Wenpeng; Zhang, Qingli. Single crystal growth and property investigation of Dy^{3+} and Tb^{3+} co-doped $Gd_3Sc_2Al_3O_{12}$ (GSAG): multiple applications for GaN blue LD pumped all-solid-state yellow lasers and UV or blue light chip excited solid-state lighting. *Journal of Materials Chemistry C*. 2021, vol. 9, no. 30, pp. 9532–9538. Available from doi: 10.1039/D1TC02294F.

89. Lutts, GB; Denisov, AL; Zharikov, EV; Zagumennyi, AI; Kozlikin, SN; Lavrishchev, SV; Samoylova, SA. GSAG and YSAG: a study on isomorphism and crystal growth. *Optical and quantum electronics*. 1990, vol. 22, S269–S281. Available from doi: 10.1007/BF02089015.

90. Kling, A; Kollewe, D; Mateika, D. Scintillation properties of cerium-doped gadolinium-scandium-aluminum garnets. *Nuclear Instruments and Methods in Physics Research Section A: Accelerators, Spectrometers, Detectors and Associated Equipment*. 1994, vol. 346, no. 1-2, pp. 205–212. Available from DOI: 10.1016/0168-9002(94)90705-6.

91. Cherepy, Nerine J; Payne, Steve A; Asztalos, Stephen J; Hull, Giulia; Kuntz, Joshua D; Niedermayr, Thomas; Pimputkar, Siddha; Roberts, Jeffery J; Sanner, Robert D; Tillotson, Thomas M, et al. Scintillators with potential to supersede lanthanum bromide. *IEEE Transactions on Nuclear Science*. 2009, vol. 56, no. 3, pp. 873–880. Available from DOI: 10.1109/TNS.2009.2020165.

92. Spassky, Dmitry; Kozlova, Nina; Zabelina, Evgeniia; Kasimova, Valentina; Krutyak, Nataliya; Ukhanova, Alisa; Morozov, Vladimir A; Morozov, Anatolii V; Buzanov, Oleg; Chernenko, Kirill, et al. Influence of the Sc cation substituent on the structural properties and energy transfer processes in GAGG: Ce crystals. *CrystEngComm*. 2020, vol. 22, no. 15, pp. 2621–2631. Available from DOI: 10.1039/D0CE00122H.

93. Chewpraditkul, Warut; Pattanaboonmee, Nakarin; Chewpraditkul, Weerapong; Sakthong, Ongsa; Kim, Kyoung Jin; Yoshino, Masao; Horiai, Takahito; Kurosawa, Shunsuke; Yoshikawa, Akira; Kamada, Kei, et al. Luminescence and scintillation properties of $Gd_3Sc_2(Al_{3-x}Ga_x)O_{12}:Ce$ $(x = 1, 2, 3)$ garnet crystals. *Radiation Physics and Chemistry*. 2021, vol. 187, p. 109559. Available from DOI: 10.1016/j.radphyschem.2021.109559.

94. Zapadlík, Ondřej; Pejchal, Jan; Kucerkova, Romana; Beitlerová, Alena; Nikl, Martin. Composition-engineered GSAG garnet: single-crystal host for fast scintillators. *Crystal Growth & Design*. 2021, vol. 21, no. 12, pp. 7139–7149. Available from DOI: 10.1021/acs.cgd.1c01007.

95. Zajíc, František. *Růst fotonických monokrystalů metodou zonální tavby*. 2022. Bachelor thesis. Faculty of Matematics and Physics, Charles University, Prague.

96. Zajic, Frantisek; Klejch, Martin; Elias, Adam; Klicpera, Milan; Beitlerová, Alena; Nikl, Martin; Pospisil, Jiri. Nd: YAG single crystals grown by the floating zone method in a laser furnace. *Crystal Growth & Design*. 2023, vol. 23, no. 4, pp. 2609–2618. Available from DOI: 10.1021/acs.cgd.2c01453.

97. Dantelle, Géraldine; Boulon, Georges; Guyot, Yannick; Testemale, Denis; Guzik, Malgorzata; Kurosawa, Shunsuke; Kamada, Kei; Yoshikawa, Akira. Research on efficient fast scintillators: evidence and X-ray absorption near edge spectroscopy characterization of Ce^{4+} in Ce^{3+}, Mg^{2+}-Co-doped $Gd_3Al_2Ga_3O_{12}$ garnet crystal. *physica status solidi (b)*. 2020, vol. 257, no. 8, p. 1900510. Available from DOI: 10.1002/pssb.201900510.

98. Babin, V.; Herman, P.; Kucera, M.; Nikl, M.; Zazubovich, S. Effect of Mg^{2+} co-doping on the photo- and thermally stimulated luminescence of the $(Lu, Gd)_3(Ga, Al)_5O_{12}:Ce$ epitaxial films. *Journal of Luminescence*. 2019, vol. 215, p. 116608. Available from DOI: 10.1016/j.jlumin.2019.116608.

99. Kučera, Miroslav; Nikl, Martin; Hanuš, Martin; Onderišinová, Zuzana. Gd^{3+} to Ce^{3+} energy transfer in multi-component GdLuAG and GdYAG garnet scintillators. *physica status solidi (RRL)–Rapid Research Letters*. 2013, vol. 7, no. 8, pp. 571–574. Available from DOI: 10.1002/pssr.201307256.

100. Khanin, Vasilii; Venevtsev, Ivan; Chernenko, Kirill; Pankratov, Vladimir; Klementiev, Konstantin; Swieten, Thomas van; Bunningen, Arnoldus J van; Vrubel, Ivan; Shendrik, Roman; Ronda, Cees, et al. Exciton interaction with Ce^{3+} and Ce^{4+} ions in $(LuGd)_3(Ga,Al)_5O_{12}$ ceramics. *Journal of Luminescence*. 2021, vol. 237, p. 118150. Available from DOI: 10.1016/j.jlumin.2021.118150.

101. Ogiegło, Joanna M; Zych, Aleksander; Ivanovskikh, Konstantin V; Jüstel, Thomas; Ronda, Cees R; Meijerink, Andries. Luminescence and energy transfer in $Lu_3Al_5O_{12}$ scintillators co-doped with Ce^{3+} and Tb^{3+}. *The Journal of Physical Chemistry A*. 2012, vol. 116, no. 33, pp. 8464–8474. Available from DOI: /10.1021/jp301337f.

102. Varney, CR; Reda, SM; Mackay, DT; Rowe, MC; Selim, FA. Strong visible and near infrared luminescence in undoped YAG single crystals. *AIP Advances*. 2011, vol. 1, no. 4, p. 042170. Available from DOI: 10.1063/1.3671646.

103. Varney, CR; Mackay, DT; Pratt, A; Reda, SM; Selim, FA. Energy levels of exciton traps in yttrium aluminum garnet single crystals. *Journal of Applied Physics*. 2012, vol. 111, no. 6, p. 063505. Available from DOI: 10.1063/1.3693581.

104. Yanagida, Takayuki; Kamada, Kei; Fujimoto, Yutaka; Yagi, Hideki; Yanagitani, Takagimi. Comparative study of ceramic and single crystal Ce: GAGG scintillator. *Optical Materials*. 2013, vol. 35, no. 12, pp. 2480–2485. Available from DOI: 10.1016/j.optmat.2013.07.002.

105. Sibczynski, Pawel; Iwanowska-Hanke, Joanna; Moszyński, Marek; Swiderski, Lukasz; Szawłowski, Marek; Grodzicka, Martyna; Szczęśniak, Tomasz; Kamada, Kei; Yoshikawa, Akira. Characterization of GAGG: Ce scintillators with various Al-to-Ga ratio. *Nuclear Instruments and Methods in Physics Research Section A: Accelerators, Spectrometers, Detectors and Associated Equipment*. 2015, vol. 772, pp. 112–117. Available from DOI: 10.1016/j.nima.2014.10.041.

106. Iwanowska, Joanna; Swiderski, Lukasz; Szczesniak, Tomasz; Sibczynski, Pawel; Moszynski, Marek; Grodzicka, Martyna; Kamada, Kei; Tsutsumi, Kousuke; Usuki, Yoshiyuki; Yanagida, Takayuki, et al. Performance of cerium-doped $Gd_3Al_2Ga_3O_{12}$ (GAGG: Ce) scintillator in gamma-ray spectrometry. *Nuclear Instruments and Methods in Physics Research Section A: Accelerators, Spectrometers, Detectors and Associated Equipment*. 2013, vol. 712, pp. 34–40. Available from DOI: 10.1016/j.nima.2013.01.064.

107. Ali, Hanan; Masschelein, P.; Bruyere, S.; Pigeat, P.; Dauscher, A.; Rinnert, H.; Horwat, D.; Khedr, Mohamed Atta; Giba, Alaa E. White light emission from Sm-doped YAG ceramic controlled by the excitation wavelengths. *Optics & Laser Technology*. 2021, vol. 142, p. 107223. Available from DOI: https://doi.org/10.1016/j.optlastec.2021.107223.

108. Zajíc, František; Pospíšil, Jiří; Kučerková, Romana; Boháček, Pavel; Nikl, Martin. Growth of GSAG:Ce scintillator by floating zone method under pressurized oxygen atmosphere. *Journal of Crystal Growth*. 2024, vol. 627, p. 127479. Available from DOI: 10.1016/j.jcrysgro.2023.127479.

List of Figures

1.1 Scintillation process divided into three consecutive parts: conversion, transport and luminescence [12]. 11
1.2 Schematic of the principle of the Czochralski method (left) and illustration of the different steps (a–j) of the Czochralski process for growing a Si crystal. (a) The polycrystalline feedstock is melted (b) in a crucible. (c, d) Seeding procedure: The seed crystal is dipped into the melt, followed by Dash necking (e), shouldering (f), cylindrical growth (g), growth of end cone (h), lift off (i), cooling down and removing of the crystal (j) [17]. 13
1.3 Schematic representation of micro-pulling-down method [28]. . . . 14

2.1 Mass atenuation coefficients of photons with different energy in lead [53]. 17

4.1 Active afterheater setup. 27

5.1 Presintering and sintering temperature profiles of GGAG and GSAG rod precursors. 29
5.2 **a)** Arrangement of afterheater, rod precursor and seed crystal in LDFZM furnace. **b)** The example of GGAG single crystal prepared. 31
5.3 The shape of hot zone during GSAG growth **a)** ideal **b)** too narrow **c)** too wide. The visible bubbles are unwanted at every case and are directly responsible for the irregular diameter of the single crystal and consequent creation of the cracks 32

6.1 Cut samples of GGAG. 34
6.2 Absorption spectra of GGAG samples. 34
6.3 Radioluminescence spectra of GGAG samples. 36
6.4 Scintillation decays of GGAG MFF6 start and MFF2 start samples. 36
6.5 Pulse height spectra of GGAG samples and BGO reference, with a shaping time set to 1 µs. 38
6.6 Measured and normalised afterglow curves of the GGAG samples, compared to the BGO reference. 39
6.7 Normalised photoluminescence excitation spectra of GGAG samples measured at $\lambda_{em} = 530$ nm. 40
6.8 Photoluminescence emission spectra of GGAG samples for the excitation wavelengths 340 nm. 41
6.9 Photoluminescence emission spectra of GGAG samples for the excitation wavelengths 440 nm. 42
6.10 Photoluminescence decays of MFF6 1start and MFF2 2start samples from GGAG single crystals measured for $\lambda_{ex} = 454$ nm, $\lambda_{em} = 530$ nm. 43
6.11 Absorption spectra of GGAG samples. 45
6.12 Radioluminescence spectra of GSAG samples. 46
6.13 Detail of radioluminescence spectra for GSAG1 samples. 47
6.14 Scintillation decays of GSAG1 4end and GSAG HUGO samples. . 47

6.15 Afterglow of GSAG samples. 48
6.16 Photoluminescence excitation spectra for emission wavelength $\lambda_{em} = 550$ nm of GSAG samples. 50
6.17 Photoluminescence emission spectra for excitation wavelength $\lambda_{ex} = 340$ nm of GSAG samples. 52
6.18 Photoluminescence emission spectra for excitation wavelength $\lambda_{ex} = 460$ nm of GSAG samples. 53
6.19 Photoluminescence decays of GSAG1 - 4 end and GSAG8 HUGO for excitation $\lambda_{ex} = 452$ nm and emission $\lambda_{ex} = 554$ nm and photoluminescence decay of GSAG1 - 4 end for excitation $\lambda_{ex} = 339$ nm and emission $\lambda_{ex} = 554$ nm. 54

7.1 In the top graph there is RT absorption spectra of GSAG1 samples compared with GSAG sample from Zapadlík [94]. Difference spectrum obtained by subtracting the absorption spectra of GSAG taken by Zapadlík from the GSAG - start 2 one is in the inset . . 56
7.2 Comparison of absorption spectra of GSAG - end 3 before and after annealing. In the inset there is difference spectrum obtained by subtracting annealed spectra from unannealed. 56
7.3 Comparison of radioluminescence spectra of GSAG prepared by floating-zone, micro-pulling-down and Czochralski methods. . . . 58
7.4 Radioluminescence spectra of GSAG3 single-crystal by CCD camera detector and measurement of photoluminescence decay with excitation at 266 nm and emission 760 nm showing 6.5 ms decay time typical for Fe^{3+} [102, 107] 59
7.5 Radioluminescence spectra of GSAG precursors, absolute and normalised. 59

List of Tables

6.1 Measured samples of GGAG. 33
6.2 Scintillation and photoluminescence decay time constants, light sums and light yield of GGAG samples. 37
6.3 Measured samples of GSAG. 44
6.4 Scintillation and photoluminescence decay time constants, light sums and light yield of GSAG samples. 49